Science Robotics
AAAS

Manuscript

Front Matter

Title

Telerobotic neurovascular interventions with magnetic manipulation

Authors

Yoonho Kim,[1] Emily Genevriere,[1] Pablo Harker,[2,3] Jaehun Choe,[1] Marcin Balicki,[4] Robert W. Regenhardt,[2] Justin E. Vranic,[2] Adam A. Dmytriw,[2] Aman B. Patel,[2] Xuanhe Zhao[1,5,*]

Affiliations

1. Department of Mechanical Engineering, Massachusetts Institute of Technology, Cambridge, Massachusetts, USA
2. Department of Neurosurgery, Massachusetts General Hospital and Harvard Medical School, Boston, Massachusetts, USA
3. Department of Neurology and Rehabilitation Medicine, University of Cincinnati College of Medicine, Cincinnati, Ohio, USA
4. Philips Research North America, Cambridge, Massachusetts, USA
5. Department of Civil and Environmental Engineering, Massachusetts Institute of Technology, Cambridge, Massachusetts, USA

*Corresponding author. Email: zhaox@mit.edu

Abstract

Advances in robotic technology have been adopted in various subspecialties of both open and minimally invasive surgery, offering benefits such as enhanced surgical precision and accuracy with reduced fatigue of the surgeon. Despite the advantages, robotic applications to endovascular neurosurgery have remained largely unexplored due to technical challenges such as the miniaturization of robotic devices that can reach the complex and tortuous vasculature of the brain. Although some commercial robotic systems enable precise manipulation of conventional guidewires for coronary and peripheral vascular interventions, they remain unsuited for neurovascular applications due to the considerably smaller and more tortuous anatomy of cerebral arteries. Here we present a teleoperated robotic neurointerventional platform based on magnetic manipulation. Our system consists of a magnetically controlled guidewire, a robot arm with an actuating magnet to steer the guidewire, a set of motorized linear drives to advance or retract the guidewire and a microcatheter, and a remote-control console to operate the system using feedback from real-time fluoroscopy. We demonstrate our system's capability to navigate narrow and winding pathways both in vitro with realistic neurovascular phantoms representing the human anatomy and in vivo in the porcine brachial artery with accentuated tortuosity for preclinical evaluation. We further demonstrate telerobotically assisted therapeutic procedures including coil embolization and clot retrieval thrombectomy for treating cerebral aneurysms and ischemic stroke, respectively. Our telerobotic neurointerventional system could enable safer and quicker access to hard-to-reach lesions while minimizing the radiation exposure to physicians and open the possibility of remote procedural services to address challenges in current stroke systems of care.

Summary

A teleoperated robotic system with magnetic actuation of a guidewire has been utilized for endovascular stroke intervention.

Main Text

Introduction

Stroke remains one of the leading causes of death and long-term disabilities in the United States, where it kills about 140,000 people and costs around $46 billion each year (1). Stroke occurs when blood flow to the brain is blocked by blood clots or plaques (ischemic) or when a weakened blood vessel ruptures and causes bleeding in the brain (hemorrhagic). Both ischemic and hemorrhagic strokes can lead to permanent brain damage, and hence early intervention is critical to better protect the brain. However, current stroke systems of care require physically transporting patients to tertiary hospitals for such interventions. For patients in rural areas, where acute-care services are often unavailable, stroke is challenging to treat in a timely fashion, and patients can become no longer eligible for therapies when their brains are irreparably damaged. One potential solution to this logistical challenge is to use teleoperated robotic systems for remote surgery (2). Such telerobotic platforms could enable skilled neurointerventionalists (physicians who are surgically trained for endovascular stroke intervention) at large institutions to perform surgical tasks remotely on patients at their local hospitals, obviating transport of patients at the expense of time (3).

In the broader context of endovascular neurosurgery, there are several challenges in the operating room as well. In neurovascular interventions, microguidewires are primarily used for intravascular access to target lesions and to facilitate the placement of other interventional or therapeutic devices such as microcatheters, coils, and stents. For steering purposes, typical guidewires have pre-shaped or shapeable distal tips which can be oriented toward a desired direction by manually twisting their proximal ends. However, this twisting maneuver for conventional passive guidewires often becomes ineffective and rather unpredictable due to the jerky motion of the pre-bent tip caused by friction, also known as "whipping (4)," particularly when navigating through narrow and winding pathways. This makes it difficult to reach distal branches of cerebral arteries and in some circumstances renders distal target access unfeasible. The predefined shape of the tip might also deform within the vessel, especially during complicated and lengthy guiding maneuvers (5). Moreover, interventionalists often need to continuously turn the guidewire while inserting it to prevent the pre-bent tip from latching onto any small ostium or opening along the path; the distal tip could otherwise become stuck and potentially cause vascular injury or perforation upon further pushing. To avoid such complications, physicians always need to verify the distal tip movement under fluoroscopy when manually manipulating guidewires, which exposes them to continuous x-rays during the interventional procedures. For interventionalists, this repetitive radiation exposure is being recognized as a greater risk than previously appreciated (6, 7). Telerobotic interventional systems, which allow for remote control of robotic guidewires with active steering and navigational capabilities, could potentially help to resolve these clinical and technical challenges as well.

However, robotic applications to endovascular neurosurgery have remained largely unexplored due to the lack of appropriate technologies. The biggest hurdle thus far has been the miniaturization of robotic devices so that they are thin and flexible enough to navigate through the narrow and complex neurovasculature. Existing robotic catheters or endoscopes with active steering and navigational capabilities are often limited to relatively large scales (a few millimeters in diameter), due to the miniaturization challenges inherent in their con-

ventional actuation mechanisms (8), and are therefore unsuitable for endovascular interventions (9).

Instead of directly tackling the challenges of realizing robotic or steerable guidewires and catheters at submillimeter scale, the industry has developed vascular robotic platforms that can accommodate and manipulate conventional guidewires and catheters under remote control. For example, the Magellan™ Robotic System of Hansen Medical (acquired by Auris Health) features an articulating sheath with linear and rotary drives to enable insertion, rotation, and retraction of conventional guidewires (9, 10). Other examples include the CorPath® GRX of Corindus Vascular Robotics (acquired by Siemens Healthineers) and R-One™ of Robocath, both of which can similarly advance or retract and rotate commercially available guidewires and catheters using linear and rotary drives under remote control (11). The R-One™ system has recently been approved for percutaneous coronary intervention only in the European Union (12), and the CorPath® GRX is currently approved for peripheral vascular intervention as well as percutaneous coronary intervention in the United States, European Union, and other countries (13). While the CorPath® GRX was originally designed to manipulate the larger-gauge devices used for percutaneous coronary and peripheral vascular interventions, the system is cleared for neurovascular intervention in the European Union, Australia, and New Zealand (13). However, it has not yet been approved for neurovascular intervention in other countries including the United States (14), possibly because of its current technical limitations for intracranial applications as discussed in a recent report (15). Following some modifications in the system to facilitate the use of smaller guidewires and microcatheters for intracranial access and intervention, recent publications reported its first-in-human, off-label use for endovascular coiling of aneurysms in relatively proximal areas of the intracranial artery (13, 16). However, to date, no robotic systems have been reported to accomplish robotically assisted endovascular treatment of cerebral aneurysms or infarctions which commonly occur in more distal and difficult-to-reach areas such as the middle or anterior cerebral arteries. More importantly, the existing robotic systems designed to manipulate conventional guidewires would retain the functional limitations inherent in the twist-based steering of pre-shaped, passive guidewires discussed above.

The present work is aimed at tackling the aforementioned technical and clinical challenges in current endovascular neurosurgery and stroke systems of care, where the application of robotics can be the key to the solution. In this paper, we present a teleoperated magnetic manipulation platform to enable robotic application in endovascular neurosurgery for treating stroke and aneurysms, which have remained largely unattainable with existing continuum or vascular robotic systems. Our telerobotic neurointerventional system allows for precise control of a magnetically steerable, soft continuum guidewire in the complex neurovasculature through a robot arm with an actuating magnet attached to its end-effector that is remotely controlled by an operator to apply the magnetic fields required for actuation and steering of the magnetic guidewire. A pair of motorized linear drives can advance or retract the guidewire and a microcatheter can travel over the guidewire along the navigated path. Through quantitative analysis and characterization of the magnetic guidewire's behavior under the action of the actuating magnet, we identified a set of fundamental and unique steering control principles for the magnetic soft continuum guidewire that can provide guidance on how to manipulate the single actuating magnet with minimal motion of the robot arm to achieve the desired configuration of the guidewire. Through real-time teleoperation of the system under feedback from x-ray fluoroscopy and virtual visualization of the robot arm, we

demonstrate our system's steering and navigational capabilities to enable access to different branches of cerebral arteries using realistic anatomical models that include all relevant pathway attributes to represent the human neurovascular anatomy. We further demonstrate our system's capability to telerobotically assist therapeutic procedures that are commonly performed in endovascular neurosurgery, such as coil embolization for treating cerebral aneurysms and clot retrieval thrombectomy for treating ischemic stroke due to cerebral infarctions. Then, to validate the safety and effectiveness of our system in physiologically relevant conditions, we demonstrate the system's steering and navigational capabilities in vivo using a porcine brachial artery tortuosity model (17) that simulates the tortuosity of the human intracranial arteries. Lastly, to evaluate the user experience with our developed system, we assess the learning curve for neurointerventionalists associated with real-time teleoperation of the system for magnetic steering and navigation in vitro with clinically challenging anatomy.

Results

Telerobotic system design overview

Fig. 1 provides an overview of our telerobotic neurointerventional system deployed in clinical settings for image-guided endovascular procedures, with a C-arm fluoroscope providing real-time imaging of the guidewire navigating in the patient's blood vessels under magnetic manipulation. Mounted on a mobile platform beside the operating table, the robot arm is teleoperated by the interventionalist from a remote-control console to steer the magnetic guidewire by varying the position and orientation of the magnet at the robot arm's end-effector around the patient's head. The guidewire/microcatheter advancing unit is placed near the patient to advance or retract the guidewire and the microcatheter from their proximal ends through the femoral or radial artery access point.

The magnetic guidewire has a steerable distal portion, which can be manipulated through spatial positioning of the actuating magnet at the robot arm's end-effector relative to the steerable tip (**Fig. 2A**). While spatial positioning of the magnet requires at most six degrees of freedom (DOFs), our system uses a 7-DOF serial robot arm manipulator with seven revolute joints (**Fig. 2A**) to take advantage of its kinematic redundancy for safer operation in cluttered environments with a confined workspace. The extra DOF provides an increased level of dexterity that helps the robot arm avoid singularities and joint limits (18) as well as workspace obstacles (the patient, C-arm, operating table, radiation shields). The guidewire and the microcatheter can be advanced or retracted individually by a pair of advancing units, each of which uses a worm drive to convert the rotary motion transmitted from the DC motor at the base through a flexible shaft to a linear motion (**Fig. 2A**). The system is teleoperated from the remote-control console under visual feedback from real-time fluoroscopic imaging of the guidewire/microcatheter in the blood vessels (**Fig. 2B**). The configuration of the robot arm is visualized in real time on the control workstation based on the joint position data (**Fig. 2B**). This real-time visualization helps the operator observe the current state of the robot arm while controlling it remotely. It can also be used for preprocedural planning and/or training of the robot manipulation in a virtual environment replicating the real world (3D CAD models), including the surrounding objects that are known a priori, to help prevent collisions during operation while performing magnetic steering and navigation. Spatial positioning of the actuating magnet can be achieved via 6-DOF position control of the robot arm's end-effector with a joystick controller, and advancement or retraction of the

guidewire and the microcatheter can be controlled either independently or simultaneously with the joystick buttons (**Fig. 2C**). The operator could observe and confirm the current states of the guidewire and the microcatheter from the fluoroscopic images while operating the robot arm and the guidewire/catheter advancing units with the joystick controller from the remote-control console (**Fig. 2B**).

Design of the magnetic soft continuum guidewire

Leveraging our previous work on the design and fabrication of ferromagnetic soft continuum robots (8), we designed our magnetic guidewire to have a smaller outer diameter (400 μm) with greatly improved mechanical robustness in terms of both strength and toughness while maintaining good steerability. With these improvements, the newly designed magnetic guidewire is as thin and flexible as standard neurovascular guidewires (typically with outer diameters of 0.014 inches) and compatible with commercially available microcatheters (typically with inner diameters of 0.017/0.021/0.027/0.033 inches) for neurovascular interventions. The magnetic guidewire consists of a tapered core of nickel-titanium alloy (nitinol), which is coated with a soft, yet durable polymer jacket composed of thermoplastic polyurethane (TPU) with embedded neodymium-iron-boron (NdFeB) particles. With the NdFeB particles in the polymer jacket magnetized along the guidewire's axial direction, the distal portion (50 mm from the end) of the guidewire is magnetically responsive and can be steered with an actuating magnet (**Fig. 2A**), utilizing the magnetic torques and forces generated from the embedded magnetic dipoles under the applied fields and field gradients (19-21). The NdFeB particle loading concentration was determined to be 20% by volume according to the optimal design strategy proposed in the previous study (8). The resultant magnetic polymer jacket has the magnetization (M) of 128 kA/m and the shear modulus (G) of 1210 kPa (**fig. S1A**).

To enable sharp turns at acute-angled corners in blood vessels with clinically challenging tortuosity, a short segment (4-mm-long; denoted L_2 in **Fig. 3B**) at the distal end of the guidewire's magnetically responsive portion is composed of the TPU-NdFeB composite only, without the stiff nitinol core, and is therefore much softer and more responsive than the remainder that contains the nitinol core. When magnetic fields are applied by the actuating magnet, the unconstrained portion (free from contact with blood vessels) of the guidewire's steerable tip of length L, which consists of a stiffer segment of length L_1 that contains the nitinol core and the softer segment of length L_2 that does not contain the stiff core, deflects either toward or away from the magnet depending on the magnetic polarity of the actuating magnet (**Fig. 3B**). Tensile strength testing demonstrated that the TPU-NdFeB composite can withstand tensile stresses up to 12 MPa, which translates into 1.5 N of tensile forces on the distal tip of the guidewire, while being stretched beyond 14 times its original length (**fig. S1B**). The measured tensile strength of the distal tip is comparable to that of commercially available neurovascular guidewires of similar dimension such as ASAHI CHIKAI® 0.014-inch guidewires with a tensile strength of 2.45 N (22). However, the high stretchability of the TPU-NdFeB composite could provide greater resistance in terms of the energy required to cause fracture or joint failure at the distal tip when compared with conventional guidewires which typically have flexible spring or coil tips that are subject to brittle fracture.

Working distance for the actuating magnet

The use of a single actuating magnet for steering control of the magnetic guidewire requires some practical considerations when determining the shape, size, and working distance of the magnet, given the workspace constraints due to the patient geometry and surrounding objects as well as the spatial distribution of magnetic fields around the magnet. We first estimated a possible working range for the actuating magnet to steer the guidewire while it is spatially positioned near the patient's head, with considerations of the average head size (23) and the anatomical location and orientation of intracranial arteries (**Fig. 3A**). For guidewire navigation in cerebral arteries, it is reasonable to consider the distance from the surface of the magnet to the Circle of Willis — an arterial network in the middle of the head (between the right and left hemispheres; **fig. S2A** for vascular anatomy and nomenclature) — which can be regarded as the farthest area within the cranium from the actuating magnet. Assuming that the magnet is positioned in one of the nearest possible locations around the head with some safety margins considered, the estimated distance from the magnet surface to the Circle of Willis is around 100 mm, as illustrated on the sagittal plane in **Fig. 3A**. Then, for navigation from the proximal to the distal areas of cerebral arteries, the effective working distance between the magnet surface and the guidewire's steerable tip would be below 100 mm and further decrease as the guidewire is advanced to the periphery. For example, if the guidewire is currently in the distal end (C4 in **fig. S2B**) of the left internal carotid artery (ICA; **fig. S2B**) and about to navigate through the left middle cerebral artery (MCA; see **fig. S2B**), the estimated working distance from the magnet surface to the guidewire at the ICA bifurcation is around 80~90 mm, as illustrated on the frontal and transverse planes in **Fig. 3A**. Then, the magnetic field applied from this distance by the magnet should be strong enough to induce the deflection of the guidewire tip along the desired direction toward the left M1 segment (**fig. S2B** for vascular anatomy and nomenclature). To ensure this, we characterized the behavior of the steerable tip under the influence of applied magnetic fields and field gradients from a single actuating magnet in the following section.

Steering principles for the magnetic guidewire

Under spatially uniform magnetic fields (between a pair of magnets), magnetic steering of the guidewire is driven solely by magnetic torques, which cause the guidewire's distal tip to bend toward the applied field direction (8, 20, 21). Magnetic actuation under spatially nonuniform fields (e.g., with a single magnet), however, involves magnetic forces as well as magnetic torques because of the presence of field gradients (8, 21). Therefore, the effects of magnetic forces on the guidewire's behavior should also be characterized when designing the steering control interface based on magnetic manipulation with a single magnet. Under the actuating magnetic field denoted by a vector $\mathbf{B}$, with the magnetization of the guidewire tip along its axial direction denoted by a vector $\mathbf{M}$, the magnetic body torque density (per unit volume of the magnetic composite material) can be expressed as

$$\boldsymbol{\tau} = \mathbf{M} \times \mathbf{B}\,, \tag{1}$$

and the magnetic body force density (per unit volume of the magnetic composite material) as

$$\mathbf{b} = (\mathrm{grad}\mathbf{B})\mathbf{M}\,, \tag{2}$$

where grad$\mathbf{B}$ denotes the spatial gradient of the applied magnetic field.

For the actuating magnet, we consider an axially magnetized, NdFeB (N52-grade) magnet of cylindrical shape (diameter and thickness of $2R$; **Fig. 3B**) with an axisymmetric field distribution (**fig. S3A**). For cylindrical magnets with the same diameter-to-thickness ratio, the shape of the magnetic field remains the same when normalized by the magnet's characteristic dimension (e.g., radius R). Therefore, the magnetic field at a certain point around the magnet can be expressed as a vector function of the spatial location of the point (denoted by a position vector $\mathbf{p}$ with respect to the center of the magnet in cylindrical coordinates) in a normalized form (by the magnet radius R) as

$$\mathbf{B}(\mathbf{p}) = B_{\mathrm{re}}\,\boldsymbol{\mathcal{F}}(\mathbf{p}/R)\,, \tag{3}$$

where B_{re} is the remanence of the magnet and $\boldsymbol{\mathcal{F}}$ denotes the vector function whose implicit form can be found in (24-26). Along the central axis of the magnet, the magnitude of the magnetic field can be expressed explicitly in a normalized form as

$$B = \frac{B_{\mathrm{re}}}{2}\left(\frac{d/R+1}{\sqrt{(d/R+1)^2+1}} - \frac{d/R-1}{\sqrt{(d/R-1)^2+1}}\right), \tag{4}$$

where d is the distance from the center of the magnet to the point of interest/measurement along the centerline (i.e., $\pm z$-direction in **fig. S3A**). Because the magnetic field strength decreases with the normalized distance d/R, as shown in **fig. S3B**, the actuating magnet should be large enough to steer the guidewire at a reasonable working distance discussed above. Typical steering and navigational tasks require the actuating field strength of at most 80 mT (8), which corresponds to the flux density at $d/R = 2.64$ from the center of the magnet as predicted from Eq. (4) and shown in **fig. S3B**. For a cylindrical magnet with diameter and thickness of 100 mm (i.e., $R = 50$ mm) and $B_{\mathrm{re}} = 1.45$ T, for example, this normalized distance translates into 132 mm from the magnet's center (or 82 mm from the magnet's surface). At this point, the field gradient along the centerline is calculated to be 1.75 mT/mm from the derivative of Eq. (3) as shown in **figs. S3C** and **S4**. Then, the magnetic torque density is evaluated to be 10.24 kN/m^2 from Eq. (1), and the moment acting on the guidewire's steerable tip of length L ($4 \le L \le 10$ mm) by the magnetic body force (per unit volume) is estimated from Eq. (2) to be 0.90 to 2.24 kN/m^2, which is around 10% to 20% of the magnetic torque density. The contribution of the magnetic body force to the steering of the distal tip further diminishes as the magnet size increases (i.e., inversely proportional to R; see **fig. S3C**), when compared to that of the magnetic torque. This implies that, for the magnetic guidewire, the magnetic torques are still the primary source of actuation even when it is steered by a single permanent magnet, provided that the actuating magnet is much larger than the steerable tip of the guidewire (i.e., $R \gg L$) and sufficiently far from the guidewire tip ($d > 2R$). Under these conditions, the tip deflection behavior of the guidewire can be characterized as a function of the normalized working distance from the magnet.

Principal modes of steering control

The most straightforward way to steer the magnetic guidewire with a single magnet is to position the magnet in such a way that the guidewire's distal tip bends toward the magnet. Such wire tip motion can be achieved by aligning the magnet's magnetic moment, which

points from the south to the north pole of the magnet along its central axis, with the desired steering direction to which the tip deflection is to occur. We define this mode of steering control, which seemingly attracts the distal end of the guidewire, as the attraction mode (**Fig. 3B**). If the magnet is flipped, with its magnetic moment reversed, the guidewire tip would be repelled away from the magnet surface. By the same token, we define this mode of steering control as the repulsion mode (**Fig. 3B**). We define the angular position of the magnet relative to the guidewire by the azimuthal angle (denoted φ in **Fig. 3B)**, which is the angle formed by the line connecting the base of the guidewire's softer tip in the undeformed reference state and the center of the magnet with respect to the straight tip of the guidewire. The working distance of the magnet is defined as the distance from the base of the guidewire's softer tip in the reference state to the center of the magnet (denoted d in **Fig. 3B**).

The tip deflection angle (denoted θ in **Fig. 3B**) varies with the working distance (**Fig. 3C**), which is normalized by the magnet's radius R for nondimensional representation as discussed above. The deflection angle also varies with the magnet's angular position φ, helping to achieve larger deflection when φ is greater than 90° in the attraction mode or smaller than 90° in the repulsion mode, respectively (**Fig. 3C**). It is worth noting that the asymmetry between the attraction and repulsion modes is attributed to the influence of magnetic forces resulting from the spatial gradients of the actuating fields discussed above. In both the attraction and repulsion modes, the bending actuation is initiated and driven by the magnetic body torques, because the magnetic body forces are almost negligible in the initial undeformed configuration (8). As the guidewire tip deforms and becomes more aligned with the applied fields, the magnetic body forces increase and attract the guidewire tip toward the magnet in both steering modes, as can be anticipated from Eq. (2). Consequently, the magnetic body forces help to increase the tip deflection angle in the attraction mode while decreasing the deflection angle in the repulsion mode, which leads to the slightly asymmetric profiles of the tip deflection angle as presented in **Fig. 3C**. Transition between the attraction and repulsion modes can be achieved through flipping the magnet by rotating the axis 7 of the robot arm by 180° (**fig. S5A**). Characterization of the guidewire's behavior during the transition (**fig. S5B**) is discussed in the Supplementary Materials.

Additional mode of steering control

Although the attraction and repulsion modes serve as the primary steering modes because of the intuitive control principles, they may not suffice for every possible case, especially when navigating in areas with unfavorable vascular anatomy for spatial positioning of the magnet due to workspace constraints. For such occasions, in which minimal motion of the robot arm is desirable, steering control of the magnetic guidewire can also be achieved through rotation of the magnet around its center, which corresponds to rotation of the end-effector around the axis 7 of the robot arm. We define the rotation angle (denoted α in **fig. S6A**) as the deviation of the central axis of the magnet from its unrotated state, in which the magnet is positioned at the zero angular position ($\varphi = 0$) with its axis aligned with the undeformed (straight) tip of the guidewire from some working distance d (**fig. S6A**). The tip deflection angle θ varies with the magnet's rotation angle α ranging from –180° to 180°, as well as the normalized working distance d / R, as characterized in **fig. S6B**. When the magnet rotates clockwise ($\alpha < 0$) from the unrotated state, the guidewire tip bends counterclockwise ($\theta > 0$); when the magnet rotates counterclockwise ($\alpha > 0$), the guidewire tip

bends clockwise ($\theta < 0$), just as two meshed gears turn in opposite directions. For the magnet positioned at either $-135° < \alpha < -90°$ or $90° < \alpha < 135°$, we define another useful steering mode, so-called the oblique repulsion mode (**fig. S6A**), which helps to deflect the guidewire tip up to around 90° at the normalized working distance of 2.64 (**fig. S6B**).

Size of the actuating magnet

The mappings between the position and orientation of the magnet and the behavior of the guidewire's distal tip presented in **Fig. 3C** and **fig. S6B** provide guidance on how to manipulate the magnet to achieve desired states of the guidewire. We define the range of working distances for the magnet in the attraction/repulsion mode as $2.64 \leq d / R \leq 3.67$ in terms of the normalized distance (**Fig. 3C**). The lower and upper boundaries correspond to the points along the central axis of the magnet at which the magnetic flux density is 80 mT and 30 mT, respectively, according to Eq. (4) (**fig. S3B**). Within this range, the tip deflection angle can reach up to around 120° in the attraction mode and around 90° in the repulsion mode as shown in **Fig. 3C**. If we allow the magnet to approach the patient's head as close as 70 mm (in terms of the distance from the magnet surface to the target vasculature) in the scenario discussed above (**Fig. 3A**), the size of the smallest possible magnet is calculated to be around 85 mm in terms of both diameter and thickness ($R = 42.5$ mm). If we increase the minimum allowable distance (between the magnet surface and the target vasculature) to 85 mm, including some safety margins (around 20 mm from the head surface), the required diameter/thickness of the magnet becomes around 100 mm ($R = 50$ mm), which is considered the ideal size of the magnet to be used in realistic clinical settings. Hence, a cylindrical magnet with size of 100 mm was employed and mounted on the most distal joint/link of the robot arm with its magnetic moment aligned perpendicularly to the joint axis.

Teleoperation interface for the robot arm

Our teleoperation interface enables spatial positioning of the magnet through real-time position control of the robot arm's end-effector using a joystick controller with a 6-DOF knob with which the operator can intuitively manipulate the actuating magnet as illustrated in **fig. S7A**. We describe the configuration of the robot arm using a joint-space vector $\mathbf{q} \in \mathbb{R}^7$ which represents the joint angles of the 7 revolute axes. The position and orientation of the end-effector frame ({e} in **Fig. 2A**) relative to the robot arm's base frame ({b} in **Fig. 2A**) are defined by a task-space vector $\mathbf{x} \in \mathbb{R}^6$ with its first three components representing the position and the last three components representing the orientation. The differential kinematics, or the relation between the small change in the joint positions $\delta\mathbf{q}$ and the corresponding change in the end-effector pose $\delta\mathbf{x}$, can then be written as

$$\delta\mathbf{x} = \frac{\partial \mathbf{f}(\mathbf{q})}{\partial \mathbf{q}} \delta\mathbf{q} = \mathbf{J}(\mathbf{q})\delta\mathbf{q}\,, \tag{5}$$

where $\mathbf{J}(\mathbf{q}) \in \mathbb{R}^{6\times7}$ is the Jacobian, or the partial derivatives of the forward kinematics defined by a mapping $\mathbf{x} = \mathbf{f}(\mathbf{q})$ with $\mathbf{f}$ denoting a nonlinear vector function. Upon the operator's joystick manipulation, 6-DOF motion commands are produced as a combined set of incremental motions (translations and rotations) in each DOF, which are scaled and converted into the end-effector's linear and angular motions in the task-space coordinates. The motion

commands for the end-effector $\delta\mathbf{x}$ are then transformed into the joint commands $\delta\mathbf{q}$ by multiplying the pseudo-inverse of the Jacobian $\mathbf{J}^{\dagger}(\mathbf{q})$:

$$\delta\mathbf{q} = \mathbf{J}^{\dagger}(\mathbf{q})\delta\mathbf{x} = \mathbf{J}^{\mathrm{T}}(\mathbf{q})\left(\mathbf{J}(\mathbf{q})\mathbf{J}^{\mathrm{T}}(\mathbf{q})\right)^{-1}\delta\mathbf{x}\,, \tag{6}$$

which returns the minimum-norm solution for redundant manipulators like the one used in the present work by minimizing the two-norm $\|\delta\mathbf{q}\| = \sqrt{\delta\mathbf{q}^{\mathrm{T}}\delta\mathbf{q}}$ (27). The joint commands are added to the current joint positions to get new joint position values, which are sent to the robot arm controller (i.e., control cabinet in **Fig. 1**) to execute the motion that achieves the desired configuration of the robot arm.

In vitro verification with anatomical models

For validation of the developed telerobotic neurointerventional platform, we evaluated its steering and navigational performance in vitro with anatomical models that replicate the human intracranial arteries. As part of benchtop verification, we first demonstrated our system's capability to guide selective navigation in different branches of cerebral arteries in a 3D neurovascular phantom under real-time optical imaging (**fig. S7B)** through telerobotically controlled magnetic manipulation (**fig. S7C**), as presented in **movie S1**. The task was performed in the presence of virtual C-arm models implemented in the robot arm's task space to simulate the workspace constraints in clinical settings for complex neurovascular interventions under biplane fluoroscopy (**fig. S7D**). In addition to the C-arm models, a virtual human patient on the operating table was also modeled in the robot's task space to ensure that the robot arm manipulation could be performed without collisions. The 3D neurovascular phantom was accessed from the left internal carotid artery (ICA; **fig. S8** for detailed vascular structure) with the magnetic guidewire and the microcatheter, which were advanced up to the left ICA bifurcation (A1-M1 junction) using the remotely controlled advancing unit. After positioning the actuating magnet to direct the guidewire tip toward the A1 segment of the left anterior cerebral artery (ACA; **fig. S8**) through repulsive steering, as shown in **fig. S7C** (00:01), the guidewire was advanced up to the anterior communicating artery (ACoA; **fig. S8**) and then to the M1 segment of the right middle cerebral artery (MCA), as shown in **fig. S7B** (00:03) and **movie S1** (00:00~00:03). Then, the guidewire was magnetically steered and manipulated within the confined space of ACoA complex to selectively reach the right and left A2 segments, as shown in **fig. S7B** (00:14~00:39) and **movie S1** (00:03~00:44), which demonstrates our system's capability to control the magnetic guidewire remotely and precisely to navigate distal branches in the complex cerebral vasculature.

Then, for testing in a more realistic setting, we used a human head phantom with cranial housing and intracranial arteries (**Fig. 4A** and **B**) under real-time x-ray fluoroscopy. Given that the vasculature between the proximal intracranial ICA to the MCA bifurcation (**fig. S2** for neurovascular anatomy) is the most common site for stroke or aneurysm intervention (6, 28), we chose to demonstrate magnetic steering and navigation in the left MCA of the phantom. First, to identify the 3D structure of the targeted vasculature, a series of images was obtained from 3D rotational angiography, and the data were reconstructed into a 3D vessel model (**Fig. 4C**) that allowed for a detailed view of the vascular structure from different perspectives. Based on the reconstructed 3D vascular model, a semi-anteroposterior projection was chosen to provide clear view of all the important anatomical landmarks along the path including the carotid siphon — the U-shaped part of the ICA between the cavernous (C3)

and supraclinoid (C4) segments — with an aneurysm, the ICA bifurcation (A1-M1 junction), and the MCA bifurcation (M1-M2 junction), as annotated in **Fig. 4C**. The corresponding C-arm configuration, which is physically and virtually visualized in **Fig. 4**, **E** and **F**, respectively, was with caudal angulation of 14° (CAU 14°) and right anterior oblique rotation of 44° (RAO 44°; **fig. S9** for the C-arm nomenclature). The 3D vessel model was also used for preprocedural planning and simulation of the robot arm's motion, path, and configuration for spatial positioning of the actuating magnet to steer the magnetic guidewire at acute-angled corners or bifurcation points. The cranial housing of the head phantom (**Fig. 4A**) imposed realistic workspace constraints of the patient geometry (**Fig. 3A**). Again, the C-arm and the human patient models in the robot's virtual task space (**Fig. 4F**) helped to ensure that the robot manipulation could be performed without collisions.

As shown in **Fig. 4D** and **movie S2**, the magnetic guidewire was naturally visible under x-ray, as clearly as standard neurovascular guidewires, due to the embedded radiopaque magnetic particles. Starting from the left proximal ICA, the guidewire was first advanced to reach the carotid siphon at which a saccular aneurysm (with an inner diameter of 4 mm) was present. As the guidewire entered the ascending part of the carotid siphon in the absence of magnetic steering, the straight tip of the guidewire was naturally directed toward the aneurysm (at the apex of the carotid siphon) as can be seen in **Fig. 4D** (00:04) and **movie S2** (00:00~00:04). To prevent the guidewire tip from contacting the inner wall of the aneurysm upon further advancement, the actuating magnet was placed above the carotid siphon for repulsive steering (**Fig. 4**, **E** and **F**; 00:15), under which the guidewire tip was directed toward the descending segment of the carotid siphon so that it could pass the acute-angled corner without touching the aneurysm, as shown in **Fig. 4D** (00:15) and **movie S2** (00:04~00:15). The guidewire was then further advanced up to the superior M2 segment under attractive steering at the ICA bifurcation (A1-M1 junction) to direct the distal tip toward the M1 branch, as shown in **Fig. 4D** (00:24~00:27) and **movie S2** (00:15~00:27). The guidewire was then retracted back to the MCA bifurcation while flipping and repositioning the magnet for repulsive steering to reorient the guidewire tip toward the inferior M2 segment, after which the guidewire was advanced until it reached the end of the inferior M2 segment, as shown in **Fig. 4D** (00:40~00:48) and **movie S2** (00:27~00:49).

This set of demonstrations with in vitro phantoms verifies that magnetic steering and navigation in intracranial arteries can be achieved with minimal motion of the actuating magnet through teleoperation of the system under visual feedback from real-time imaging and visualization in the presence of realistic workspace constraints. We also found that the magnetic guidewire could be steered effectively in the complex 3D vasculature without its view for state observation being blocked or compromised by the actuating magnet. Given the steering principles based on a single magnet described in **Fig. 3B** and **figs. S5A** and **S6A**, it is unlikely that the view of the guidewire's steerable tip is blocked or interrupted by the actuating magnet during the steering task. This is because the plane of bending (on which the guidewire tip deflection is induced by the in-plane magnet motion) and the plane of view (on which the guidewire tip deflection is being observed) should be aligned with each other for optimal state observation. Hence, the argument that the magnet would not block the view of the guidewire tip during steering should generally hold for any vascular structure, provided that a suitable projection (the plane of view) was chosen for state observation of the guidewire in the target vasculature.

Telerobotically-assisted aneurysm coil embolization

We further demonstrate our system's capability to telerobotically assist therapeutic procedures that are commonly performed in endovascular neurosurgery such as coil embolization for treating intracranial aneurysms and clot retrieval thrombectomy for treating ischemic stroke. For endovascular treatments of aneurysms or stroke, therapeutic devices such as embolization coils or a stent retriever need to be delivered to the target lesion through a microcatheter. Aneurysms are localized points of vessel-wall weakening that create saccular or fusiform dilatations of the vessel wall leading to risk of rupture (29). Intracranial aneurysms are typically treated endovascularly by deploying coils through a microcatheter to promote thrombosis within the aneurysm to eliminate blood flow into the dilated area, thereby reducing the risk of rupture (30). To demonstrate robotically assisted aneurysm coiling with our developed telerobotic neurointerventional platform, we used the same neurovascular phantom with multiple aneurysms (**fig. S8**) that was used for benchtop verification in **fig. S7** and **movie S1**. The most distal (difficult-to-reach) aneurysms at the left and right MCA bifurcations (M1-M2 junctions) were chosen for demonstration.

To reach the target aneurysm at the left MCA bifurcation, the magnetic guidewire was first steered in the left internal carotid artery (ICA), where a large saccular aneurysm (with an inner diameter of 9 mm) was present in the carotid siphon (**fig. S8**). To cross the large gap within the aneurysm while avoiding contact with the inner wall of the aneurysm, the guidewire was manipulated under repulsive steering and advanced to the ICA bifurcation (A1-M1 junction) as shown in **Fig. 5A** (00:00~00:12) and **movie S3** (00:00~00:15). Then, the guidewire was directed toward the left M1 segment to make a 90° turn under attractive steering, without touching the small aneurysm (with an inner diameter of 5 mm) located at the distal ICA (C4 in **fig. S8A**), and then advanced up to the target aneurysm (with an inner diameter of 7 mm) at the left MCA bifurcation (M1-M2 junction) as shown in **Fig. 5A** (00:24) and **movie S3** (00:15~00:28). The guidewire was then directed toward the inferior M2 segment through repulsive steering to avoid touching the target aneurysm upon further advancement, as shown in **Fig. 5A** (00:34~00:38) and **movie S3** (00:28~00:38). Then, the microcatheter was advanced up to the M1-M2 junction, after which the magnetic guidewire was retracted so that the microcatheter's distal tip could be placed inside the target aneurysm, as shown in **Fig. 5A** (00:46~00:55) and **movie S3** (00:38~00:58). After full retraction and withdrawal from the microcatheter, the magnetic guidewire was replaced by an embolization coil device with its push wire engaged with the guidewire advancing unit. After the device exchange, the coil was advanced and delivered through the microcatheter into the target aneurysm under the joystick control of the advancing unit, as shown in **Fig. 5B** (00:04~00:30) and **movie S3** (after 00:58). The real-time x-ray fluoroscopy confirmed successful coil placement in the target aneurysm.

We performed another aneurysm coiling with our telerobotic neurointerventional system in the most distal aneurysm at the right MCA bifurcation, as presented in **fig. S10A** and **movie S4**. Two large aneurysms were present in the neurovascular phantom (**fig. S8**), one with an inner diameter of 9 mm at the corner in the right ICA (C2) and the other with an inner diameter of 7.5 mm at the carotid siphon (C3-C4). Both of them were imposing navigational challenges due to their presence at the acute-angled corners. The C-arm configuration was determined to provide a semi-lateral projection with caudal angulation of 18° and right anterior oblique rotation of 60° (**fig. S9** for C-arm nomenclature). Starting from the

proximal ICA, the guidewire was magnetically steered using the oblique repulsion mode to cross the first aneurysm without touching its inner wall and then advanced up to the second aneurysm as shown in **fig. S10A** (00:00~00:10) and **movie S4** (00:00~00:15). Then, the guidewire tip was directed toward the distal ICA (C4) using repulsive steering to avoid contact with the second aneurysm, after which the guidewire was advanced until its distal tip reached the right MCA bifurcation (M1-M2 junction), as shown in **fig. S10A** (00:30) and **movie S4** (00:15~00:35). The guidewire was then further advanced to reach the inferior M2 segment under repulsive steering, as shown in **fig. S10A** (00:37~00:39) and **movie S4** (00:35~00:39), which was to ensure that sufficient distance from the target aneurysm to the guidewire tip was reserved for smooth microcatheter advancement over the guidewire. The microcatheter was advanced up to the target aneurysm while retracting the guidewire so that the microcatheter tip could be placed in the aneurysm sac, after which the guidewire was completely withdrawn, as shown in **fig. S10A** (00:39~00:56) and **movie S4** (00:39~00:58). An embolization coil was delivered through the microcatheter under the joystick control of the advancing unit until the aneurysm became densely packed with the coil, as shown in **fig. S10B** and **movie S4** (after 00:58). These results presented in **Fig. 5**, **fig. S10**, and **movies S3** and **S4** demonstrate the potential of our developed platform for telerobotically assisted endovascular coiling of cerebral aneurysms to treat or prevent hemorrhagic stroke with potentially reduced operative time, perioperative risk, and radiation exposure. The results also illustrate the versatile applicability of our system to endovascular coiling procedures for treating intracranial aneurysms in hard-to-reach areas of the cerebral vasculature.

Telerobotically-assisted clot retrieval thrombectomy

Next, we investigated the feasibility of our system for endovascular treatment of ischemic stroke due to cerebral infarction. For the feasibility test, we used a simulated, nonbiological blood clot to create occlusion in the M1 segment — one of the most common sites for a thrombus to lodge to cause cerebral ischemia (6) — in the right middle cerebral artery (MCA) of the same neurovascular phantom we used for demonstrating the aneurysm coiling procedures. The artificial clot used in our experiment had similar mechanical and viscoelastic properties to a real blood clot (31). Given that the clot by itself was not visible under x-ray, the magnetic navigation and clot retrieval procedures were initially performed under real-time optical imaging to better visualize the whole process (x-ray results are also presented below), as shown in **Fig. 6** and **movie S5**. Steering control and manipulation of the magnetic guidewire to the occluded site were similar to what was described for the previous demonstration of guidewire navigation in the same path presented in **fig. S10A** and **movie S4**, until the distal tip of the guidewire reached the clot, as shown in **Fig. 6A** (00:00~00:34) and **movie S5** (00:00~00:34). The guidewire was further advanced so that the distal tip thrust itself into the tiny gap between the clot and the vessel wall, under careful control of the guidewire advancing unit to avoid touching the inner wall of the first aneurysm at the corner, as shown in **movie S5** (00:34~00:46). The guidewire tended to buckle inside the aneurysm upon further push, due to the high resistance from the clot, as can be seen in **movie S5** (00:46~00:49). To avoid buckling by adding more mechanical support to the guidewire, the microcatheter was carefully advanced up to the clot while at the same time controlling the guidewire, after which the guidewire was advanced to pass through the artificial clot, as can be seen in **Fig. 6A** (01:35) and **movie S5** (00:50~01:37). With the aid of magnetic steering of the guidewire at the MCA bifurcation, the microcatheter was placed across the occlusion such that its dis-

tal end was positioned distal to the thrombus, as shown in **Fig. 6A** (01:42) and **movie S5** (01:38~01:49).

After withdrawing the guidewire, mechanical thrombectomy was performed to retrieve the clot using a commercially available revascularization device (i.e., a stent retriever; see Materials and Methods for details). Delivery of the stent retriever was performed manually following the standard procedure after inserting the stent introducer sheath into the hub of the microcatheter. The stent push wire was advanced within the microcatheter until the distal markers of the stent retriever lined up with the distal end of the microcatheter, as shown in **movie S5** (00:00~00:20 of the second part). Then, the microcatheter was carefully withdrawn under the joystick control of the catheter advancing unit while fixing the stent push wire to maintain the position of the stent until the distal end of the microcatheter was just proximal to the thrombus, thereby fully deploying the stent across the thrombus, as shown in **Fig. 6B** (00:42) and **movie S5** (00:20~00:46). After confirming the stent deployment from the real-time imaging, the microcatheter and the stent as a unit were withdrawn to retrieve the clot and revascularize the occluded site (M1), as shown in **Fig. 6B** (00:48~00:52) and **movie S5** (00:47~00:56).

We repeated the clot retrieval procedure under real-time x-ray fluoroscopy as shown in **fig. S11**, **A** and **B**. It is worth noting that the infarcted right MCA was missing on the digital subtraction angiography (i.e., roadmap) images due to the occlusion in M1 blocking contrast flow (see corresponding optimal images in **fig. S11**, **C** and **D)**, which is the same phenomenon observed in real stroke cases. The overall procedure and the workflow were similar to the previous demonstration in **Fig. 6**. However, greater distal migration of the clot was observed while advancing the guidewire and placing the microcatheter, as shown in **fig. S11C** (01:02~01:58), possibly due to the presence of pulsatile flow generated by the peristaltic pump. In contrast to the previous demonstration in which the stent retriever device was manually manipulated, this time we used the advancing unit and the joystick controller to manipulate both the stent retriever and the microcatheter when deploying the stent and retrieving the clot (**fig. S11**, **B** and **D**) to avoid radiation exposure during the procedures. Only the device exchange was done manually, after removing the guidewire from the microcatheter, by engaging the stent push with the guidewire advancing unit. The results presented in **Fig. 6** and **fig. S11** demonstrate the potential of our system for telerobotically assisted clot retrieval thrombectomy for treating ischemic stroke.

In vivo validation with porcine artery model

The series of in vitro verification results presented above have demonstrated our system's steering and navigational capabilities in clinically relevant settings for image-guided neurointervention using x-ray fluoroscopy, with realistic workspace constraints for the robot arm taken into account. The phantom studies allowed us to assess the physical and mechanical properties of the magnetic guidewire, such as radiopacity, stiffness, lubricity, and durability, in addition to the steering performance in the simulated human neurovascular anatomy with clinically challenging tortuosity and disease states. While indispensable, performance evaluation in vitro based on anatomical models in general does not fully characterize all clinical experiences, outcomes, and risks (4). To verify our system's steering and navigational performance under realistic in vivo conditions while assessing the viscoelastic and physiological responses of blood vessels during the endovascular manipulation, we conducted animal testing using a porcine model.

Although pigs have been considered as excellent experimental animals for medical research because of the similarities between human and porcine biology (32), their head and neck geometry and intracranial arterial anatomy are quite different from those of humans. For example, in the pig exists a small and dense network (plexus) of interconnected vessels called rete mirabile, from which the internal carotid artery originates intracranially. Furthermore, the porcine intracranial arteries are much smaller in diameter (around 1 mm or less) than the human intracranial arteries (around 2~5 mm), and two middle cerebral arteries (MCAs) emerge from the internal carotid artery (ICA) in each hemisphere of the pig unlike human anatomy. In a pivotal paper, Carniato et al. reported an animal model for in vivo evaluation of neuroendovascular devices based on the porcine brachial artery in the flexed forelimb position, which is to replicate the clinically challenging tortuosity of the human ICA at the carotid siphon (17). Following the reported protocol for the porcine brachial artery tortuosity model (see Materials and Methods for details), we evaluated our system's steering and navigation performances in the porcine brachial artery with accentuated tortuosity in the maximally flexed position, as presented in **Fig. 7** and **movie S6**.

First, a series of images of the target vasculature in the right forelimb was obtained from 3D rotational angiography while injecting the contrast agent through a 7-Fr guide catheter positioned in the brachial branch of the subclavian artery in the flexed forelimb position (**Fig. 7A**). The acquired images were then reconstructed into a 3D vessel model (**Fig. 7B**), which allowed for a detailed view of the vascular structure from different perspectives (**movie S7**) for preprocedural planning. Based on the reconstructed 3D vessel model, a semi-anteroposterior projection was chosen to provide clear view of all the side branches (numbered in **Fig. 7**, **B** and **D**) present along the target path in the brachial artery, through the C-arm configuration with cranial angulation of 4° and left anterior oblique rotation of 34° (**Fig. 7C**). Then, digital subtraction angiography was performed to visualize the target vasculature on the live fluoroscopy images from the chosen projection (**movie S6**). It is worth noting that the vessel roadmap was taken from the angiography data and graphically overlaid on top of the fluoroscopic images in **Fig. 7D** for clear representation and that the guidewire contour was highlighted to make it clearly visible in the small panels of the figure (**movie S7** for raw data).

The first two side branches (1 and 2 in **Fig. 7**, **B** and **D**) in the proximal brachial artery were located at the acute-angled corners, into which the straight tip of the guidewire would have naturally been directed if it were not steered by the externally applied magnetic fields. To prevent the guidewire tip from entering the undesired branch at each corner, the position and orientation of the actuating magnet were identified such that the guidewire tip could be steered toward the desired path, using the 3D vessel model implemented in the virtual task space of the robot arm for real-time visualization and motion planning (**Fig. 7E**). The corresponding end-effector pose and the configuration of the robot arm were prescribed so that the actuating magnet could readily be positioned upon the operator's command from the remote-control console to steer the magnetic guidewire, as shown in **Fig. 7**, **D** to **F** (00:06~00:20) and **movie S6** (00:00~00:30). To demonstrate selective navigation in different branches in the distal area, the magnet pose was prescribed such that the guidewire tip could be steered to selectively reach branches 4 and 5 consecutively, as shown in **Fig. 7**, **D** to **F** (00:45~01:04) and **movie S6** (00:30~01:05). Lastly, the guidewire tip was advanced into the tortuous area with a 360-degree turn followed by another sharp turn before the goal location. The guidewire tip was initially directed toward the entering curve of the 360-degree

turn, repelled sideways at the 90-degree corner to make its shape favorable for the sharp turn, and then advanced until it reached the goal, as shown in **Fig. 7**, **D** to **F** (01:33~01:37) and **movie S6** (01:04~01:41). It is worth noting that the x-ray fluoroscopy was intermittently stopped while repositioning the robot arm, as can be seen in **movie S6**, to minimize the radiation exposure to the animal as well as the staff present in the catheterization laboratory.

One noticeable difference observed from the in vivo testing above was that the guidewire in the proximal area tended to deviate more greatly from the vessel roadmap as it proceeded more distally along the path, as shown in **Fig. 7D**, which was rarely observed in the silicone vessels during our in vitro phantom studies presented earlier. This can be attributed to the deformation of the soft blood vessels due to the stiff guidewire, which normally occurs during endovascular navigation with standard guidewires. Nonetheless, the deformation of the proximal vessels had no effect on the steering of the distal tip of the magnetic guidewire. Except for this apparent deviation of the guidewire from the roadmap, the behavior of the magnetic guidewire in the tortuous porcine brachial artery during the steering and navigational task in vivo was close to that observed in the silicone phantoms, in terms of the device performance and characteristics such as steerability, lubricity, and durability.

Notably, no adverse biological or physiological responses such as thrombosis or complications due to endothelial injury such as vessel dissection or perforation were observed during the demonstrated steering and navigational task in vivo. In addition, no adverse events were observed due to the presence of the magnetic field during the setup, use, and completion of the experiment. These results validate the safety and effectiveness of the telerobotically controlled magnetic steering and navigation in complex and tortuous vasculature in realistic in vivo conditions.

Usability testing and learning curve assessment

Our system allows the operator to remotely control the magnetic guidewire by manipulating the actuating magnet through the robot arm while advancing/retracting the guidewire along with the microcatheter for endovascular navigation and intervention. Although the primary role of the magnetic guidewire is the same as that of conventional ones, in terms of enabling access to the target lesion to initiate interventional procedures, the way in which the magnetic guidewire is manipulated for steering purposes is quite different from the manually controlled passive guidewires based on the twisting maneuver. Hence, new users must be trained to learn how to drive the robot arm and the advancing units with the given teleoperation interface to be able to manipulate the magnetic guidewire and microcatheter under feedback from real-time imaging and visualization.

To assess the learning curve and evaluate the user experience, we conducted a pilot study with 6 participants who had no prior experiences with the developed telerobotic manipulation platform. The novice group consisted of 2 engineers with expertise in robotically assisted image-guided therapy and 4 experienced neurointerventionalists. For this learning curve assessment, we used the 3D neurovascular phantom that was used for the aneurysm coiling and clot retrieval demonstrations in **Figs. 5** and **6** in the catheterization laboratory equipped with a standard neurointerventional angiography suite (**fig. S15**, **A** and **B**). The given task for learning curve assessment was endovascular navigation along the previously demonstrated path in **Fig. 5**, from the left proximal internal carotid artery (ICA) to the inferior M2 segment of the left middle cerebral artery (MCA), as shown in **fig. S15C**. Learning curves

were obtained by tracking procedural time taken for the defined task as a metric for performance over 15 consecutive trials for each participant. Prior to data collection from the novice group, procedural time was measured from 2 experienced users (over 15 consecutive trials for each) for comparison. As shown in **fig. S15D**, the experienced group displayed relatively consistent performance with small deviations over the repeated trials. On average, it took 47.8 ± 12.2 s (mean ± standard deviation) for the experienced group to complete the given task. The novice group was trained by the experienced users to learn the magnetic steering principles. As part of the training curriculum, each novice performed 3 practice runs to familiarize themselves with real-time teleoperation of the system under the guidance of the experienced users before starting to track the procedural time.

The average learning curve of the novice group is presented in **fig. S15E**, with the individual learning curves presented as well in **fig. S16**, where each dataset was fitted with a logarithmic curve. The average learning curve was short, exhibiting fast decay of the measured time over the number of completed trials. On average, the novice group was able to reduce the procedural time by half after around 5 trials and reach the similar proficiency level of the experienced group after around 12 trials (**fig. S15E**). The average of the entire trials (n = 90; 15 trials from each of the 6 novices) was 92.8 ± 61.7 s, which was almost double that of the experienced group with much greater deviations. One of the main difficulties faced by the novices while performing the given task was the presence of the large aneurysm at the acute-angled corner in the carotid siphon, which imposed a navigational challenge that turned out to be the main rate-limiting factor. Even though the guidewire tip was seemingly directed correctly toward the desired branch (C4; see **Fig. 5A**), it tended to exit the desired branch and inadvertently fall into the aneurysm upon further advancement of the guidewire when the actuating magnet was wrongly positioned or oriented, producing insufficient repulsive steering torque. This navigational challenge, however, became certainly manageable after a few trials and could eventually be overcome by every participant, leading to the time reduction. The average of the last 5 trials of the novice group (n = 30; last 5 trials from each of the 6 novices) was 50.1 ± 17.4 s, which was close to the average procedural time (47.8 ± 12.2 s) of the experienced group (n = 30; 15 trials from each of the 2 experienced users). We found no statistically significant difference between the two datasets from Welch's t-test (two-sample t-test assuming unequal variances). These results verify that our designed system requires a relatively short period of time for new users to learn how to navigate clinically challenging anatomy with the magnetic guidewire through real-time teleoperation of the robot arm and the advancing unit.

Comparison with conventional guidewires

Lastly, we evaluated the steering and navigational performance of our telerobotically controlled magnetic guidewire in comparison with that of a manually manipulated conventional guidewire by an experienced neurointerventionalist as shown in **Fig. 8A**. For comparison, the interventionalist performed the same navigational task in **fig. S15C** using a standard 0.014-inch neurovascular guidewire (Synchro 2, Stryker) with a shapeable tip for steering purposes (**Fig. 8**, **B** and **C**). The time it took for the interventionalist to complete the task was measured over 10 consecutive trials (**Fig. 8D** and **movie S7**). Before measuring time, the interventionalist was given several practice trials to familiarize himself with the given vascular anatomy and to produce steady-state performances for fair comparison.

One of the navigational challenges encountered was the acutely angled left carotid siphon with a large aneurysm (Aneurysm 1 in **Fig. 8B**), where the 90°-angled tip of the guidewire frequently failed to pass the sharp corner due to the presence of large open space inside the aneurysm (**movie S7**). Crossing this corner with the pre-shaped guidewire was successful only in 5 trials (Trials 3, 4, 5, 6 and 10 in **movie S7**) out of the 10 consecutive trials. In those 5 successful trials, however, the guidewire's pre-bent tip was prone to fall into the posterior communicating artery (PCoA; **fig. S8A**) upon further advancement after passing the aneurysm, which was unintended. When the guidewire continuously failed to cross the corner (Trials 1, 2, 7, 8, and 9 in **movie S7**), the interventionalist chose to loop the guidewire in the aneurysm to access the desired branch. However, this guidewire looping maneuver can be potentially dangerous, especially in ruptured or in partially thrombosed aneurysms due to the risk of bleeding or displacement of thrombus (33). We also noticed that the pre-bent tip of the guidewire occasionally latched onto a small aneurysm (Aneurysm 2 in **Fig. 8B**) located at the distal end of the supraclinoid (C4) ICA, as can be seen in **Fig. 8F** (00:42) and **movie S7** (00:16 in Trial 5 and 00:42 in Trial 7). At the MCA bifurcation with another aneurysm (Aneurysm 3 in **Fig. 8B**), the pre-shaped guidewire also frequently failed to access the desired inferior M2 branch, encountering a similar navigational challenge due to the presence of an aneurysm at the acutely angled corner in 6 trials (Trials 3, 4, 5, 7, 8, and 10 in **movie S7**). In these 6 trials, accessing the desired branch required another potentially risky looping maneuver to pass the corner with the aneurysm, as shown in **Fig. 8F** (00:58~01:14). Overall, the manually controlled passive guidewire showed somewhat unpredictable behavior in those clinically challenging areas, causing several unintended or undesirable incidents such as the guidewire tip colliding with aneurysms, looping inside aneurysms, or falling into undesired branches. The number of such undesirable events encountered while manually manipulating the guidewire was counted for each trial as presented in **Fig. 8E**.

Unlike the manually controlled passive guidewire, the telerobotically controlled magnetic guidewire enabled access to the clinically challenging branches without requiring a dangerous looping maneuver in the aneurysm sac and obviated unexpected or unintended guidewire tip movements, as can be seen in **Fig. 8**, **E** and **G**, and **movie S8**. Overall, the average time to complete the given task was shorter with the telerobotically controlled magnetic guidewire (42.9 ± 10.5 s) when compared with the manually controlled passive guidewire (63.7 ± 22.4 s), and we found statistically significant difference in the procedural time between the two approaches ($P < 0.05$) during the 10 consecutive trials. We assessed the operator's workload in each trial using the NASA Task Load Index (34) as presented in **fig. S17**. We found statistically significant ($P < 0.05$) reduction in the operator's workload in terms of the mental demand, temporal demand, performance, effort, and frustration with the telerobotically controlled magnetic guidewire when compared with the manually controlled passive guidewire.

These experimental results with quantitative comparison data demonstrate that the telerobotically controlled magnetic guidewire can help to reduce the procedural time as well as the potential risk of vascular perforation or aneurysm rupture while allowing for the operator to work remotely to minimize the radiation exposure. The results also indicate that the telerobotically controlled magnetic navigation could be more predictable and less dependent on the experience and skill of the operator when compared with the manually controlled passive guidewire. This performance comparison was conducted by only one interventionalist and hence further studies based on a multi-user trial will be required to confirm the comparison results. Nonetheless, given the technical challenges and functional limitations inherent in

conventional guidewires with shapeable/pre-shaped distal tips, we believe that the demonstrated steering and navigational capabilities of our telerobotic neurointerventional system suggest its potential for improving the quality of endovascular neurosurgery by enabling safer and quicker access to hard-to-reach lesions in the complex neurovasculature.

Discussion

In this work, we have introduced a telerobotic neurointerventional platform with a 7-DOF robot arm employed for steering control of the magnetic guidewire and a set of motorized linear drives for precise control of the guidewire or microcatheter advancement, which are controlled remotely under visual feedback from real-time imaging. In the series of benchtop testing, we have shown that our system performs as intended in simulated clinical environments representing the human neurovascular anatomy with clinically challenging tortuosity and disease states such as multiple aneurysms and vascular occlusions. Through the preclinical testing, we have also demonstrated the safety and effectiveness of our developed system for its use in realistic in vivo conditions as well. We have further demonstrated our system's ability to assist therapeutic procedures for endovascular treatments of aneurysms and ischemic stroke in difficult-to-reach areas of cerebral arteries with clinically challenging anatomies. To the best of our knowledge, such telerobotically assisted aneurysm coil embolization and clot retrieval thrombectomy in the complex cerebral vasculature have not been demonstrated with previously reported vascular robotic systems in the literature including the commercial ones discussed earlier (5, 9-14, 35-39). The series of demonstrations in this paper have validated the quantitative analyses presented in **Fig. 3** and **fig. S3** for determining the right size of the actuating magnet for clinical use. Further increasing the size of the actuating magnet may allow greater safety margins in terms of its working distance, but the use of a larger magnet would likely affect the flexibility and dexterity of the robot arm due mainly to the greater constraints in terms of the available workspace in cluttered environments. Because it is known that the magnetic susceptibility of biological tissues in the human head causes negligible effect (below 1%) on the actuating field strength (40), the magnet size verified from the series of benchtop verification would likely be applicable to clinical scenarios.

It is worth noting that the concept of magnetically guided intravascular devices has existed for decades (41-46). Despite the long and checkered history of using magnetism to direct intravascular devices (5), there are currently no viable magnetic guidewire/catheter products or commercially available robotic systems to magnetically manipulate such devices for neurovascular applications, where the active steering capability is most needed. Several magnetic guidewire products were introduced for coronary and peripheral interventions in the past by Stereotaxis Inc., in the form of "magnet-tipped" guidewires with a small magnet attached to the distal end tip (5, 38, 39, 47). There have been some similar variants proposed in the research domain, with a few magnets embedded in the distal portion of the guidewire (35). Such magnet-tipped guidewires, however, entail potential risks of embolization because the magnet at the end could break off (48). Furthermore, lacking the ability to conform to the given environment, the rigid and stiff tip of magnet-tipped guidewires could make it particularly challenging to work through narrow and winding pathways in the distal cerebral vasculature. More importantly, the use of finite-sized, rigid magnets in a thin, flexible device often leads to discontinuous dimensions or mechanical properties along the magnet-tipped guidewire (36), which could significantly compromise its compatibility with other standard inter-

ventional devices (e.g., balloon catheters or microcatheters) that are indispensable for the endovascular treatment of aneurysms or stroke.

It is also worth noting that magnetic actuation based on a multi-DOF robot arm with a single magnet has been explored in previous studies for different applications such as magnetic capsule endoscopes (49-54). While the underlying mechanism of using magnetic torques and forces for device control is similar, the hardware design and control strategies of the previously reported systems are specific to their devices based on rigid, finite-sized magnets and hence not directly applicable to steering control of our magnetic continuum guidewire. When it comes to magnetic actuation systems of other types, there are commercialized platforms based on either a pair of large permanent magnets (such as Niobe® and Genesis® of Stereotaxis Inc.) or a set of multiaxial electromagnets (such as Magnetecs CGCI System and Aeon Phocus), which have been used mostly for cardiac electrophysiology to treat arrhythmia using magnetically controlled ablation catheters. While these commercialized systems could be used to control our magnetic guidewires, given the previously reported results based on magnet-tipped guidewires (5, 38, 39, 47), such heavy and bulky, hence immobile, platforms may not be ideal for endovascular neurosurgery, especially in the context of telestroke services. Furthermore, for the existing magnetic actuation systems, the available angulation for the monoplane C-arm is limited due to the confined space between the magnets − for example, the Niobe® system allows only 28° for the rotation of the C-arm in left or right anterior oblique projection (5). When compared with these existing magnetic actuation systems, our compact single-arm-based platform allows much wider C-arm rotation angles for better state observation as demonstrated in the series of benchtop and preclinical evaluations. Our developed platform based on a compact, lightweight robot arm could therefore suggest a cost-efficient alternative to those existing magnetic navigation systems in realizing robotic telesurgery for stroke intervention.

As demonstrated in **figs. S13** and **S14** (with related discussions presented in Supplementary Materials), our telerobotic neurointerventional system is also compatible with standard biplane fluoroscopy based on a pair of C-arms for simultaneous projections from two different angles. While single-plane imaging sufficed for most of the navigational tasks demonstrated in this paper, biplanar imaging offered benefits when identifying complex angulations of intracranial vessels as illustrated in **figs. S13** and **S14**. Although monoplane fluoroscopy can be used for stroke interventions (42-44), biplane imaging in general could provide better state observation of the guidewire in more complex vascular anatomies and hence potentially improve the operator's confidence, thereby leading to reduced intraoperative risk (55, 56). In this light, biplane imaging may be used when our system is operated in comprehensive stroke centers or tertiary hospitals that are equipped with biplane angiography suites. It is worth noting, however, that primary care centers in rural areas are not necessarily equipped with biplane systems due mainly to higher acquisition and maintenance costs. Recent studies (55-57) have shown that experienced neurointerventionalists can perform complex endovascular procedures such as mechanical thrombectomy equally safely and effectively on monoplane systems by utilizing angulation or rotation of the C-arm as they do the same procedures on biplane systems. For these reasons, in the context of telerobotic stroke intervention, we envision that our system could allow the experienced interventionalists at large institutions to perform surgical tasks remotely on patients at their local hospitals that are equipped with monoplane fluoroscopy systems.

There are some potential technical and logistical issues to consider for further translation of our proposed concept and developed system into the clinic. First, communication delays are inevitable in teleoperation systems due to signal propagation time and bandwidth constraints. Since our telerobotic system does not involve any dynamic motion of the robot arm, communication delays are nearly imperceptible to a human operator teleoperating the system from the remote-control console, which is a few meters away from the robot arm. For long-distance intervention in a robotic telesurgery scenario, however, the increased latency may negatively impact the steering control and navigational performance of our system. A recent study reported telerobotically assisted percutaneous coronary intervention in human patients that was performed remotely (32 km away) using the CorPath® GRX system under reliable network connection (58). The measured network delay was around 50 ms, and the authors reported that the delay did not result in any noticeable procedural or technical difficulties. We expect that advances in low-latency telecommunications (such as 5G wireless network) and improvements in network connectivity (59, 60) would help to realize long-distance telerobotic stroke intervention (2, 15) when combined with our system. Contingency plans must also exist for periprocedural complications to ensure the feasibility of remotely performed interventions through our proposed system. Even though the critical components of endovascular procedures can be performed remotely by a skilled neurointerventionalist (off-site expert) from another hospital, other personnel on-site will need to be present in the operating room for perioperative assistance from establishing vascular access and handling the C-arm machine to addressing any potential problems or complications that may arise before, during, or after the intervention (2, 3). In this light, the emerging telepresence or teleproctoring systems based on low-latency, high-resolution streaming technology, such as the Tegus system (61, 62), will greatly benefit both the off-site and on-site interventionalists by enabling bi-directional communication as well as high-resolution image transmission for real-time fluoroscopic images and visualization of robot configuration.

Secondly, similarly to other commercial vascular robotic systems with linear drives for guidewire and catheter advancement, the advancing unit of our system does not provide any tactile or haptic feedback. While the lack of tactile or haptic feedback is often considered one of the major drawbacks of existing vascular robotic systems (9), it should be noted that interventionalists rely mostly on visual feedback when manually manipulating a conventional guidewire. Some recent studies support this standpoint reporting that the lack of tactile feedback in the CorPath® GRX system did not result in any procedural challenges or adverse clinical outcomes (13, 14), mainly because of the ability to detect obstacles and friction visually by observing subtle changes in the shape and motion of the guidewire. Likewise, we believe that the tactile feedback may not be a critical factor for telerobotically performed endovascular navigation as the system provides the ability to stop advancing or retracting the guidewire and microcatheter immediately when the operator observes any undesirable behavior of the device from real-time fluoroscopic imaging. Nonetheless, we believe the implementation of force-sensing and haptic feedback technologies would help to improve the control interface and operator performance (3), which is therefore an area for future exploration.

From the presented in vitro and in vivo studies in this paper, we found that pre-operative imaging (3D rotational angiography and reconstructed 3D vessel models) can play a pivotal role in pre-procedural planning of the robot arm's motion, path, and configuration for spatial positioning of the actuating magnet to steer the magnetic guidewire at critical locations such as branching points or sharp corners in the target vasculature. We envision that pre-planned

robot motion for spatial positioning of the actuating magnet based on the pre-operative imaging data can help to make the system easier for interventionalists to use by reducing the operator's workload in real-time teleoperation of the robot arm with a joystick controller. This pre-procedural planning will also be crucial for future developments of the proposed robotic neurointerventional platform towards semi-autonomous or fully autonomous endovascular navigation in the complex neurovasculature based on magnetic manipulation. In doing so, model-based estimation and control of the magnetic soft continuum guidewire under the action of a single actuating magnet will also be an important area for future development, given the practical constraints on real-time 3D shape sensing and tracking capabilities due to the projected challenges in miniaturizing sensors or reconstructing the 3D guidewire shapes from the standard mono- or bi-plane x-ray fluoroscopic images.

Materials and Methods

Telerobotic magnetic manipulation platform

A kinematically redundant, serial robotic manipulator with 7 revolute joints (LBR Med 14 R820, KUKA) was employed to manipulate a N52-grade cylindrical magnet ($B_{\text{re}} = 1.45$ T) with diameter and thickness of 100 mm (Hangzhou X-mag Inc.), which was mounted on the flange of the robot arm using a 3D-printed magnet housing. The net weight of the magnet and the fixture was 7 kg, and the center of the mass was 160 mm away from the robot arm's flange at the most distal link. The strength of the magnetic field from the magnet at this distance from the flange did not affect the position and torque sensors at each joint of the robot arm. The magnetic field and field gradient maps around the actuating magnet presented in **figs. S3A** and **S4** were generated using a commercial finite element analysis software (COMSOL Multiphysics® 5.2). The teleoperation control interface was designed based on the open-source libraries and tools such as MoveIt (for control of the robot arm based the joint commands $\delta\mathbf{q}$ computed from Eq. (6) and motion planning with collision avoidance) and RViz (graphical interface for real-time visualization of the robot arm) available in the Robot Operating System (ROS). A joystick controller with a 6-DOF knob (SpaceMouse® Pro Wireless, 3Dconnexion) was used for remote control of the robot end-effector for spatial positioning of the magnet.

Guidewire/microcatheter advancing unit

A pair of cylindrical brushed DC gearmotors with integrated encoders (High-power 12V, Pololu) was used to build the guidewire and microcatheter advancing units. Along with the DC motors, a motor driver (Dual VNH5019 Motor Driver Shield, Pololu) and a microcontroller board (Arduino Uno R3) were assembled in a 3D-printed motor housing (**Fig. 2A**). A pair of catheter advancers (QuikCAS Cardiodrive, Stereotaxis Inc.) was connected to the DC motors through flexible shafts to advance or retract the guidewire and the microcatheter, each of which was coupled to a 7-Fr introducer sheath/dilator (Destination® Guiding Sheath, Terumo) through a straight hemostasis valve connector (Qosina). The control interface for the guidewire/microcatheter advancing unit based on manipulation of the joystick buttons was implemented in the ROS environment to build an integrated teleoperation interface for the system.

In vitro testing setup

For demonstrations presented in **fig. S7**, **movie S1**, and **figs. S10** to **S13**, a 3D neurovascular model based on silicone vessels (Trandomed) was used. For demonstrations presented in **Fig. 4**, **movie S2**, and **fig. S14**, a human head phantom with cranial housing (Vascular Simulations Inc.) was used for realistic simulation of workspace constraints due to patient geometry. These anatomical models included both carotid and vertebral arteries and a complete circle of Willis in realistic dimensions. Multiple aneurysms with different neck morphologies, sizes and angulations from the carrier vessel were present on these anatomical models (**figs. S8** and **S14**). The silicone vessels were filled with a blood-mimicking fluid (Replicator Fluid, Vascular Simulations Inc.), along with a peristaltic pump to generate pulsatile flow, to simulate the friction between commercial hydrophilic guidewire/catheter surfaces and the real blood vessels. To demonstrate the repeatability of the navigational task in **Fig. 4** and **movie S2**, the experiment was repeated 5 times to evaluate the average time taken for completion and the standard deviation. To compare the interventionalist's performance with the telerobotically controlled magnetic guidewire and the manually controlled passive guidewire (**Fig. 8** and **movies S7**), a standard neurovascular guidewire (Synchro 2, Stryker) with a shapeable tip and an outer diameter of 0.014 inches (360 μm) was used. During the comparison, the operator's task load was also assessed via the NASA Task Load Index to compare the experienced task load from the two different approaches (**fig. S17**).

Telerobotically assisted therapeutic procedures

For the demonstrations of aneurysm coil embolization presented in **Fig. 5** with **movie S3** and in **fig. S10** with **movie S4**, bare platinum coils with an outer diameter of 0.0115 inches (290 μm) (Axium™ Prime, Medtronic) were used. For the demonstration of clot retrieval thrombectomy presented in **Fig. 6** with **movie S5** and **fig. S11**, a stent retriever device (Solitaire™ X Revascularization Device, Medtronic) was used to retrieve a simulated clot (ASIST™ Thrombus Simulant, Vascular Simulation Inc.). To create the occlusion in the left, a cylindrical plug of the thrombus simulant was deposited in the left ICA through an 8-Fr guide catheter with an inner diameter of 2.9 mm (Destination® Guiding Sheath, Terumo), and then a peristaltic pump was turned on to generate a pulsatile flow that carried the thrombus up to the M1 segment. A rotating hemostatic valve (Qosina) was connected to the microcatheter hub to tighten or loosen the introducer sheath of the embolization coils or the stent retriever when transferring those therapeutic devices into the microcatheter.

In vivo animal testing setup

A female Yorkshire swine of 56 kg was used for our animal testing. All procedures were conducted in accordance with the protocol approved by the Institutional Animal Care and Use Committee of University of Massachusetts Medical School and the Committee on Animal Care of Massachusetts Institute of Technology. Following the previously reported protocol (17), the swine was anesthetized and maintained with mechanical ventilation under continuous monitoring of its physiologic status. A 10-Fr hemostatic introducer (Check-Flo Performer® Introducer, Cook Medical) was placed in the right femoral artery by using a modified Seldinger technique. A 0.035-inch diagnostic guidewire (Glidewire, Terumo) was manually manipulated under x-ray fluoroscopy to reach the brachial branch of the right subclavian artery, and a 7-Fr guide catheter (Destination® Guiding Sheath, Terumo) was advanced manually over the diagnostic guidewire to be placed in the proximal brachial artery for contrast injection and angiography. After removing the diagnostic guidewire, the magnetic guidewire

was then advanced up to the proximal brachial artery to initiate the preclinical evaluation of magnetic steering and navigation through real-time teleoperation of the robot arm and the guidewire advancing unit.

Characterization of magnetic steering control

For the characterization data presented in **Fig. 3C**, **figs. S5B** and **S6B**, the guidewire's tip deflection angle θ was experimentally measured from the images taken with a high resolution camera (acA2440-35uc, Basler AG) while varying the distance d, the angular position φ, and the rotation angle α of the actuating magnet of cylindrical shape with diameter and thickness of 76.2 mm relative to the steerable tip. The distal portion of the magnetic guidewire was clamped and fixed with a nonmagnetic miniature gripper (Mark-10) to impose a fixed boundary condition while exposing only the distal 10-mm segment of the magnetically responsive tip that was free to deflect under the influence of the actuating magnet (**Fig. 3B**).

Statistical analyses

To demonstrate the repeatability of the in vitro navigation presented in **Fig. 4** with **movie S2** and **fig. S12** and the in vivo navigation presented in **Fig. 7** with **movie S6**, each of the experiments was repeated 5 times to evaluate the average and standard deviation of the time it took to complete the navigational task. Similarly, for repeatability of the telerobotically performed therapeutic procedures presented in **Fig. 5** with **movie S3**, **fig. S10** with **movie S4**, and **Fig. 6** with **movie S5**, each of the experiments was repeated 3 times to evaluate the average and standard deviation of the time it took for the demonstrated procedure. Welch's t-test (two-sample t-test assuming unequal variances) was performed to verify that there was no statistically significant difference in the performance between the experienced users and the trained novices, when comparing the average procedural time of the last 5 trials of the novice group ($n = 30$; last 5 trials from each of the 6 novices) with that of the experienced group ($n = 30$; 15 trials from each of the 2 experienced users) in **fig. S15E**. For the data presented in **Fig. 8D** with **movies S7** and **S8** to compare the steering and navigational performance of the manually controlled passive guidewire and the telerobotically controlled magnetic guidewire, each of the experiments was repeated 10 times to evaluate the average and standard deviation of the time it took for the interventionalist to complete the given task. In **Fig. 8D** and **fig. S17**, statistically significant differences are indicated with asterisks ($^*P < 0.05$) based on the P values obtained from paired t-tests (two-sample t-test for means).

References

1. S. S. Virani, A. Alonso, E. J. Benjamin, M. S. Bittencourt, C. W. Callaway, A. P. Carson, A. M. Chamberlain, A. R. Chang, S. Cheng, F. N. Delling, L. Djousse, M. S. V. Elkind, J. F. Ferguson, M. Fornage, S. S. Khan, B. M. Kissela, K. L. Knutson, T. W. Kwan, D. T. Lackland, T. T. Lewis, J. H. Lichtman, C. T. Longenecker, M. S. Loop, P. L. Lutsey, S. S. Martin, K. Matsushita, A. E. Moran, M. E. Mussolino, A. M. Perak, W. D. Rosamond, G. A. Roth, U. K. A. Sampson, G. M. Satou, E. B. Schroeder, S. H. Shah, C. M. Shay, N. L. Spartano, A. Stokes, D. L. Tirschwell, L. B. VanWagner, C. W. Tsao, Heart disease and stroke statistics – 2020 update: a report from the American Heart Association. *Circulation* **141**, e139-e596 (2020).

2. S. S. Panesar, J. J. Volpi, A. Lumsden, V. Desai, N. S. Kleiman, T. L. Sample, E. Elkins, G. W. Britz, Telerobotic stroke intervention: a novel solution to the care dissemination dilemma. *J. Neurosurg.* **132**, 971 (2019).

3. M. Goyal, G. R. Sutherland, S. Lama, P. Cimflova, N. Kashani, A. Mayank, M.-N. Psychogios, L. Spelle, V. Costalat, N. Sakai, J. M. Ospel, Neurointerventional robotics: challenges and opportunities. *Clin. Neuroradiol.* **30**, 203-208 (2020).

4. U.S. Food and Drug Administration (FDA), Center for Devices and Radiological Health, *Coronary, Peripheral, and Neurovascular Guidewires – Performance Tests and Recommended Labeling* (FDA-2018-D-1775, 2019); https://www.fda.gov/regulatory-information/search-fda-guidance-documents/coronary-peripheral-and-neurovascular-guidewires-performance-tests-and-recommended-labeling.

5. T. Krings, J. Finney, P. Niggemann, P. Reinacher, N. Lück, A. Drexler, J. Lovell, A. Meyer, R. Sehra, P. Schauerte, M. Reinges, F. J. Hans, A. Thron, Magnetic versus manual guidewire manipulation in neuroradiology: in vitro results. *Neuroradiology* **48**, 394-401 (2006).

6. M. R. Harrigan, J. P. Deveikis, *Handbook of Cerebrovascular Disease and Neurointerventional Technique*. (Humana Press, 2012).

7. C. E. Hoffler, A. M. Ilyas, Fluoroscopic radiation exposure: are we protecting ourselves adequately? *J. Bone Jt. Surg.* **97**, 721-725 (2015).

8. Y. Kim, G. A. Parada, S. Liu, X. Zhao, Ferromagnetic soft continuum robots. *Sci. Robot.* **4**, eaax7329 (2019).

9. S. A. Menaker, S. S. Shah, B. M. Snelling, S. Sur, R. M. Starke, E. C. Peterson, Current applications and future perspectives of robotics in cerebrovascular and endovascular neurosurgery. *J. Neurointerv. Surg.* **10**, 78-82 (2018).

10. J. Bonatti, G. Vetrovec, C. Riga, O. Wazni, P. Stadler, Robotic technology in cardiovascular medicine. *Nat. Rev. Cardiol.* **11**, 266-275 (2014).

11. J. Troccaz, G. Dagnino, G.-Z. Yang, Frontiers of medical robotics: from concept to systems to clinical translation. *Annu. Rev. Biomed. Eng.* **21**, 193-218 (2019).

12. J. Chakravartti, S. V. Rao, Robotic assisted percutaneous coronary intervention: hype or hope? *J. Am. Heart Assoc.* **8**, e012743 (2019).

13. V. M. Pereira, N. M. Cancelliere, P. Nicholson, I. Radovanovic, K. E. Drake, J.-M. Sungur, T. Krings, A. Turk, First-in-human, robotic-assisted neuroendovascular intervention. *J. Neurointerv. Surg.* **12**, 338-340 (2020).

14. G. W. Britz, J. Tomas, A. Lumsden, Feasibility of robotic-assisted neurovascular interventions: initial experience in flow model and porcine model. *Neurosurgery* **86**, 309-314 (2019).

15. K. C. Sajja, A. Sweid, F. Al Saiegh, N. Chalouhi, M. B. Avery, R. F. Schmidt, S. I. Tjoumakaris, M. R. Gooch, N. Herial, R. Abbas, H. Zarzour, V. Romo, R. Rosenwasser, P. Jabbour, Endovascular robotic: feasibility and proof of principle for diagnostic cerebral angiography and carotid artery stenting. *J. Neurointerv. Surg.* **12**, 345-349 (2020).

16. V. M. Pereira, P. Nicholson, N. M. Cancelliere, X. Y. E. Liu, R. Agid, I. Radovanovic, T. Krings, Feasibility of robot-assisted neuroendovascular procedures. *J. Neurosurg.*, 1-13 (2021).

17. S. Carniato, M. Mehra, R. M. King, A. K. Wakhloo, M. J. Gounis, Porcine brachial artery tortuosity for in vivo evaluation of neuroendovascular devices. *Am. J. Neuroradiol.* **34**, E36-E38 (2013).

18. S. Chiaverini, G. Oriolo, I. D. Walker, Kinematically redundant manipulators in *Springer Handbook of Robotics,* (Springer Nature, 2008), pp. 245-268.

19. Y. Kim, H. Yuk, R. Zhao, S. A. Chester, X. Zhao, Printing ferromagnetic domains for untethered fast-transforming soft materials. *Nature* **558**, 274-279 (2018).

20. R. Zhao, Y. Kim, S. A. Chester, P. Sharma, X. Zhao, Mechanics of hard-magnetic soft materials. *J. Mech. Phys. Solids* **124**, 244-263 (2019).

21. L. Wang, Y. Kim, C. F. Guo, X. Zhao, Hard-magnetic elastica. *J. Mech. Phys. Solids* **142**, 104045 (2020).

22. ASAHI Neurovascular Guide Wire Instruction for Use (Asahi Intecc, 2012); https://asahi-inteccusa-medical.com/product/asahi-chikai/.

23. Z. Zhuang, B. Bradtmiller, Head-and-face anthropometric survey of U.S. respirator users. *J. Occup. Environ. Hyg.* **2**, 567-576 (2005).

24. D. J. Craik, *Magnetism: principles and applications*. (Wiley, 1995).

25. J. S. Agashe, D. P. Arnold, A study of scaling and geometry effects on the forces between cuboidal and cylindrical magnets using analytical force solutions. *J. Phys. D: Appl. Phys.* **41**, 105001 (2008).

26. C. D. Natali, M. Beccani, P. Valdastri, Real-time pose detection for magnetic medical devices. *IEEE Trans. Magn.* **49**, 3524-3527 (2013).

27. K. M. Lynch, F. C. Park, *Modern Robotics: Mechanics, Planning, and Control*. (Cambridge University Press, 2017).

28. S. Torikoshi, Y. Akiyama, A concealed intracranial aneurysm detected after recanalization of an occluded vessel: a case report and literature review. *Interv. Neurol.* **4**, 90-95 (2015).

29. T. Krings, D. M. Mandell, T.-R. Kiehl, S. Geibprasert, M. Tymianski, H. Alvarez, K. G. terBrugge, F.-J. Hans, Intracranial aneurysms: from vessel wall pathology to therapeutic approach. *Nat. Rev. Neurol.* **7**, 547-559 (2011).

30. R. M. Starke, A. Turk, D. Ding, R. W. Crowley, K. C. Liu, N. Chalouhi, D. M. Hasan, A. S. Dumont, P. Jabbour, C. R. Durst, R. D. Turner, Technology developments in endovascular treatment of intracranial aneurysms. *J. Neurointerv. Surg.* **8**, 135-144 (2016).

31. ASIST™ Proprietary Thrombus Simulant (Vascular Simulations, 2020); https://vascularsimulations.com/simulation-accessories/#thrombus.

32. F. Arikan, T. Martínez-Valverde, Á. Sánchez-Guerrero, M. Campos, M. Esteves, D. Gandara, R. Torné, L. Castro, A. Dalmau, J. Tibau, J. Sahuquillo, Malignant infarction of the middle cerebral artery in a porcine model. A pilot study. *PLOS ONE* **12**, e0172637 (2017).

33. A. von Hessling, T. Reyes del Castillo, G. Karwacki, J. E. Roos, The Columbus steerable guidewire in neurointerventions: early clinical experience and applications. *J. Neurointerv. Surg.* **0**, 1-6 (2021).

34. A. P. Mamunes, F. Campisano, J. Martin, B. Scaglioni, E. Mazomenos, P. Valdastri, K. L. Obstein, Magnetic flexible endoscope for colonoscopy: an initial learning curve analysis. *Endosc. Int. Open* **09**, E171-E180 (2021).

35. S. Jeon, A. K. Hoshiar, K. Kim, S. Lee, E. Kim, S. Lee, J.-Y. Kim, B. J. Nelson, H.-J. Cha, B.-J. Yi, H. Choi, A magnetically controlled soft microrobot steering a guidewire in a three-dimensional phantom vascular network. *Soft Robot.* **6**, 54-68 (2018).

36. A. Azizi, C. C. Tremblay, K. Gagné, S. Martel, Using the fringe field of a clinical MRI scanner enables robotic navigation of tethered instruments in deeper vascular regions. *Sci. Robot.* **4**, eaax7342 (2019).

37. S. Jeong, Y. Chitalia, J. P. Desai, Design, modeling, and control of a coaxially aligned steerable (COAST) guidewire robot. *IEEE Robot. Autom. Lett.* **5**, 4947-4954 (2020).

38. M. Schiemann, R. Killmann, M. Kleen, N. Abolmaali, J. Finney, T. J. Vogl, Vascular guide wire navigation with a magnetic guidance system: experimental results in a phantom. *Radiology* **232**, 475-481 (2004).

39. K. Tsuchida, H. M. García-García, W. J. van der Giessen, E. P. McFadden, M. van der Ent, G. Sianos, H. Meulenbrug, A. T. L. Ong, P. W. Serruys, Guidewire navigation in coronary artery stenoses using a novel magnetic navigation system: first clinical experience. *Catheter. Cardiovasc. Interv.* **67**, 356-363 (2006).

40. J. J. Tharayil, S. M. Goetz, J. M. Bernabei, A. V. Peterchev, Field distribution of transcranial static magnetic stimulation in realistic human head model. *Neuromodulation* **21**, 340-347 (2018).

41. H. Tillander, Magnetic guidance of a catheter with articulated steel tip. *Acta Radiol.* **35**, 62-64 (1951).

42. J. F. Alksne, Magnetically controlled intravascular catheter. *Surgery* **64**, 339-345 (1968).

43. J. Molcho, H. Z. Karny, E. H. Frei, H. M. Askenasy, Selective cerebral catheterization. *IEEE Trans. Biomed. Eng.* . **17**, 134-140 (1970).

44. H. L. Cares, J. R. Hale, D. B. Montgomery, H. A. Richter, W. H. Sweet, Laboratory experience with a magnetically guided intravascular catheter system. *J. Neurosurg.* **38**, 145-154 (1973).

45. S. K. Hilal, W. J. Michelsen, J. Driller, E. Leonard, Magnetically guided devices for vascular exploration and treatment. *Radiology* **113**, 529-540 (1974).

46. M. S. Grady, M. A. Howard, R. G. Dacey, W. Blume, M. Lawson, P. Werp, R. C. Ritter, Experimental study of the magnetic stereotaxis system for catheter manipulation within the brain. *J. Neurosurg.* **93**, 282-288 (2000).

47. S. Ramcharitar, M. S. Patterson, R. J. van Geuns, C. van Meighem, P. W. Serruys, Technology insight: magnetic navigation in coronary interventions. *Nat. Clin. Pract.* **5**, 148-156 (2008).

48. U.S. Food and Drug Administration (FDA), *Class 2 Medical Device Recalls: Cronus Endovascular Guidewires* (510(K) Number: K021363, FDA, 2004); https://www.accessdata.fda.gov/scripts/cdrh/cfdocs/cfRES/res.cfm?start_search=1&knumber=K021363.

49. A. W. Mahoney, J. J. Abbott, Five-degree-of-freedom manipulation of an untethered magnetic device in fluid using a single permanent magnet with application in stomach capsule endoscopy. *Int. J. Rob. Res.* **35**, 129-147 (2016).

50. L. B. Kratchman, T. L. Bruns, J. J. Abbott, R. J. Webster, Guiding elastic rods with a robot-manipulated magnet for medical applications. *IEEE Trans. Robot.* **33**, 227-233 (2017).

51. A. Z. Taddese, P. R. Slawinski, M. Pirotta, E. De Momi, K. L. Obstein, P. Valdastri, Enhanced real-time pose estimation for closed-loop robotic manipulation of magnetically actuated capsule endoscopes. *Int. J. Rob. Res.* **37**, 890-911 (2018).

52. G. Pittiglio, L. Barducci, J. W. Martin, J. C. Norton, C. A. Avizzano, K. L. Obstein, P. Valdastri, Magnetic levitation for soft-tethered capsule colonoscopy actuated with a single permanent magnet: a dynamic control approach. *IEEE Robot. Autom. Lett.* **4**, 1224-1231 (2019).

53. J. C. Norton, P. R. Slawinski, H. S. Lay, J. W. Martin, B. F. Cox, G. Cummins, M. P. Y. Desmulliez, R. E. Clutton, K. L. Obstein, S. Cochran, P. Valdastri, Intelligent magnetic manipulation for gastrointestinal ultrasound. *Sci. Robot.* **4**, eaav7725 (2019).

54. J. W. Martin, B. Scaglioni, J. C. Norton, V. Subramanian, A. Arezzo, K. L. Obstein, P. Valdastri, Enabling the future of colonoscopy with intelligent and autonomous magnetic manipulation. *Nat. Mach. Intell.* **2**, 595-606 (2020).

55. C. A. Bellemare, T. G. Poder, Effectiveness of biplane angiography compared to monoplane angiography for vascular neuro-interventions: a systematic review of the literature. *Clin. Radiol.* **72**, 6121-6125 (2017).

56. B. Friedrich, C. Maegerlein, D. Lobsien, S. Mönch, M. Berndt, D. Hedderich, S. Wunderlich, D. Michalski, M. Lehm, T. Boeckh-Behrens, C. Zimmer, K. Kreiser, Endovascular stroke treatment on single-plane vs. bi-plane angiography suites. *Clin. Neuroradiol.* **29**, 303-309 (2019).

57. A. Guenego, P. J. Mosimann, M. Wintermark, J. J. Heit, K. Zuber, T. Dobrocky, J. A. Lotterie, P. Nicholson, D. G. Marcellus, J. M. Olivot, N. Gonzalez, R. Blanc, V. M. Pereira, J. Gralla, J. Kaesmacher, R. Fahed, M. Piotin, C. Cognard, E. Piechowiak, P. Mordasini, F. Zibold, C. Ducroux, F. Bonneville, J. Darcourt, I. Vukasinovic, A. C. Januel, S. Monfraix, C. Michelozzi, P. Tall, M. Mazighi, J.-P. Desilles, G. Ciccio, S. Smajda, H. Redjem, B. Maier, B. W. Martin, E. Guenego, F. Carbillet, Safety and effectiveness of neuro-thrombectomy on single compared to biplane angiography systems. *Sci. Rep.* **10**, 4470 (2020).

58. T. M. Patel, S. C. Shah, S. B. Pancholy, Long distance tele-robotic-assisted percutaneous coronary intervention: a report of first-in-human experience. *EClinicalMedicine* **14**, 53-58 (2019).

59. X. Jiang, H. Shokri-Ghadikolaei, G. Fodor, E. Modiano, Z. Pang, M. Zorzi, C. Fischione, Low-latency networking: where latency lurks and how to tame it. *Proc. IEEE* **107**, 280-306 (2019).

60. J. Zheng, Y. Wang, J. Zhang, W. Guo, X. Yang, L. Luo, W. Jiao, X. Hu, Z. Yu, C. Wang, L. Zhu, Z. Yang, M. Zhang, F. Xie, Y. Jia, B. Li, Z. Li, Q. Dong, H. Niu, 5G ultra-remote robot-assisted laparoscopic surgery in China. *Surg. Endosc.* **34**, 5172-5180 (2020).

61. M. Bechstein, J.-H. Buhk, A. M. Frölich, G. Broocks, U. Hanning, M. Erler, M. Andelkovic, D. Debeljak, J. Fiehler, E. Goebell, Training and supervision of thrombectomy by remote live streaming support (RESS). *Clin. Neuroradiol.* **31**, 181-187 (2019).

62. M. Bechstein, S. Elsheikh, F. Wodarg, C. A. Taschner, U. Hanning, J.-H. Buhk, R. McDonough, E. Goebell, J. Fiehler, M. Bester, Republished: Interhospital teleproctoring of endovascular intracranial aneurysm treatment using a dedicated live-streaming technology: first experiences during the COVID-19 pandemic. *J. Neurointerv. Surg.* **0**, 1-3 (2020).

63. H. Gibo, C. Lenkey, A. L. Rhoton, Microsurgical anatomy of the supraclinoid portion of the internal carotid artery. *J. Neurosurg.* **55**, 560-574 (1981).

Acknowledgments

The authors thank Sang Uk Lee and Heather Bowman (Massachusetts Institute of Technology) for helpful discussion and feedback on the manuscript. The authors also thank Alexandru Patriciu and Sean Kyne (Philips Research) for participating usability testing and learning curve assessment and providing feedback and Molly Flexman and Atul Gupta (Philips Research) as well for insightful discussion and constructive feedback on the developed system. The authors also thank Chanthakham Thammavong (Massachusetts General Hospital) for help with fluoroscopic imaging and Robert King, Erin Langan, Chris Brooks, and Matthew Gounis (University of Massachusetts Medical School) for help with animal testing.

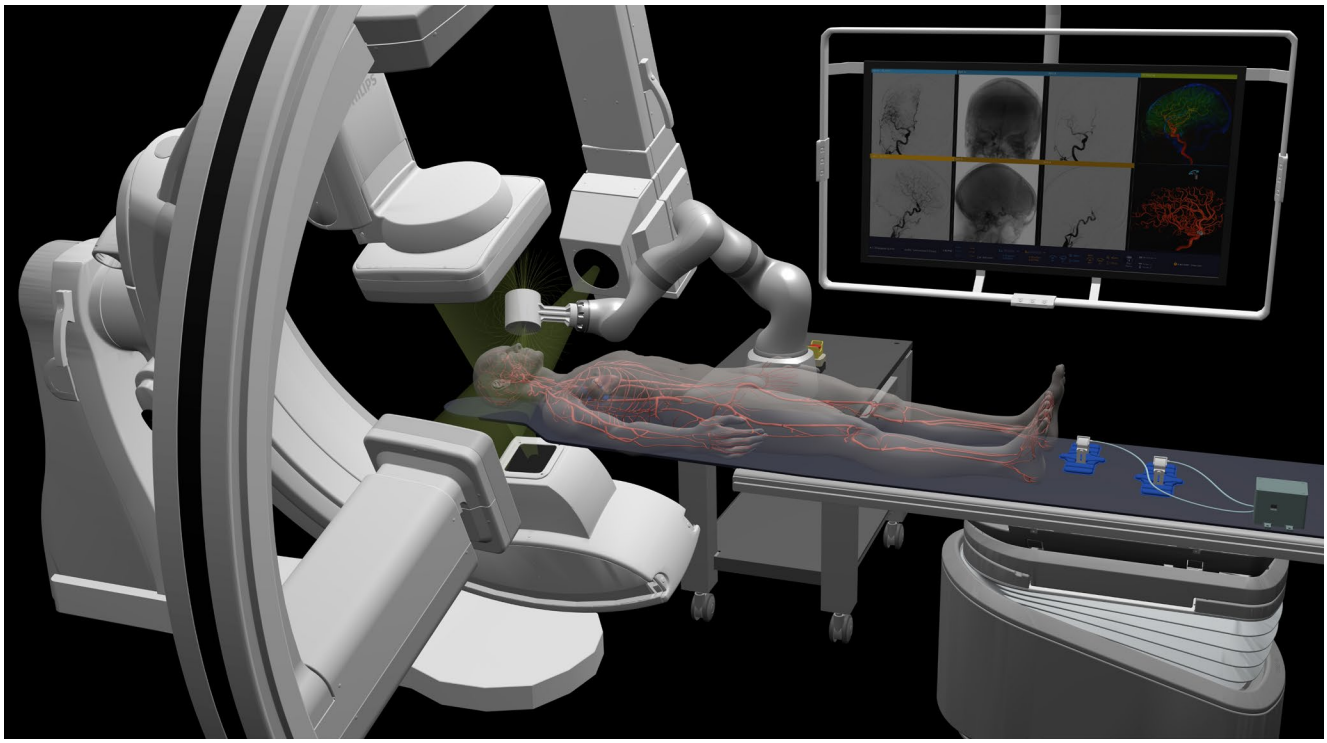
Funding: This work was supported by the National Science Foundation (EFRI-1935291) and National Institutes of Health (1R01HL153857-01) and funded in part by Philips Research North America through MIT-Philips research alliance. Y.K. acknowledges the financial support through a scholarship from ILJU Academy and Culture Foundation and MIT School of Engineering MathWorks Fellowship.

Author contributions: Y.K. and X.Z. conceived and designed the study. Y.K. developed the magnetic soft continuum guidewire and the telerobotic manipulation platform and its control interface. Y.K. and E.G. developed the guidewire/catheter advancing unit and its control interface. Y.K., J.C., P.H., and M.B. conducted the in vitro experiments and analyzed the results. P.H. and A.B.P. provided guidance and feedback on the demonstrated endovascular interventional procedures. Y.K., J.C., M.B., and R.W.R., conducted the in vivo animal study and analyzed the results. Y.K., J.C., P.H., M.B., R.W.R., J.E.V., A.D., and A.B.P. conducted the usability testing for learning curve assessment and provided feedback. P.H. evaluated the performance of the telerobotically controlled magnetic guidewire in comparison with the manually controlled passive guidewire and assessed the operator's task load. Y.K. and X.Z. wrote the manuscript with input from all authors. X.Z. supervised the study.

Competing interests: The authors declare that they have no competing financial interests. Y.K. and X.Z. are listed as inventors of a patent on the presented telerobotic neurointerventional system and the magnetic soft continuum guidewire. The other authors declare that they have no competing financial interests.

Data and materials availability: All data are provided in the manuscript and the Supplementary Materials (data S1).

Main Figures



Movie 1. Overview of telerobotic stroke intervention based on magnetic manipulation.

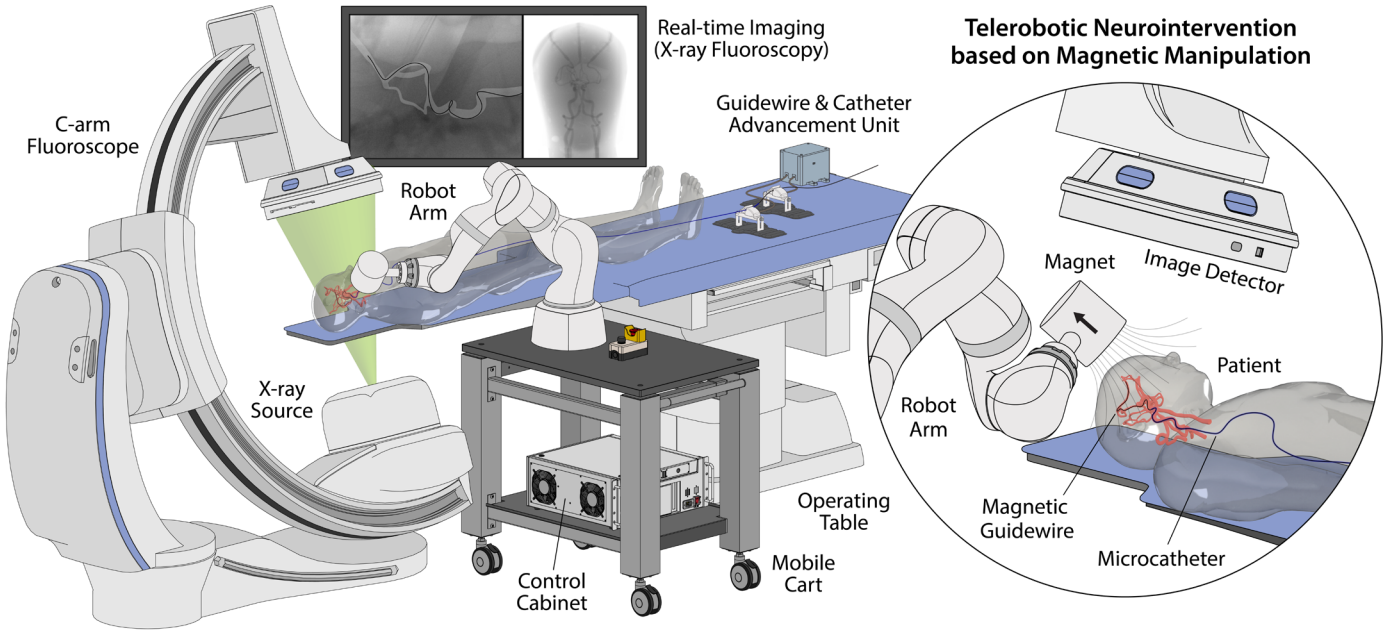


Figure 1. Overview of the telerobotic neurointerventional platform based on magnetic manipulation. The system features a lightweight, compact robot arm with an actuating magnet attached to its end-effector to remotely control a magnetically steerable guidewire through spatial positioning of the magnet around the patient's head. Mounted on a mobile platform beside the operating table, the robot arm is teleoperated from a remote-control console to steer the magnetic guidewire under real-time fluoroscopic imaging. The system further integrates a guidewire/microcatheter advancing unit based on a pair of motorized linear drives that can advance or retract the guidewire and a microcatheter upon remote control.

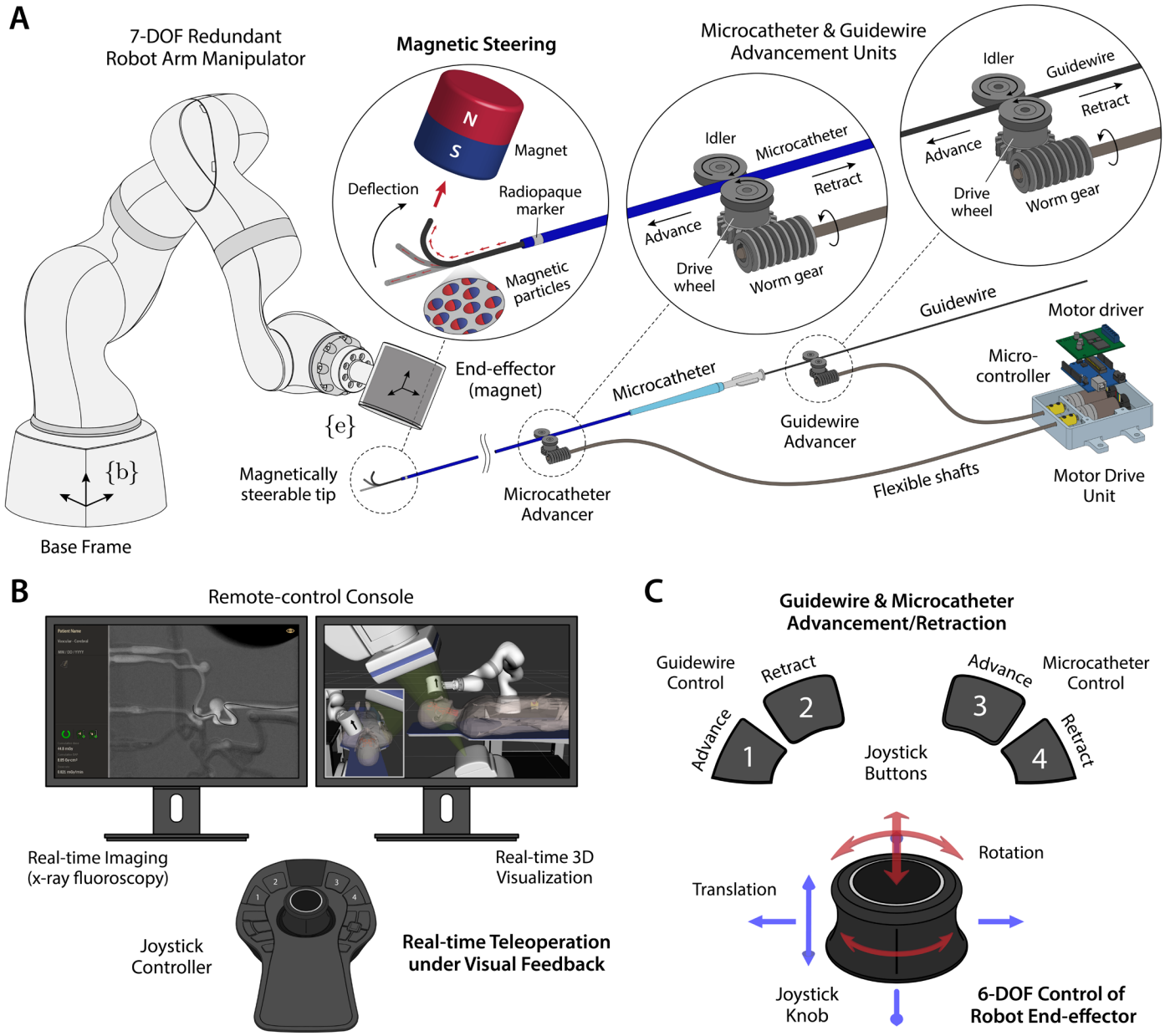


Figure 2. Description of the telerobotic neurointerventional system. (**A**) The robot arm has 7 degrees of freedom (DOF) with kinematic redundancy for flexible manipulation and safer operation in cluttered environments. The guidewire has a magnetically responsive tip that contains magnetic particles, and hence can be steered by the actuating magnet at the robot arm's end-effector. The guidewire is compatible with a standard microcatheter which travels over the guidewire along the navigated path. The guidewire and the microcatheter can be advanced/retracted by a pair of advancing units, each of which uses a worm drive to convert the rotary motion of the DC motor at the base to a linear motion. (**B**) The system is teleoperated from the remote-control console under feedback from real-time imaging of the guidewire/microcatheter in the blood vessels and virtual visualization of the robot arm. The magnetic guidewire is naturally visible under x-ray due to the embedded magnetic particles, and the position of the microcatheter can be identified by the radiopaque marker at the distal end. The robot arm is visualized in a virtual environment that replicates the real world on the control workstation to allow the operator to avoid collisions with surrounding objects while teleoperating the robot arm. (**C**) Spatial positioning of the magnet is achieved via 6-DOF position control of the robot arm's end-effector with a joystick controller, and advancement/retraction of the guidewire and the microcatheter can be controlled either independently or simultaneously with the joystick buttons.

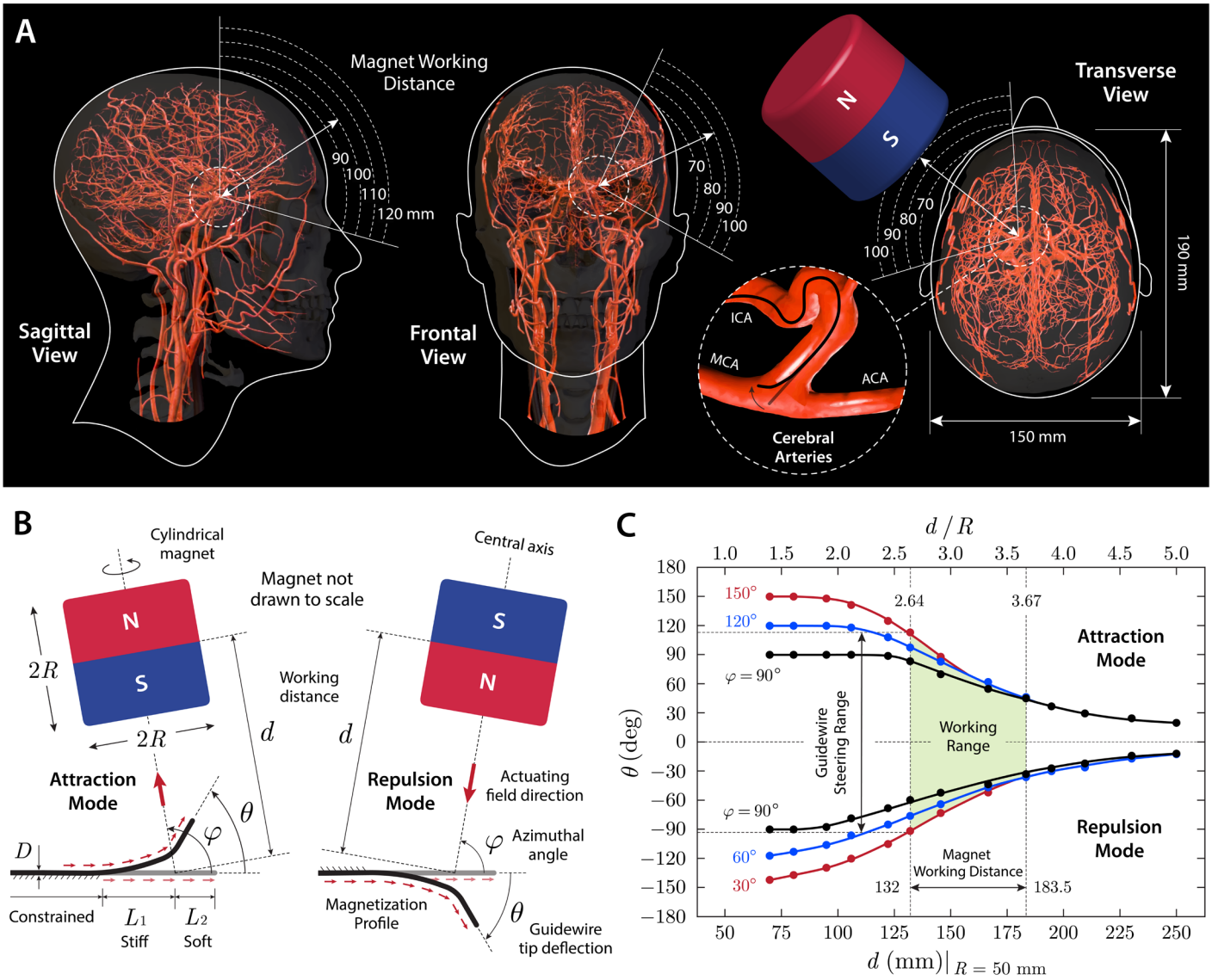


Figure 3. Design considerations for magnetic steering with a single magnet. (**A**) Working distance and area for a cylindrical magnet (diameter and thickness of 100 mm) around the head considering the average head size (23) and anatomical location and orientation of intracranial arteries illustrated on the sagittal, frontal, and transverse planes. When viewed from the sagittal plane, the distance from the surface of the magnet to the Circle of Willis in the middle of the head is estimated to be around 100 mm. When viewed from the frontal and transverse planes, the distance from the surface of the magnet to left ICA bifurcation is estimated to be 80~90 mm. ICA: internal carotid artery; MCA/ACA: middle/anterior cerebral artery. (**B**) Attraction and repulsion modes for steering control of the magnetic guidewire with a single magnet of cylindrical shape (diameter and thickness of $2R$). The magnet working distance, denoted d, is defined as the distance from the center of the magnet to the base of the guidewire's softer tip. The angular position of the magnet relative to the guidewire's reference state is defined by the azimuthal angle φ, and the tip deflection angle is denoted θ. D indicates the outer diameter of the guidewire, and L_1 and L_2 denote the stiff and soft segments in the unconstrained (free to bend) portion of the guidewire's steerable tip, respectively. (**C**) Characterization of the magnetic guidewire's behavior under magnetic manipulation with a single magnet. The tip deflection angle θ was measured while varying the working distance and the angular position of the actuating magnet in the attraction and repulsion modes (guidewire dimension: $D = 400$ μm, $L_1 = 6$ mm, $L_2 = 4$ mm).

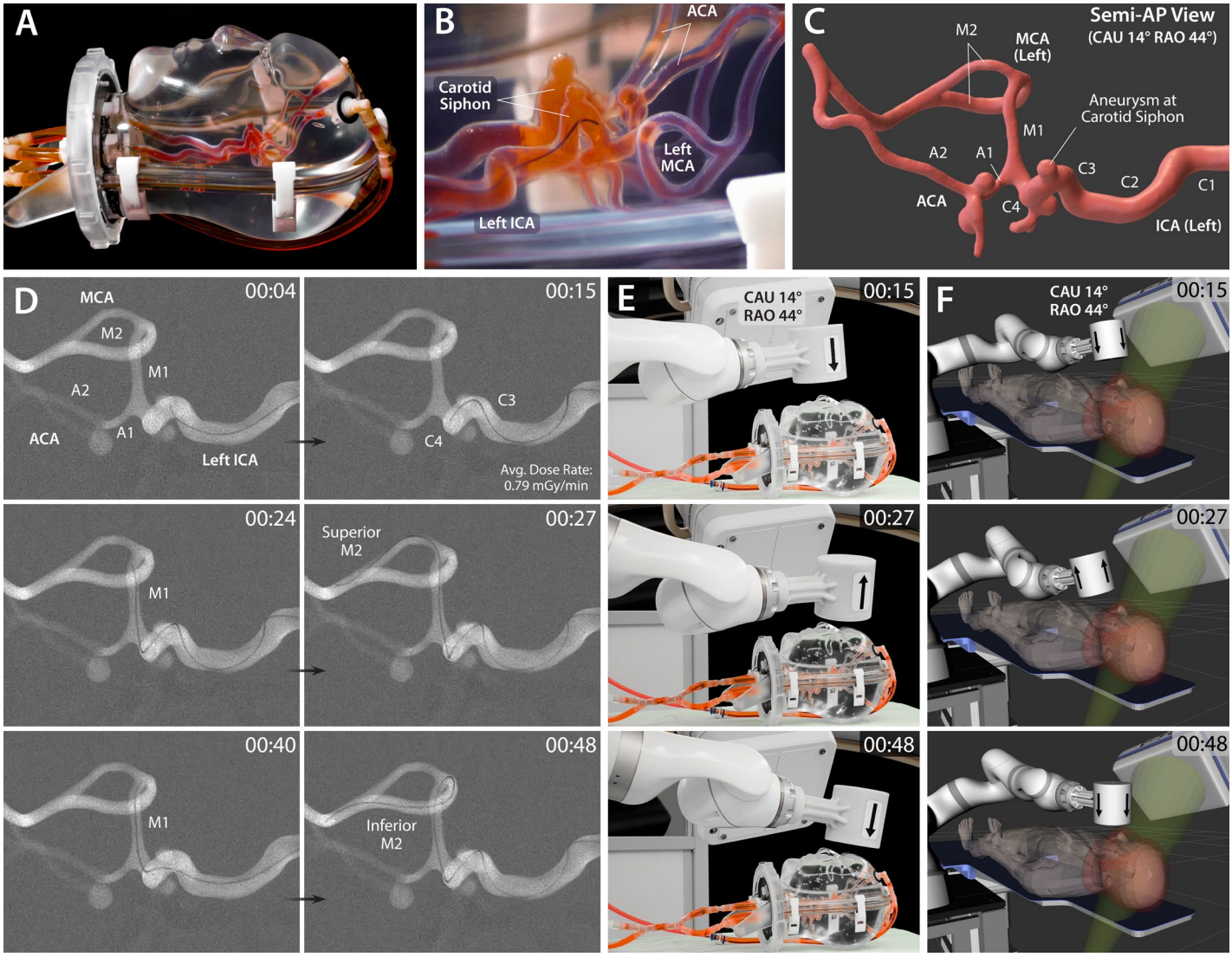


Figure 4. In vitro demonstration of magnetic steering and navigation in intracranial arteries under real-time x-ray fluoroscopy. (**A**) Realistic human head phantom with replicated intracranial arteries based on silicone vessels. (**B**) Lateral view of the magnetic guidewire navigating in the left ICA with its distal tip being directed toward the descending portion of the carotid siphon under repulsive steering to avoid contact with the aneurysm at the apex of the carotid siphon. (**C**) 3D model of the target vasculature viewed from a semi-anteroposterior (AP) projection which shows all the important anatomical landmarks including the carotid siphon with an aneurysm, the ICA bifurcation (A1-M1 junction), and the MCA bifurcation at the same time. (**D**) Fluoroscopic images of the magnetic guidewire navigating from the left ICA to MCA under telerobotically controlled magnetic steering to reach the superior and inferior M2 segments selectively in sequence. As part of the preprocedural step, digital subtraction angiography was performed to visualize the target vasculature as a roadmap for guidewire steering and navigation. ICA: internal carotid artery; MCA/ACA: middle/anterior cerebral artery. (**E**) Actual view and (**F**) virtual visualization of the robot arm with an actuating magnet, the C-arm providing the semi-AP projection for the target vasculature in caudal angulation of 14° (CAU 14°) and right anterior oblique rotation of 44° (RAO 44°), the human head phantom (or equivalently the virtual human patient) on the operating table. The arrow on the actuating magnet indicating the magnet's polarity identifies which steering mode is being used. A live fluoroscopy video is available in **movie S2**, which also shows the robot motion under real-time teleoperation in both the physical and virtual environments. The average time ($\pm$ standard deviation) it took for the demonstrated navigational task was 45.0 $\pm$ 4.0 s ($n = 5$).

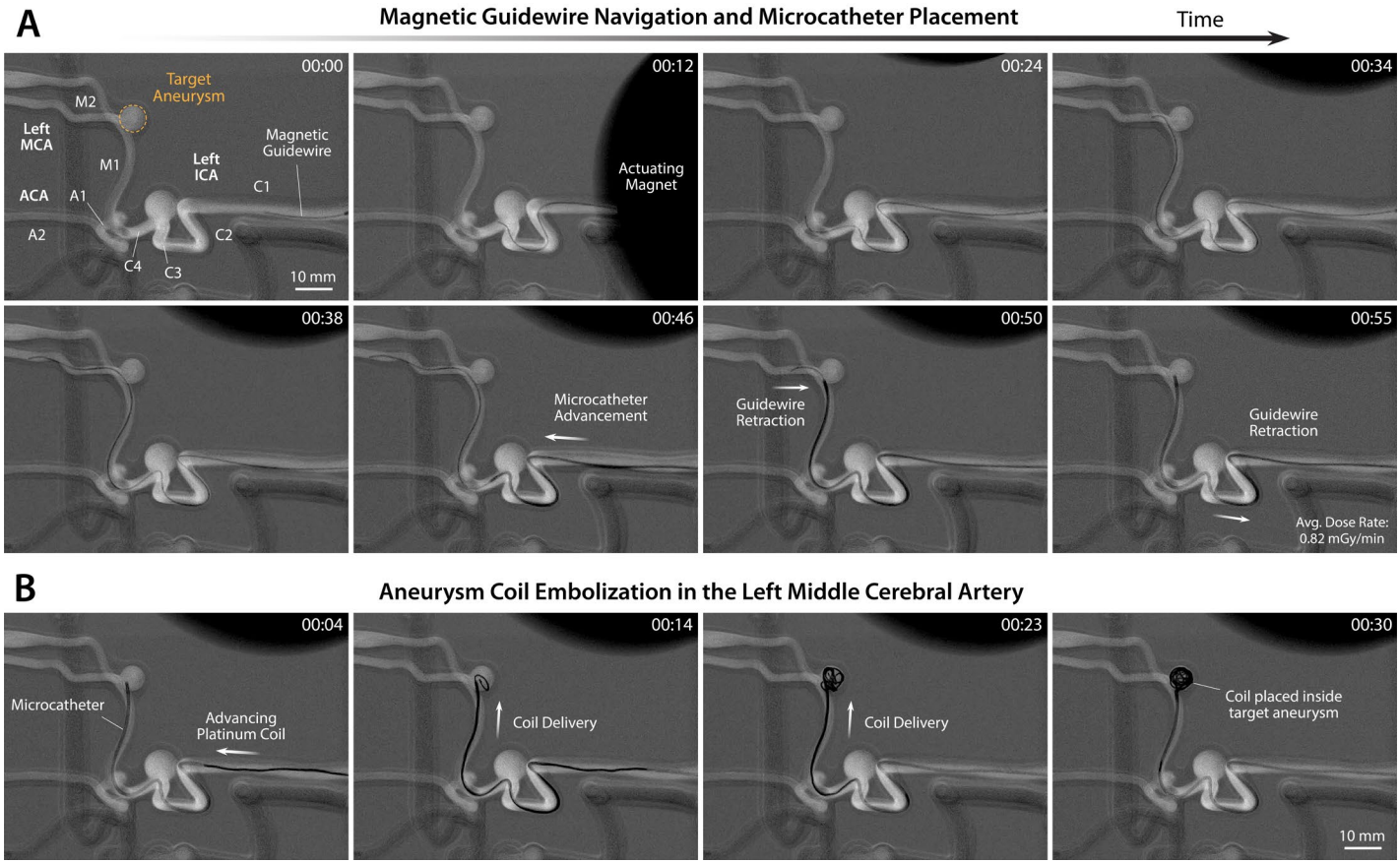


Figure 5. Demonstration of telerobotically assisted aneurysm coil embolization in the middle cerebral artery. (**A**) Magnetic steering and guidewire navigation up to the target aneurysm in the left middle cerebral artery (MCA) (00:00~00:38) and microcatheter placement in the target aneurysm sac while retracting the guidewire (00:46~00:55) through real-time teleoperation of the system under x-ray fluoroscopy. (**B**) Endovascular coiling of the targeted aneurysm by delivering embolization coils into the aneurysm sac through the placed microcatheter under joystick teleoperation of the advancing unit. Demonstration of the entire procedure from guidewire navigation and steering control to aneurysm coiling is presented in **movie S3**. The average time ($\pm$ standard deviation) it took for the demonstrated guidewire navigation and microcatheter placement in the targeted aneurysm in (**A**) was 51.7 $\pm$ 3.5 s (n = 3) and the coiling of the aneurysm in (**B**) was 32.3 $\pm$ 2.5 s (n = 3).

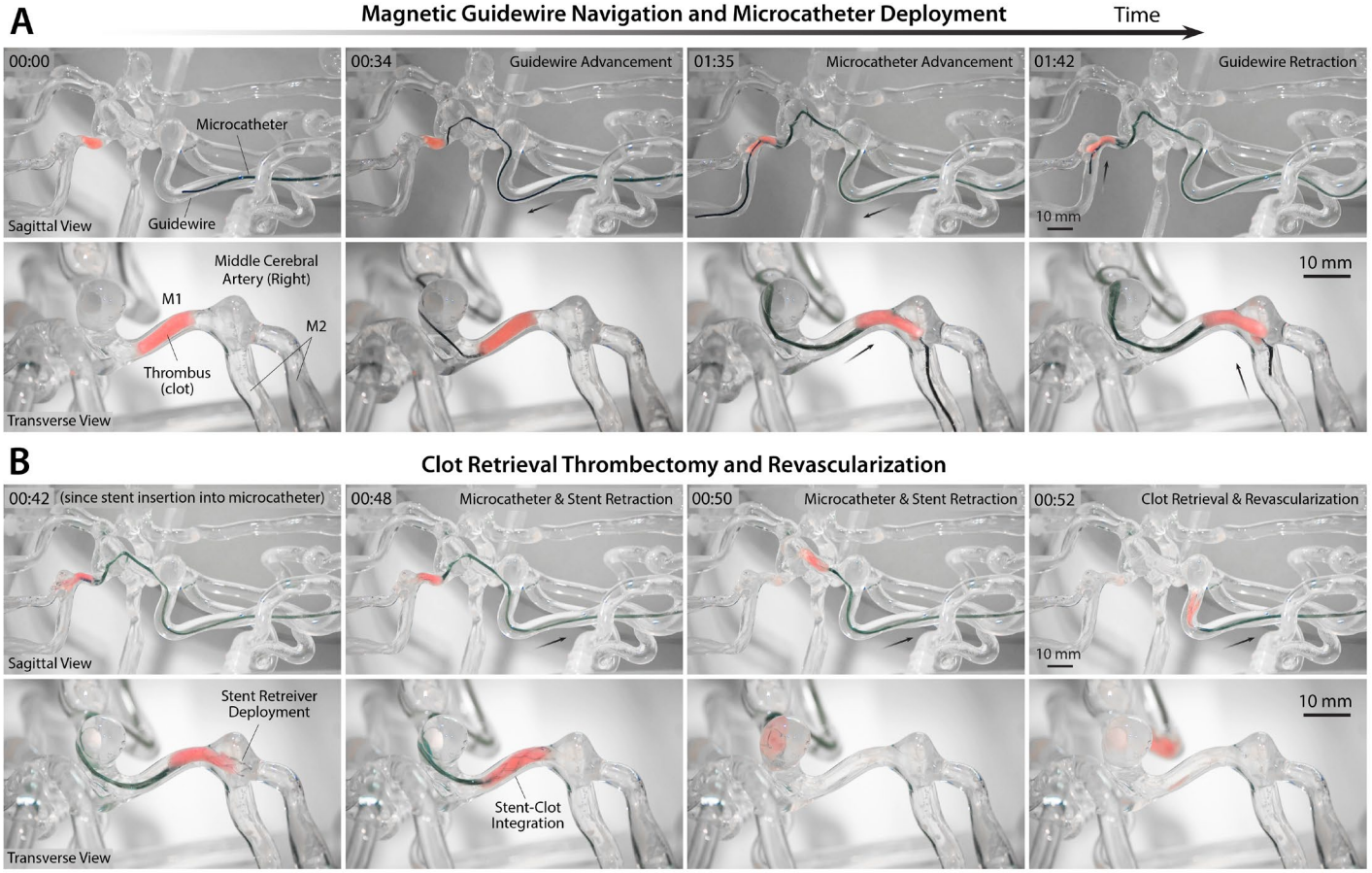


Figure 6. Demonstration of telerobotically assisted clot retrieval thrombectomy and revascularization in the cerebral vasculature. (**A**) Navigation up to the simulated clot in the M1 segment of the right middle cerebral artery (MCA) with the telerobotically controlled magnetic guidewire (00:00~00:34) and microcatheter placement across the thrombus with the aid of magnetic steering at the MCA bifurcation (01:35~01:42) under real-time optical imaging to show the clot during the interventional process. (**B**) Deployment of a stent retriever across the thrombus (00:42~00:48) and retrieval of the clot upon withdrawal of the stent retriever and the microcatheter for revascularization of the occluded site (00:50~00:52). Demonstration of the entire navigation, steering control, and stent deploying procedures is available in **movie S5**. Telerobotically assisted clot retrieval procedure performed under real-time x-ray fluoroscopy is also presented in **fig. S11**. The average time ($\pm$ standard deviation) it took for the demonstrated guidewire navigation and microcatheter placement in the occluded site in (**A**) was 108.0 $\pm$ 14.0 s ($n = 3$) and the clot retrieval using the stent retriever in (**B**) was 46.7 $\pm$ 5.0 s ($n = 3$).

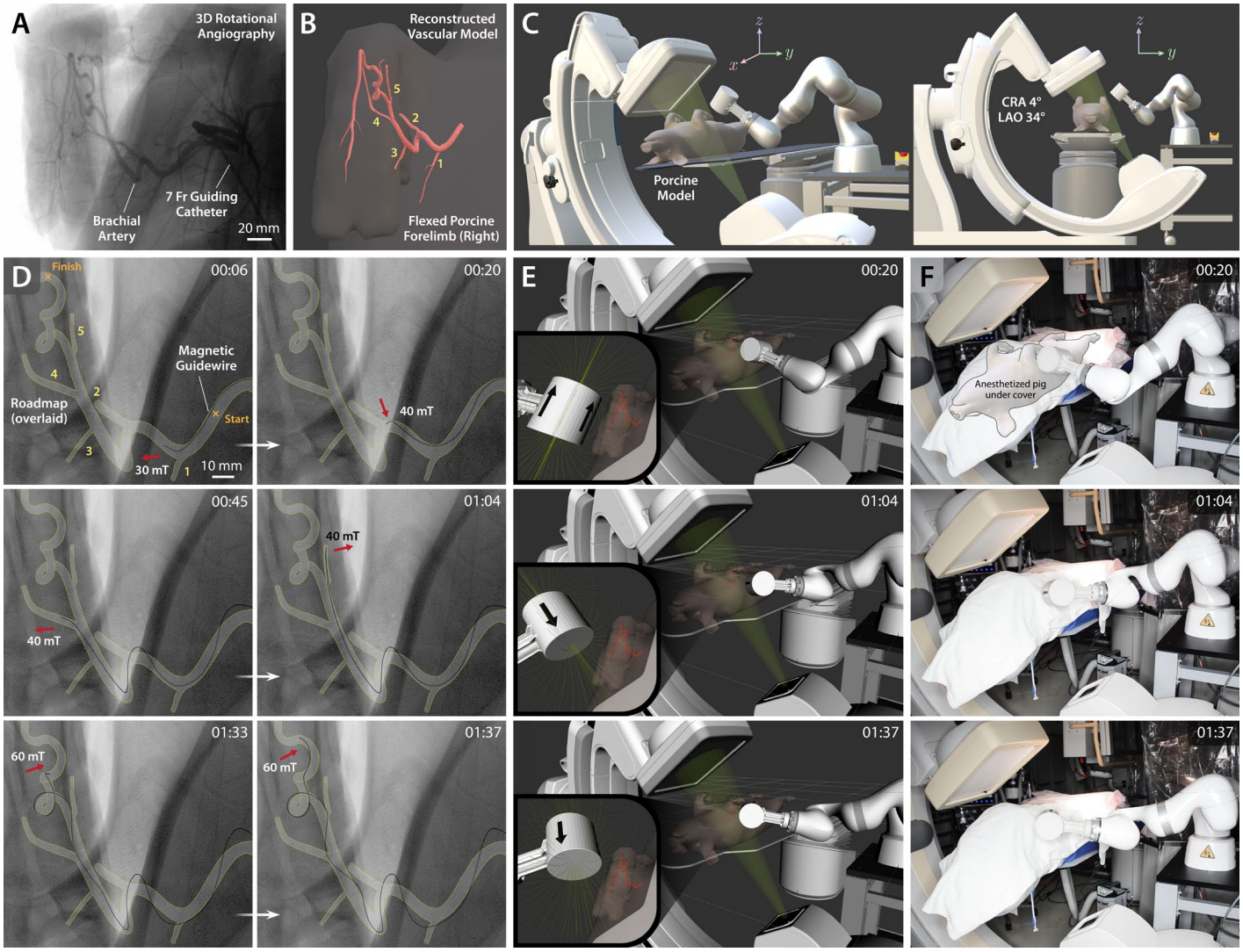


Figure 7. In vivo demonstration of telerobotically controlled magnetic navigation in porcine brachial artery. (**A**) 3D rotational angiography of the porcine brachial artery with accentuated tortuosity in the maximally flexed forelimb position to replicate the tortuosity of the human carotid siphon. (**B**) Reconstructed 3D model of the target vasculature viewed from a semi-anteroposterior (AP) projection with all the side branches along the path clearly shown and numbered. (**C**) Graphical representation of the experimental setup with the C-arm configuration for the chosen semi-AP projection based on cranial angulation of 4° (CRA 4°) and left anterior oblique rotation of 34° (LAO 34°). (**D**) Fluoroscopic images of the magnetic guidewire navigating in the target vasculature under telerobotically controlled magnetic steering avoiding entering undesired branches (1 and 2) at the acute-angled corners (00:06~00:20). The guidewire was steered to selectively reach the side branches (4 and 5) present on the path (00:45~01:04) and then reach the goal after negotiating the tortuous region with 360-degree and 90-degree turns (01:33~01:37). (**E**) Real-time visualization of the robot arm in a virtual environment simulating the physical testing setup including the C-arm and the anesthetized pig on the operating table. The target vasculature and the magnetic field lines around the actuating magnet are also visualized in real time to enable preprocedural planning of the robot arm's motion for spatial positioning of the magnet relative to the target vasculature. (**F**) Actual view of the robot arm positioning the magnet based on the prescribed magnet position and orientation for the steering and navigational task upon the operator's command from the remote-control console. Out of respect for the animal and to comply with the Institutional Animal Care and Use Committee (IACUC) policy on photography of research animals, the pig was covered during the video recording. Demonstration of the entire navigation and steering control procedures is available in **movie S6**. The average time ($\pm$ standard deviation) it took for the demonstrated task was 124.6 $\pm$ 19.7 s ($n = 5$).

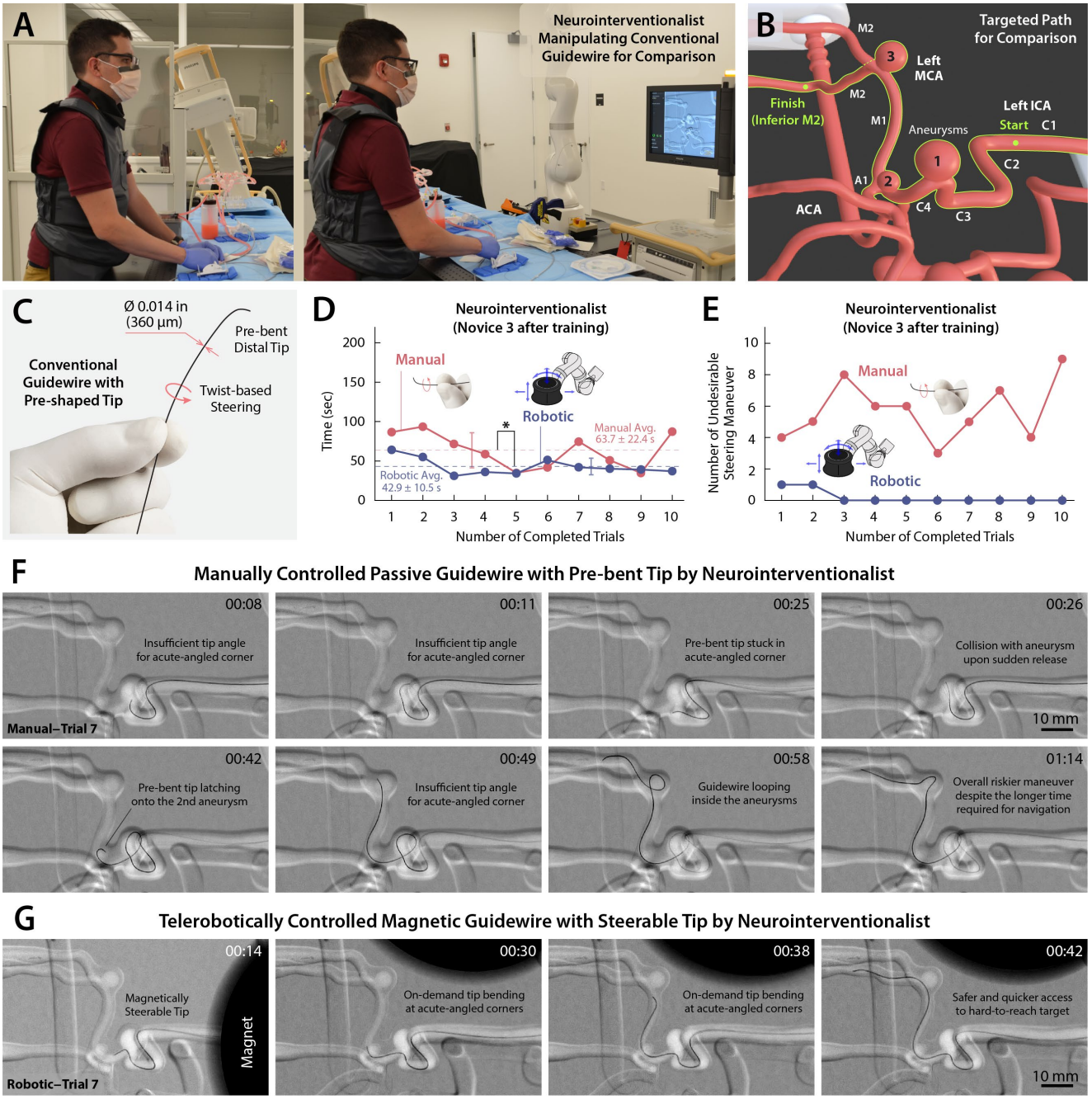


Figure 8. Evaluation of the steering and navigational performance of the telerobotically controlled magnetic guidewire in comparison with the conventional neurovascular guidewire based on manual manipulation by a neurointerventionalist. (**A**) Neurointerventionalist manually manipulating a conventional neurovascular guidewire with pre-bent distal tip for twist-based steering under real-time x-ray fluoroscopy. (**B**) Defined navigational task for the performance comparison from the left internal carotid artery (ICA) to the inferior M2 segment of the middle cerebral artery (MCA). (**C**) Conventional neurovascular guidewire (Synchro 2, Stryker) with an outer diameter of 0.014 inches (360 µm) and pre-bent (shapeable) distal tip. (**D**) Comparison of the procedural time (average ± standard deviation) for the trained neurointerventionalist to complete the defined navigational task using the manually controlled passive guidewire and the telerobotically controlled magnetic guidewire over 10 consecutive trials ($n = 10$) for each experiment. Error bars with whiskers indicate the standard deviation of the measured time, and statistically significant differences are indicated with asterisks ($^*P < 0.05$). The interventionalist has +4 years of training and experiences in endovascular neurointervention based on conventional guidewire manipulation and was trained with the telerobotic manipulation system for less than 1 hour (see Novice 3 in **fig. S16**). (**E**) The number of incidents with undesirable guidewire behavior such as the distal tip colliding with or looping inside aneurysms or falling into undesired branches during the given navigational task. (**F**) The pre-bent tip of the conventional guidewire tended to undergo unpredictable and undesirable motion while making frequent contact with the aneurysms present along the path due to the limited steering capability based on twisting maneuver. (**G**) The magnetic guidewire demonstrated smooth navigation in the narrow and tortuous pathways without any unintended distal tip movement or contact with the aneurysms along the navigated path due to its active steering. Videos for comparison of the steering and navigational performance are available in **movies S7** and **S8**.

Science Robotics
AAAS

Supplementary Materials for

Telerobotic neurovascular intervention with magnetic manipulation

Yoonho Kim, Emily Genevriere, Pablo Harker, Jaehun Choe, Marcin Balicki,
Robert W. Regenhardt, Justin E. Vranic, Adam A. Dmytriw, Aman B. Patel, Xuanhe Zhao*

* Corresponding author. Email: zhaox@mit.edu

This PDF file includes:

List of Acronyms and Abbreviations
Supplementary Text
Figure S1. Mechanical characterization of the magnetic polymer composites.
Figure S2. Anatomy and nomenclature of intracranial arteries.
Figure S3. Magnetic fields around a cylindrical magnet.
Figure S4. Spatial gradients of the magnetic fields around a cylindrical magnet.
Figure S5. Transition between the attraction and repulsion modes.
Figure S6. Definition and characterization of the oblique repulsion mode.
Figure S7. Benchtop demonstration of telerobotically controlled magnetic steering and navigation in cerebral arteries.
Figure S8. Neurovascular phantom model used in the benchtop verification.
Figure S9. Nomenclature for angulation and rotation of C-arm fluoroscope.
Figure S10. Telerobotically assisted aneurysm coil embolization in the right middle cerebral artery.
Figure S11. Telerobotically assisted clot retrieval procedure in the cerebral vasculature performed under x-ray fluoroscopy.
Figure S12. Navigation in the left middle cerebral artery under a semi-lateral projection.
Figure S13. Simulated biplane fluoroscopy based on combination of two monoplane results and C-arm configurations.
Figure S14. Experimental demonstration of magnetic steering and navigation in under biplane x-ray fluoroscopy.
Figure S15. Learning curve assessment for magnetic steering and navigation through real-time teleoperation of the system under fluoroscopic imaging.
Figure S16. Individual learning curves for novices performing magnetic steering and navigation through real-time teleoperation of the system under fluoroscopic imaging.
Figure S17. Workload assessment using the NASA Task Load Index during the comparison of the interventionalist's performances with the manually controlled passive guidewire and with the telerobotically controlled magnetic guidewire for 10 consecutive trials in fig. S16.
Legends for movies S1 to S8

Other Supplementary Materials for this manuscript includes the following:

Movie S1 (.mp4 format). Benchtop demonstration of telerobotically controlled magnetic steering and navigation in cerebral arteries of a 3D neurovascular model.

Movie S2 (.mp4 format). In vitro demonstration of magnetic steering and navigation in a realistic human head phantom with intracranial arteries under real-time x-ray fluoroscopy.

Movie S3 (.mp4 format). In vitro demonstration of telerobotically assisted aneurysm coil embolization in the left middle cerebral artery under real-time x-ray fluoroscopy.

Movie S4 (.mp4 format). In vitro demonstration of telerobotically assisted aneurysm coil embolization in the right middle cerebral artery under real-time x-ray fluoroscopy.

Movie S5 (.mp4 format). In vitro demonstration of telerobotically assisted clot retrieval thrombectomy and revascularization in the right middle cerebral artery.

Movie S6 (.mp4 format). In vivo demonstration of magnetic steering and navigation in the porcine brachial artery with accentuated tortuosity in the maximally flexed forelimb position.

Movie S7 (.mp4 format). Conventional neurovascular guidewire with pre-bent tip manually controlled by a neurointerventionalist for performance comparison.

Movie S8 (.mp4 format). Performance evaluation of the telerobotically controlled magnetic guidewire in comparison with a manually controlled passive guidewire.

List of Acronyms and Abbreviations (in order of appearance)

DOF	degree of freedom
TPU	thermoplastic polyurethane
NdFeB	neodymium-iron-boron
ICA	internal carotid artery (see **fig. S2** and **S8**)
MCA	middle cerebral artery (see **fig. S2** and **S8**)
ACA	anterior cerebral artery (see **fig. S2** and **S8**)
ACoA	anterior communicating artery (see **fig. S2** and **S8**)
PCoA	posterior communicating artery (see **fig. S8A**)
AP	anteroposterior (see **fig. S9**)
LAT	lateral (see **fig. S9**)
CRA	cranial (see **fig. S9**)
CAU	caudal (see **fig. S9**)
LAO	left anterior oblique (see **fig. S9**)
RAO	right anterior oblique (see **fig. S9**)

Supplementary Text

Transition between attraction and repulsion modes

Transition between the attraction and repulsion modes can be achieved through flipping the magnet by rotating the axis 7 of the robot arm by 180°, during which the steerable tip of the guidewire also changes its configuration in response to the rotation of the magnet, as illustrated in **fig. S5A**. The rotation angle (denoted α in **fig. S5A**) is defined as the deviation of the central axis of the magnet from its unrotated state (in the attraction mode with $\varphi = 90°$ in **fig. S5A**). Rotating the magnet along the current bending direction of the guidewire tip (i.e., either clockwise or counterclockwise) causes the tip to unwind itself, decreasing the deflection angle θ, when transitioning from either the attraction or the repulsion mode to an intermediate state (**fig. S5A**). Counter-rotating the magnet reverse to the current bending direction, on the other hand, causes the guidewire tip to bend further toward or away from the magnet, increasing the deflection angle, when transitioning from an intermediate state to the attraction or the repulsion mode, as illustrated in **fig. S5A**. The behavior of the guidewire tip in response to the rotation of the magnet, which is initially positioned at $\varphi = 90°$ with $\alpha = 0°$ (i.e., attraction mode), is characterized while varying α from –45° to 225° as presented in **fig. S5B**.

Compatibility with standard biplane fluoroscopy

The demonstrations presented in the paper were mostly based on single-plane fluoroscopy for real-time imaging and state observation. While it was possible to perform each navigational task under single-plane imaging as demonstrated in the presented experimental results, we found that having two different projections under biplanar imaging could be beneficial for state observation of the guidewire tip in complex angulations of intracranial vessels. To illustrate this point, we navigated the same path demonstrated in **Fig. 5A** under different C-arm configuration with cranial angulation of 6° and right anterior oblique rotation of 80° to provide a semi-lateral projection, as shown in **fig. S12**. Although the given task could be performed under a single projection in each experiment, we found that the two projections could be complementary to each other. For example,

the semi-anteroposterior projection (with cranial angulation of 23° and right anterior oblique rotation of 19°) provided a better view of the guidewire tip around the small aneurysm at the internal carotid artery (ICA) bifurcation (A1-M1 junction), while the semi-lateral projection allowed better observation of the guidewire tip orientation at the middle cerebral artery (MCA) bifurcation, as illustrated and compared in **fig. S13**.

To verify our system's compatibility with standard biplane fluoroscopy in terms of the available workspace for the robot arm, we also performed the navigational task demonstrated in **Fig. 4** (from the left ICA to the M2 segments with the human head phantom) in a neurointerventional biplane angiography suite as shown in **fig. S14**. Based on the reconstructed 3D vessel model from rotational angiography (**fig. S14A**), two different projections were determined to provide clear view of all the important anatomical landmarks in the target vasculature as shown in **fig. S14**, **B** and **C**. The semi-anteroposterior projection (with cranial angulation of 19° and right anterior oblique rotation of 40°) showed the left ICA bifurcation (A1-M1 junction) more clearly, while the semi-lateral projection (with cranial angulation of 6° and right anterior oblique rotation of 118°) showed the aneurysm at the carotid siphon and the MCA bifurcation more clearly, as shown in **fig. S14**, **D** and **E**, respectively. During the navigation, the semi-lateral projection helped to better identify the guidewire tip orientation at locations where the semi-anteroposterior projection alone might not suffice, allowing for safer manipulation of the guidewire with reduced potential risks of the aneurysm present on the path being touched or struck by the guidewire. Throughout the entire navigation under biplane fluoroscopy, the actuating magnet approached the head space most closely when steering the magnetic guidewire at the carotid siphon with an aneurysm in the left ICA. The corresponding magnet position and robot configuration are visualized and shown from different perspectives in **fig. S14**, **F** and **G**, respectively. This reveals that there was a sufficient gap between the magnet and the head surface even when the magnet was closest to the phantom at the moment. Overall, the available workspace between the two C-arms was sufficient for the robot arm to manipulate the magnet around the head phantom (or equivalently the virtual patient's head shown in **fig. S14F**) without collisions while steering the guidewire in the intracranial vessels.

Supplementary Figures

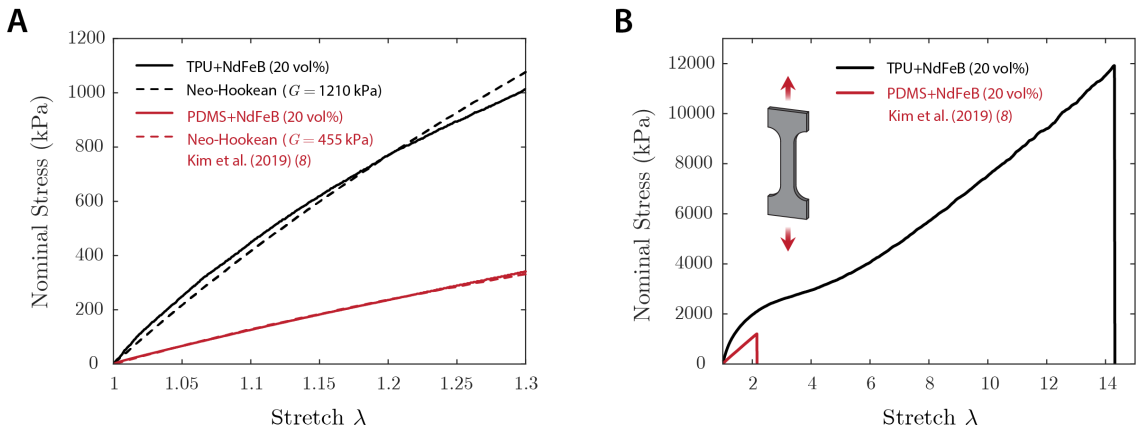


Figure S1. Mechanical characterization of the magnetic polymer composites. Nominal tensile stress-stretch curve for the magnetic polymer composite based on TPU+NdFeB (20 volume %) plotted (**A**) over a range of small stretch ($\lambda < 1.3$) for measuring shear modulus and (**B**) up to the fracture point ($\lambda = 14.3$) for measuring tensile strength and stretchability. With the TPU-based composite, both the tensile strength and the stretchability have been greatly improved (by 10 and 7 times, respectively) when compared with the PDMS-based composite that was used for the previously demonstrated prototype of the magnetic guidewire (8). TPU: thermoplastic polyurethane; NdFeB: neodymium-iron-boron; PDMS: polydimethylsiloxane.

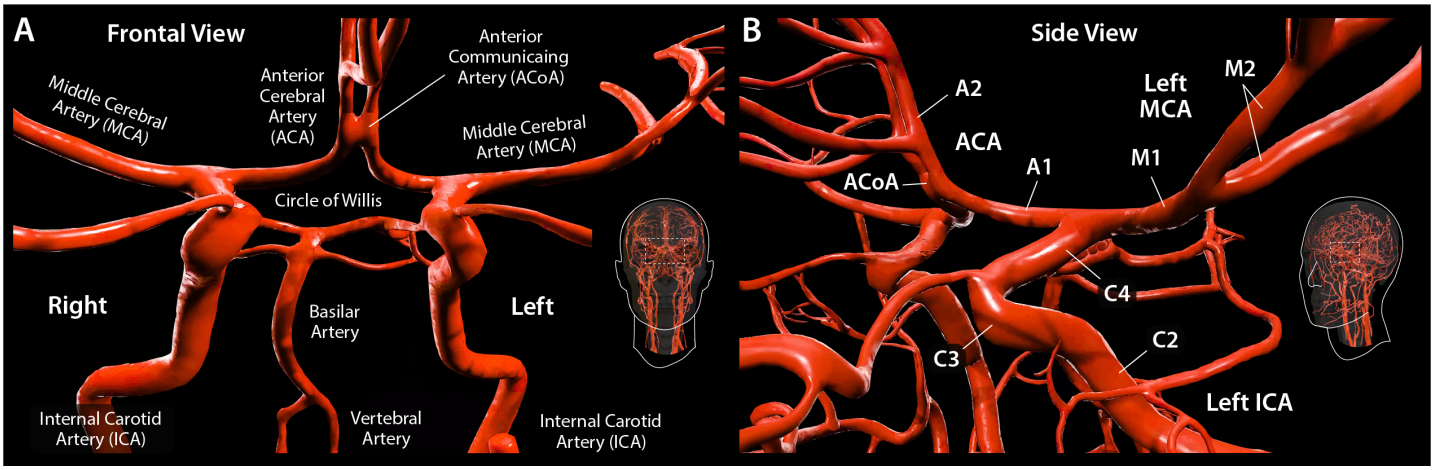


Figure S2. Anatomy and nomenclature of intracranial arteries. (**A**) Major arteries within the cranium are presented on the frontal plane. (**B**) Different branches and segments of the internal carotid artery (ICA; C2, C3, and C4), anterior cerebral artery (ACA; A1 and A2), and middle cerebral artery (MCA; M1 and M2) in the left hemisphere are indicated. For the segments of the ICA, several classification schemes and various numbering systems exist. Here, we follow the simple system corresponding to the description by Gibo and colleagues (63): C4: Supraclinoid, C3: Cavernous, C2: Petrous, C1: Cervical (C1 is not shown in the figure).

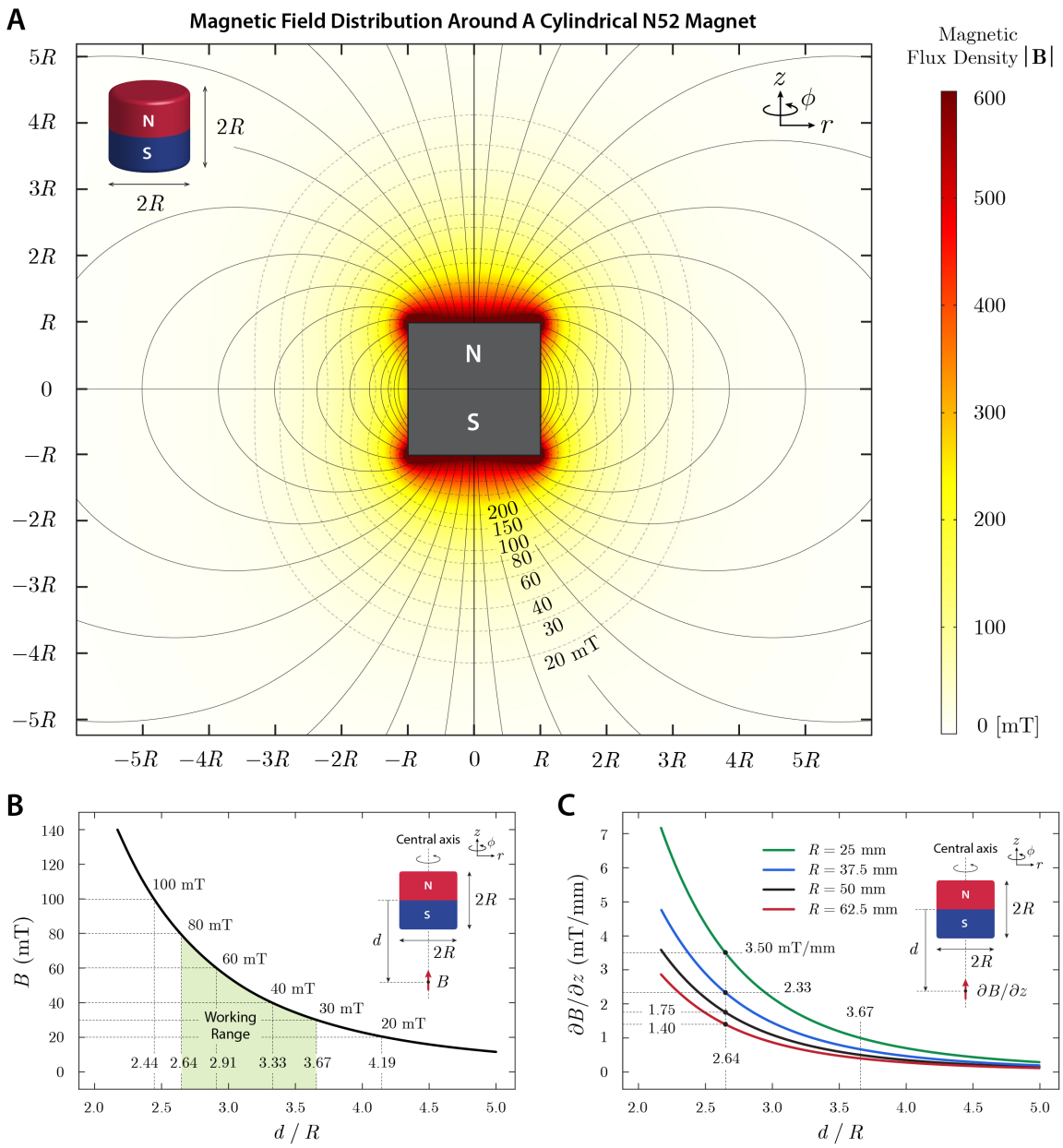


Figure S3. Magnetic fields around a cylindrical magnet. (**A**) Axisymmetric magnetic field distribution around a N52-grade cylindrical magnet with diameter and thickness of $2R$ and remanence $B_{\mathrm{re}} = 1.45$ T. The solid lines indicate the field directions, and the dotted lines form the contours around which the magnetic flux densities are the same as the indicated values on the field map. (**B**) Magnetic flux density B along the central axis of the magnet plotted against the normalized working distance d / R. For typical steering tasks, the required magnetic field strength ranges from 30 to 80 mT, which correspond to the upper ($d / R = 3.67$) and lower ($d / R = 2.64$) boundaries of the working range for the magnet in the attraction and repulsion modes. (**C**) Magnetic field gradients $\partial B / \partial z$ along the axial direction plotted against the normalized working distance d / R for different sized magnets of the same shape ($R = 25$, 37.5, 50, 62.5 mm). The field gradient values at the lower boundary of the working range ($d / R = 2.64$) are presented on the plot.

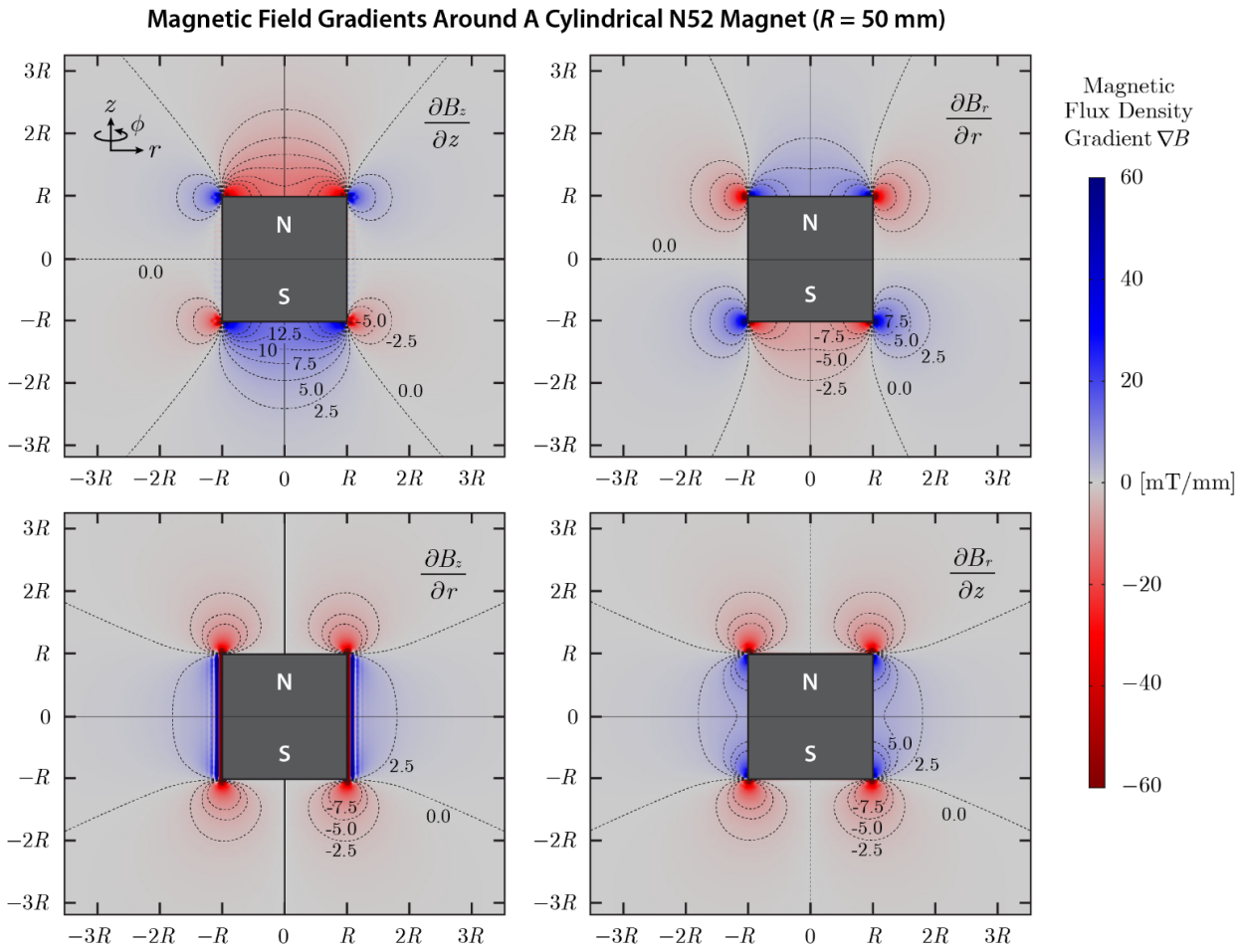


Figure S4. Spatial gradients of the magnetic fields around a cylindrical magnet. All the non-zero components of the field gradients are presented for a N52-grade cylindrical magnet with remanence $B_{\mathrm{re}} = 1.45$ T and diameter and thickness of 100 mm, which is considered the ideal size for the actuating magnet to be used in clinical settings given the average head size and the field strength at a typical range of working distance. Along the center axis of the magnet, the diagonal terms of the field gradient tensor in Eq. (2) (i.e., $\partial B_z / \partial z$ and $\partial B_r / \partial r$) give rise to magnetic body forces acting on the steerable tip of the guidewire, whereas the off-diagonal terms (i.e., $\partial B_z / \partial r$ and $\partial B_r / \partial z$) are effectively zero along the center line.

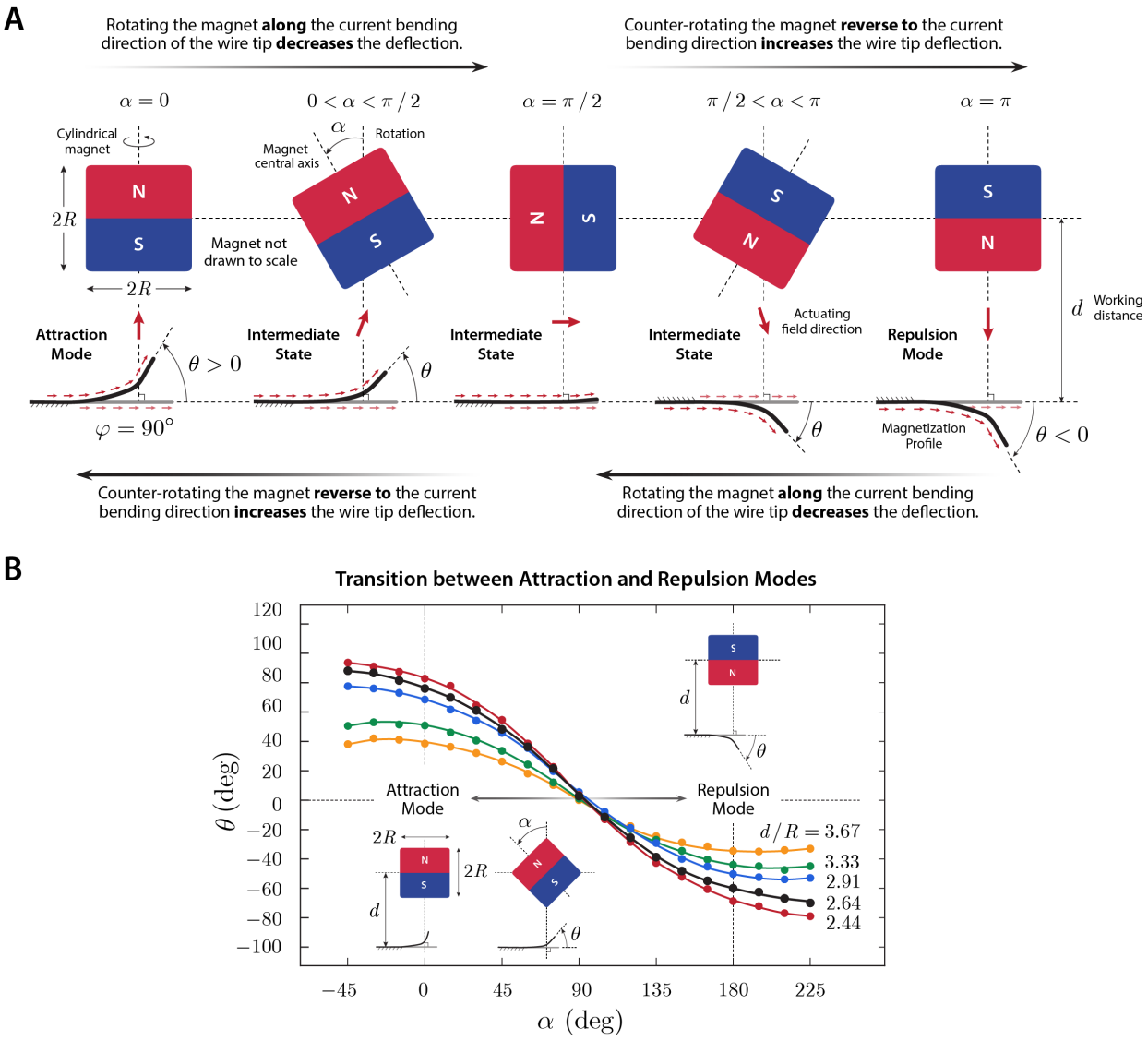


Figure S5. Transition between the attraction and repulsion modes. (**A**) Schematic representation and (**B**) characterization of the magnetic guidewire's behavior during the transition between the attraction and repulsion modes. Rotating the magnet along the current bending direction of the guidewire tip (i.e., either clockwise or counterclockwise) causes the tip to unwind itself, decreasing the deflection angle θ, when transitioning from either the attraction or the repulsion mode to an intermediate state. Counter-rotating the magnet reverse to the current bending direction, on the other hand, causes the tip to bend further toward or away from the magnet, increasing the deflection angle, when transitioning from an intermediate state to the attraction or the repulsion mode.

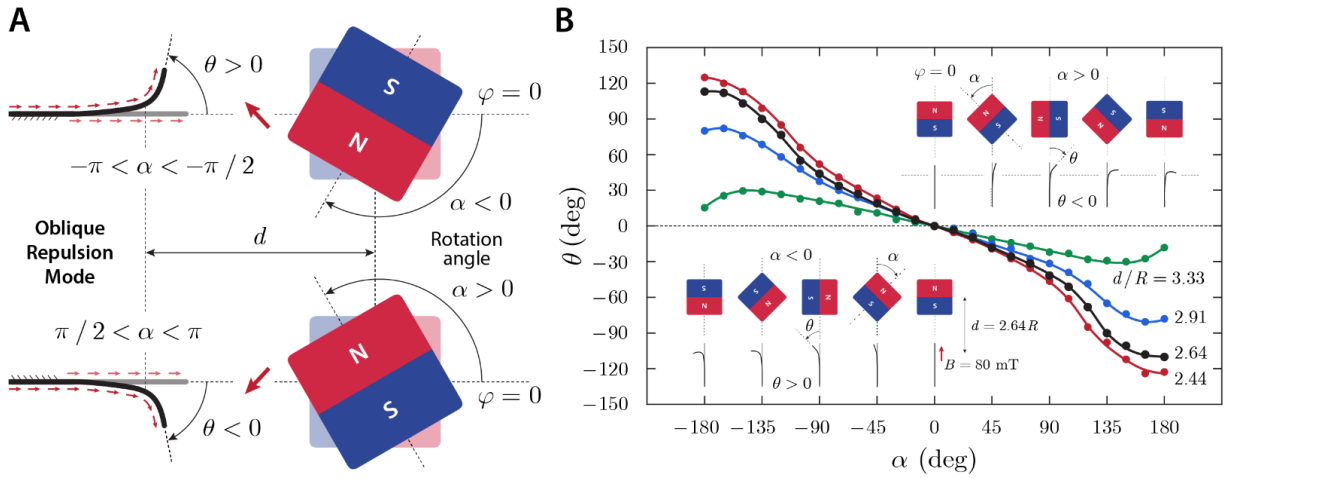


Figure S6. Definition and characterization of the oblique repulsion mode. (**A**) Schematic representation of the oblique repulsion mode in which the guidewire tip deflects in response to the magnet's peripheral fields outside of the core fields along the axial direction. The rotation angle α is defined as the deviation of the central axis of the magnet from its unrotated state, in which the magnet is positioned at the zero angular position ($\varphi = 0$) with its axis aligned with the undeformed tip of the guidewire from some working distance d. (**B**) Characterization of the tip deflection angle θ while varying the rotation angle α from –180° to 180° at different normalized working distance d/R. When the magnet rotates clockwise ($\alpha < 0$) from the unrotated state, the guidewire tip bends counterclockwise ($\theta > 0$); when the magnet rotates counterclockwise ($\alpha > 0$), the guidewire tip bends clockwise ($\theta < 0$).

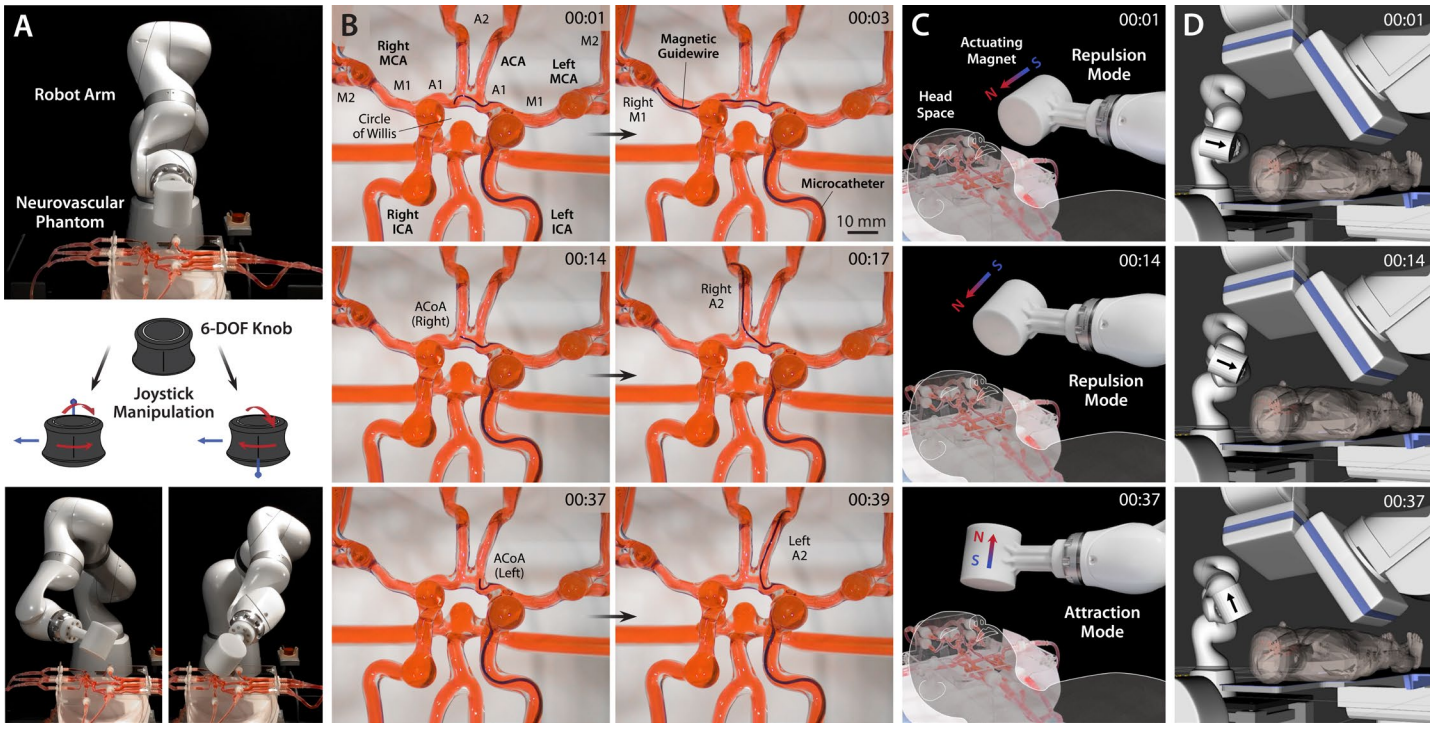


Figure S7. Benchtop demonstration of telerobotically controlled magnetic steering and navigation in cerebral arteries. (**A**) Real-time teleoperation of the robot arm for spatial positioning of the actuating magnet around a life-sized neurovascular phantom used for benchtop verification. The actuating magnet can be manipulated intuitively through position control of the robot arm's end-effector with a 6-DOF joystick controller. (**B**) Magnetic steering and navigation in different branches of cerebral arteries. The magnetic guidewire is advanced from the internal carotid artery (ICA) bifurcation (A1-M1 junction) under repulsive steering to reach the left A1 segment and then the right A1 and M1 segments sequentially (00:01~00:03). After repositioning the magnet to reduce the steering torque, the guidewire is advanced to reach the right A2 segment of the anterior cerebral artery (ACA) under the repulsive steering mode (00:14~00:17). After flipping the magnet to utilize attractive steering, the guidewire tip is directed toward the left A2 segment and advanced (00:37~00:39). (**C-D**) The robot arm's motion and configuration are visualized during the demonstrated steering and navigational task. The C-arm and human patient models implemented in the robot arm's virtual task space simulate the realistic workspace constraints in clinical settings for neurovascular interventions under biplane fluoroscopy. Demonstration of the entire navigation and steering control procedures is available in **movie S1**.

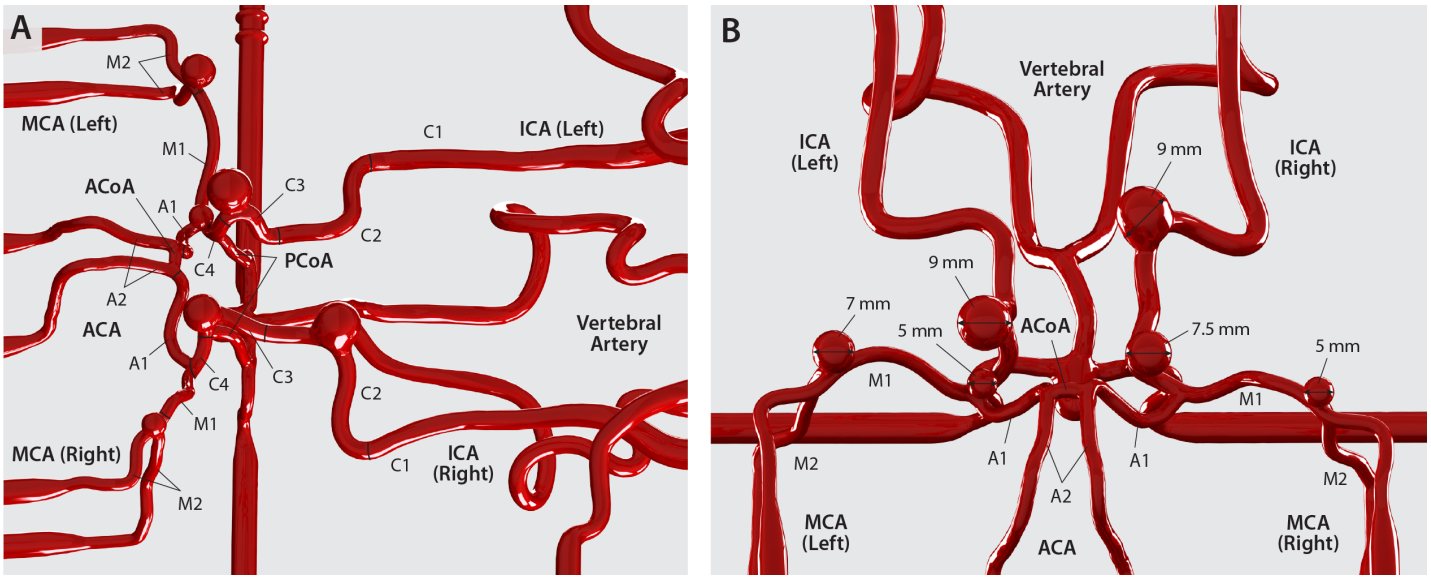


Figure S8. Neurovascular phantom model used in the benchtop verification. (**A**) Anatomy and nomenclature of the phantom neurovasculature (ICA: internal carotid artery; MCA: middle cerebral artery; ACA: anterior cerebral artery; ACoA: anterior communicating artery; PCoA: posterior communicating artery). The ICA is divided into supraclinoid (C4), cavernous (C3), petrous (C2), and cervical (C1) segments, following (62). The acute-angled corner between the cavernous and supraclinoid portions of the ICA is defined as the carotid siphon. (**B**) Detailed location and dimensions of the aneurysms present in the anatomical model. The given dimensions indicate the inner diameter of the aneurysms.

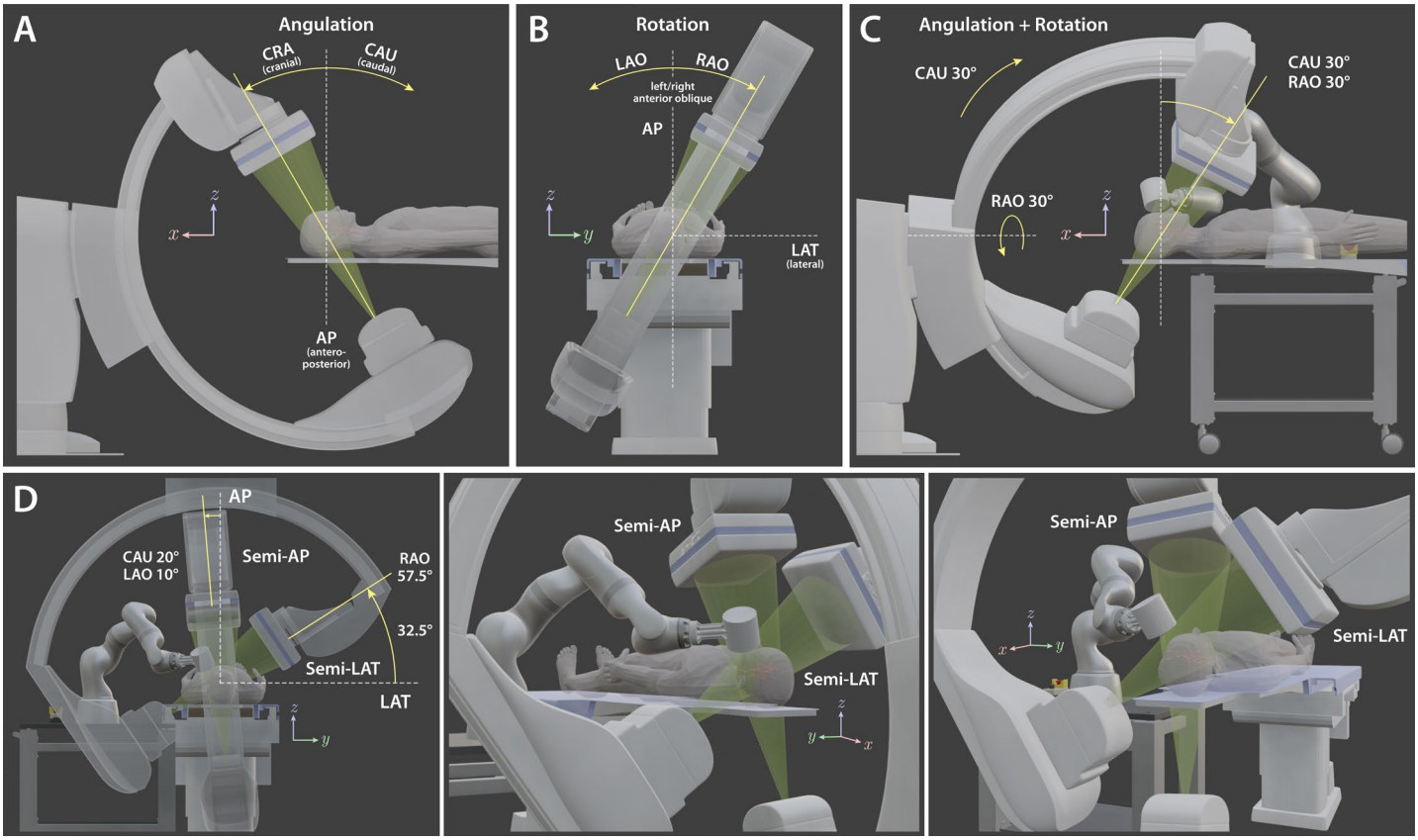


Figure S9. Nomenclature for angulation and rotation of C-arm fluoroscope. (**A**) The term *angulation* refers to orbital rotation of the C-arm around the y-axis from the upright position for anteroposterior (AP) projection. Depending on the direction of angulation and the resulting change in the position of the image detector relative to the patient, the angulated C-arm configuration is defined as either cranial (CRA) or caudal (CAU) position. (**B**) The term *rotation* refers to tilting of the C-arm sideways around the x-axis from the upright position for AP projection. Depending on the direction of rotation and the resulting change in the position of the image detector relative to the patient, the rotated C-arm configuration is defined as either left/right anterior oblique (LAO/RAO) position. (**C**) If the C-arm is angulated in the CAU direction by 30° and rotated toward the RAO position by 30°, the resulting configuration is referred to as CAU 30° and RAO 30°. (**D**) Illustration of the robot arm deployed in biplanar imaging settings for complex neurovascular interventions based on a pair of C-arms for simultaneous projections from two different angles.

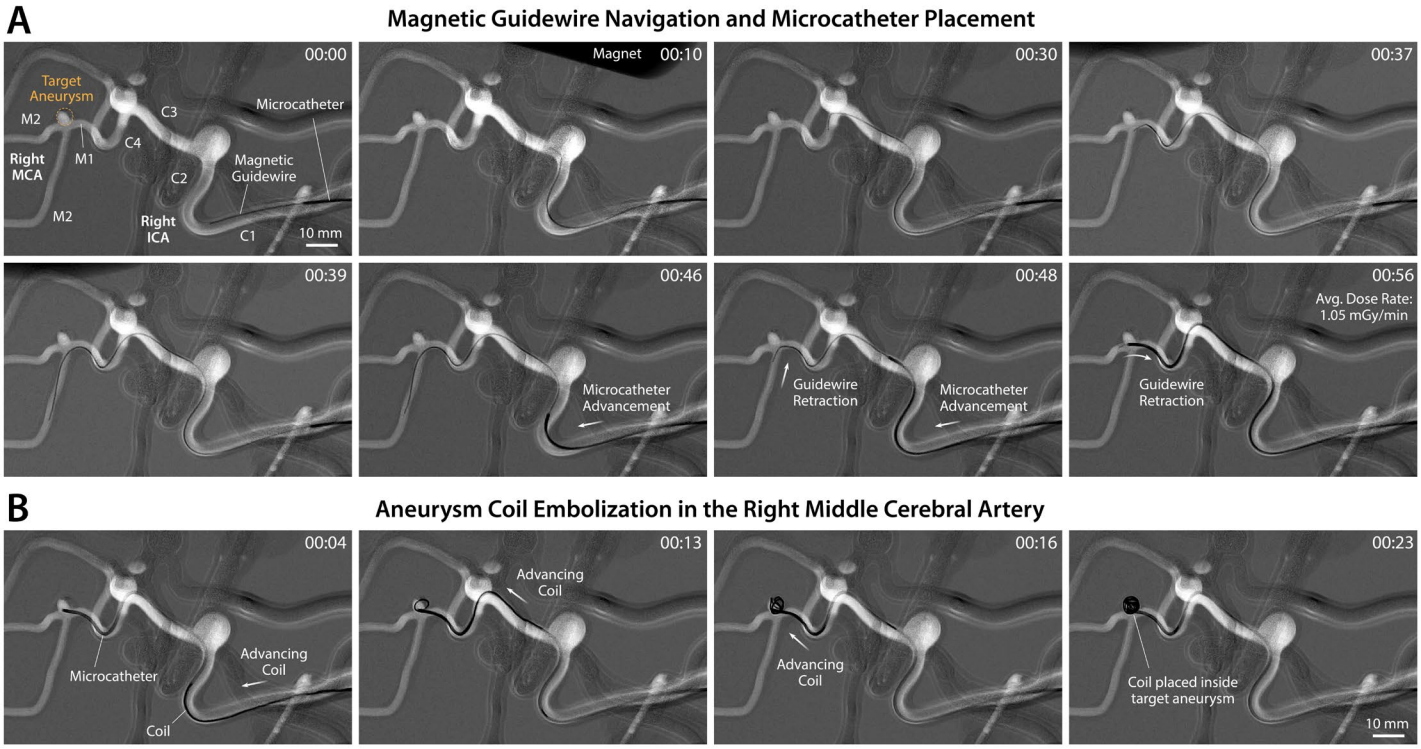


Figure S10. Telerobotically assisted aneurysm coil embolization in the right middle cerebral artery. (**A**) Guidewire navigation under magnetic manipulation up to the target lesion in the right middle cerebral artery (MCA) through real-time teleoperation of the robot arm (00:00~00:39) and microcatheter placement in the targeted aneurysm upon the retraction of the guidewire (00:46~00:56). (**B**) Endovascular coiling of the targeted aneurysm by delivering embolization coils into the aneurysm sac through the microcatheter. Demonstration of the entire navigation, steering control, and coiling procedures is available in **movie S4**. The average time ($\pm$ standard deviation) it took to complete the demonstrated guidewire navigation and microcatheter placement in the targeted aneurysm in (**A**) was 57.6 $\pm$ 3.2 s ($n = 3$) and the coiling of the aneurysm in (**B**) was 22.3 $\pm$ 1.5 s ($n = 3$), respectively.

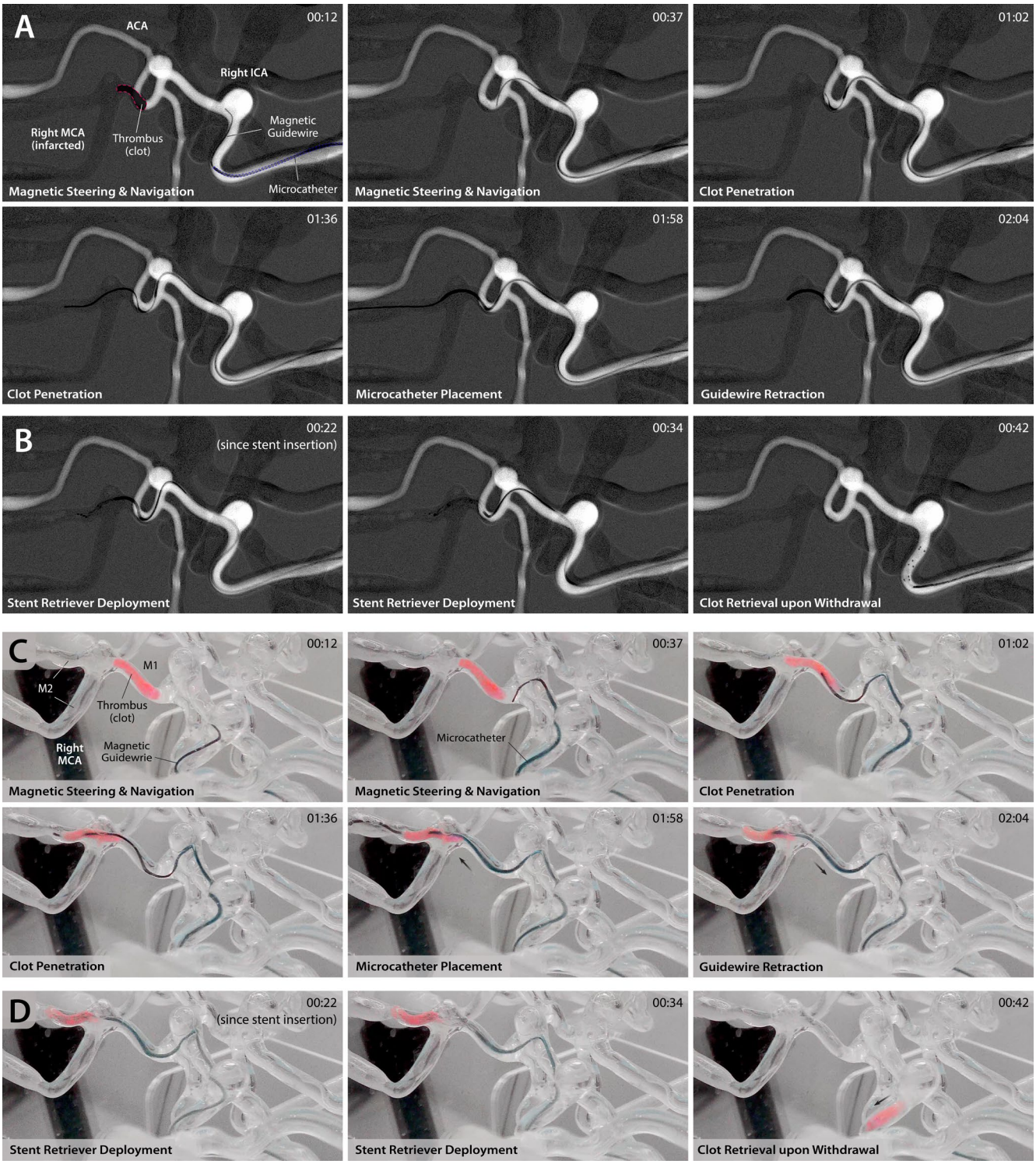


Figure S11. Telerobotically assisted clot retrieval procedure in the cerebral vasculature performed under x-ray fluoroscopy. (**A**) Navigation up to the simulated clot in the M1 segment of the right middle cerebral artery (MCA) with the telerobotically controlled magnetic guidewire (00:00~00:37) and microcatheter placement across the thrombus with the aid of magnetic steering at the MCA bifurcation (01:02~02:04) under real-time x-ray fluoroscopy. (**B**) Deployment of a stent retriever across the thrombus (00:22~00:34) and retrieval of the clot from the occluded site (00:42) through joystick teleoperation of the guidewire/microcatheter advancing unit. The guidewire advancing unit was used to advance/retract the stent retriever after device exchange upon the withdrawal of the magnetic guidewire from the microcatheter. (**C-D**) Corresponding optical images of the demonstrated clot retrieval process in (**A-B**) juxtaposed for showing the clot which is not visible under x-ray by itself.

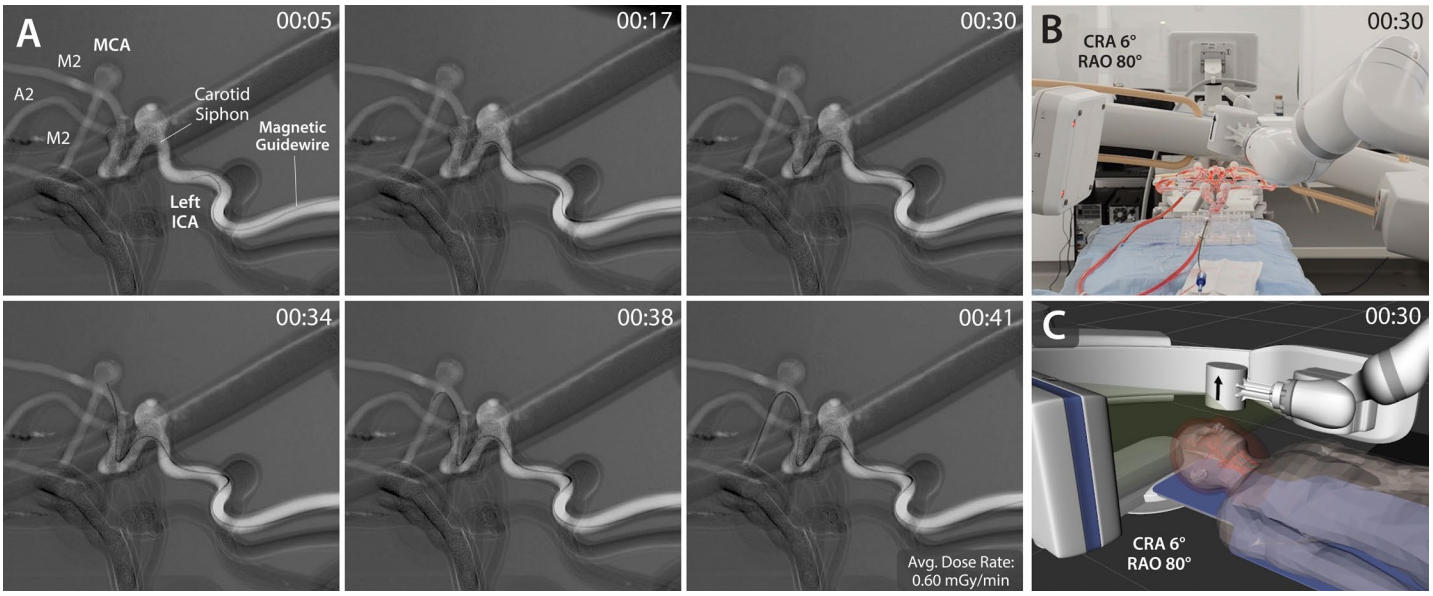


Figure S12. Navigation in the left middle cerebral artery under a semi-lateral projection. (**A**) The magnetic guidewire navigating from the left internal carotid artery (ICA) to the inferior M2 segment of the left middle cerebral artery (MCA) of the 3D neurovascular phantom. (**B-C**) With cranial angulation of 6° (CRA 6°) and right anterior oblique rotation of 80° (RAO 80°), the C-arm provides a semi-lateral projection for the target vasculature in the demonstrated navigation. Under this semi-lateral projection, the guidewire tip was observed more clearly while at the acute-angled corners in the carotid siphon and the MCA bifurcation (00:17 and 00:38), when compared with the semi-anteroposterior projection presented in **Fig. 5A** (see 00:12 and 00:34 for comparison). The average time ($\pm$ standard deviation) it took to complete the demonstrated navigational task was 43.0 ± 5.6 s ($n = 5$).

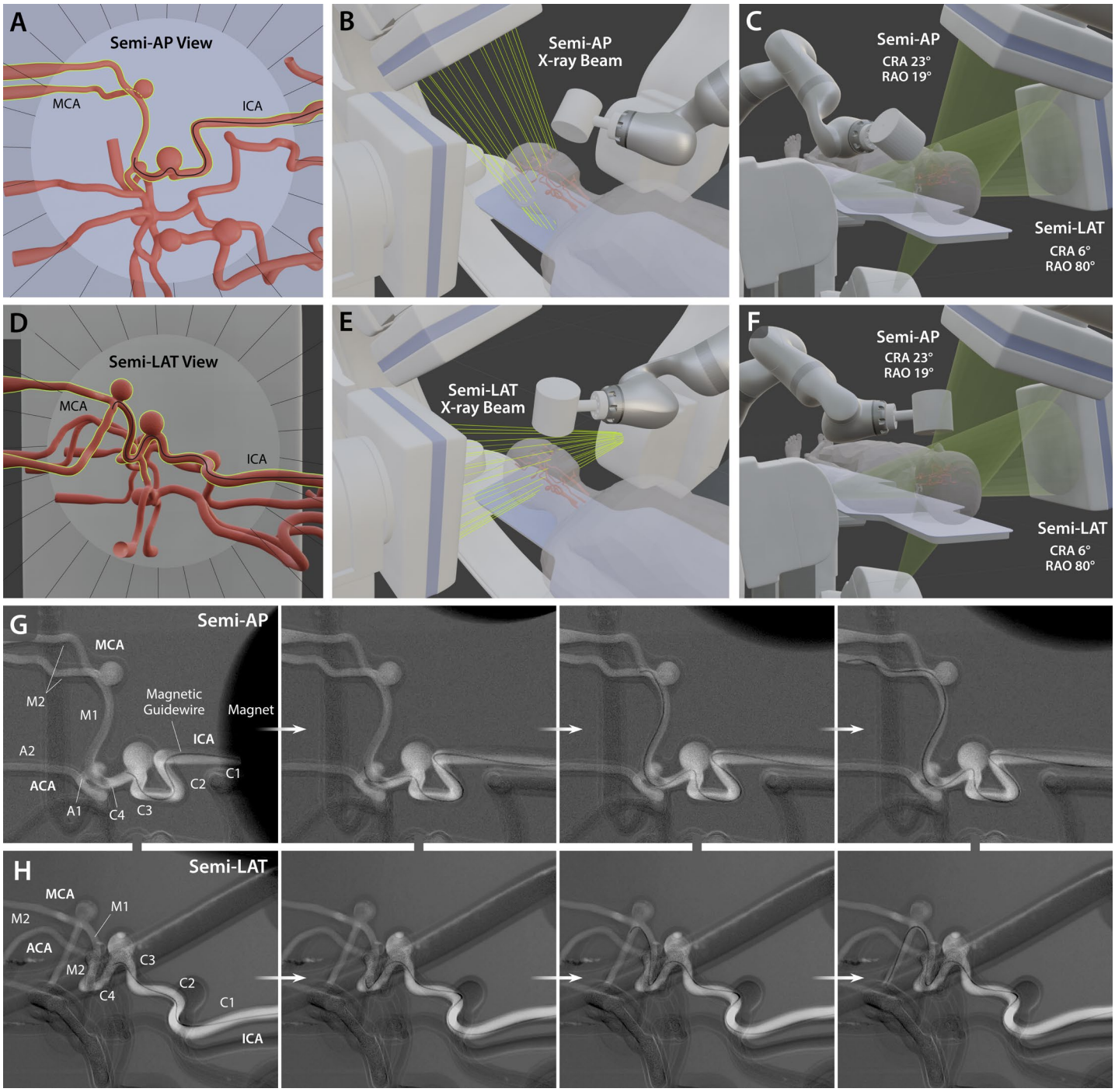


Figure S13. Simulated biplane fluoroscopy based on combination of two monoplane results and C-arm configurations. (**A-C**) When the guidewire tip is at the internal carotid artery (ICA) bifurcation (A1-M1 junction), the semi-anteroposterior (AP) projection can best visualize the tip movement. For effective steering of the guidewire tip at the ICA bifurcation, the actuating magnet is positioned mostly sideways with its movement in the lateral direction, and the magnet would not block the view of the guidewire tip on the semi-AP projection. (**D-F**) When the guidewire tip reaches the middle cerebral artery (MCA) bifurcation (M1-M2 junction), the semi-lateral (LAT) projection provides a clearer view of the guidewire tip deflection, which is now driven by the magnet moving mostly in the vertical direction. Therefore, the magnet would not block the view of the guidewire tip on the semi-LAT projection. (**G-H**) The monoplane fluoroscopic images of magnetic navigation presented in **Fig. 5A** and **fig. S12** in the same vascular path are combined and synchronized to simulate biplane settings with simultaneous projections of semi-AP and semi-LAT. As illustrated in (**C**) and (**F**), the available workspace is sufficient for the robot arm to manipulate the magnet.

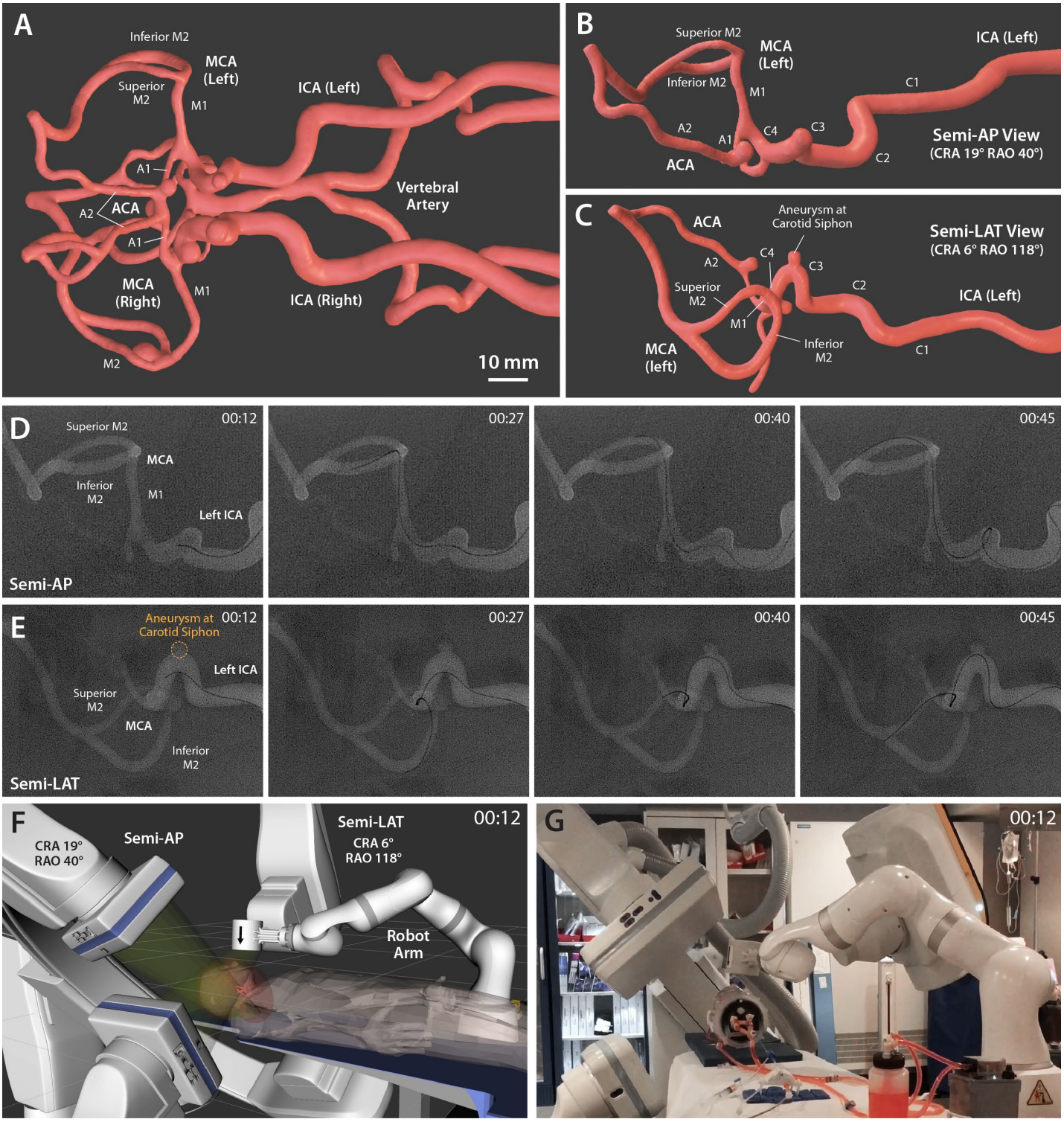


Figure S14. Experimental demonstration of magnetic steering and navigation in under biplane x-ray fluoroscopy. (**A**) Reconstructed 3D vascular structure of the intracranial arteries of the human head phantom obtained from rotational angiography. (**B**) Semi-anteroposterior (AP) view of the target vasculature from the left ICA to MCA providing clear view of the ICA bifurcation (A1-M1 junction). ICA: internal carotid artery; MCA: middle cerebral artery. (**C**) Semi-lateral (LAT) view providing clear view of the aneurysm at the carotid siphon and the superior and inferior M2 segments at the MCA bifurcation. (**D-E**) Fluoroscopic images of the magnetic guidewire navigating in the target vasculature from the two different projections (semi-AP with cranial angulation of 19° (CRA 19°) and right anterior oblique rotation of 40° (RAO 40°) and semi-LAT with CRA 6° and RAO 118°). (**F-G**) Real-time visualization and actual view of the teleoperated robot arm under the biplane fluoroscopy setting. The available workspace between the two C-arms was sufficient for the robot arm to manipulate the magnet around the head phantom/virtual patient.

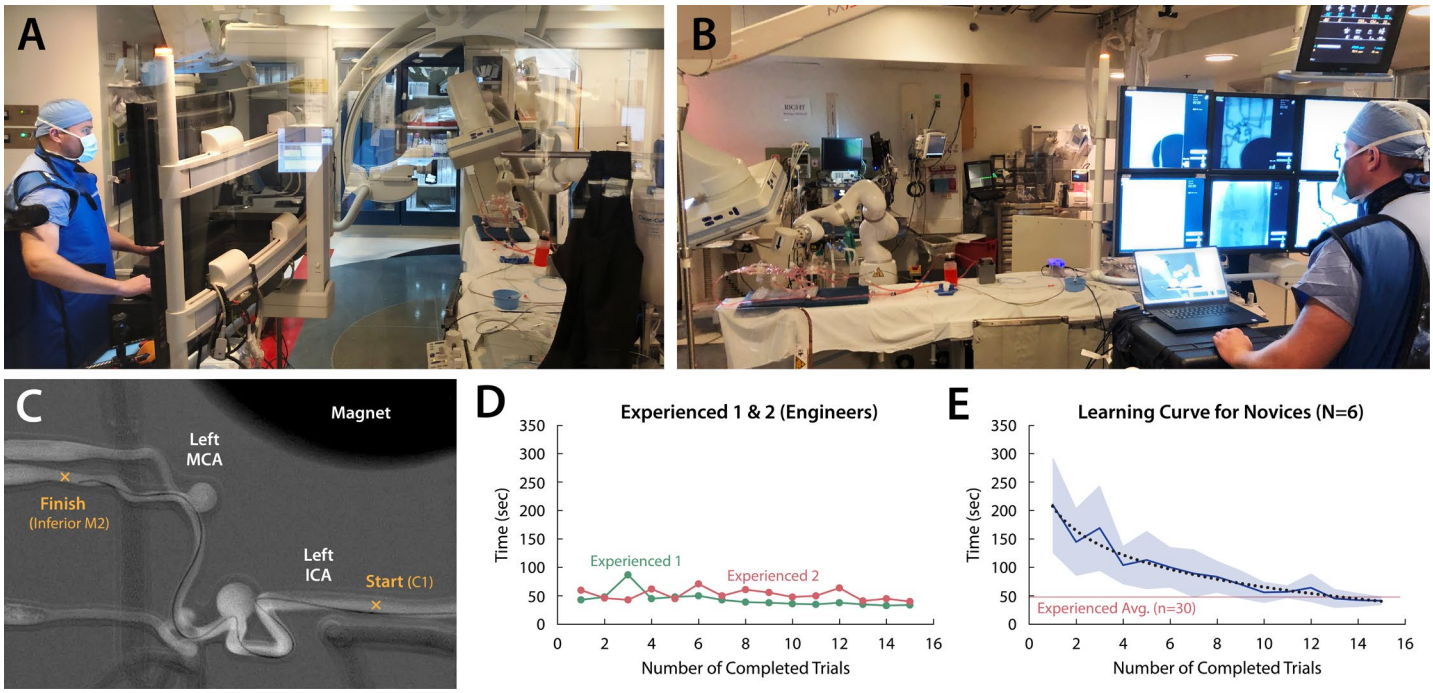


Figure S15. Learning curve assessment for magnetic steering and navigation through real-time teleoperation of the system under fluoroscopic imaging. (**A-B**) Experimental setup for the usability testing and learning curve assessment using a 3D neurovascular phantom under single-plane x-ray fluoroscopy. (**C**) Defined navigational task for the learning curve assessment from the left internal carotid artery (ICA) to the inferior M2 segment of the middle cerebral artery (MCA). (**D**) Time taken for experienced users to complete the defined task versus the number of completed trials (15 trials each from 2 experienced users). (**E**) Average learning curve for the novice group (2 engineers and 4 neuro-interventionalists with no prior experience with the developed system) based on the average procedural time (mean $\pm$ standard deviation) for each trial. The mean values are fitted with a logarithmic curve, and the standard deviation is given as the shaded area below and above the curve. The individual learning curves are presented in **fig. S16**. Comparison of the steering and navigational performances of an experienced neurointerventionalist with the manually controlled passive guidewire and the telerobotically controlled magnetic guidewire (after training) for the same navigational task is available in **Fig. 8** with **movies S7** and **S8**. Comparison of the operator's workload assessed via the NASA Task Load Index is available in **fig. S17**.

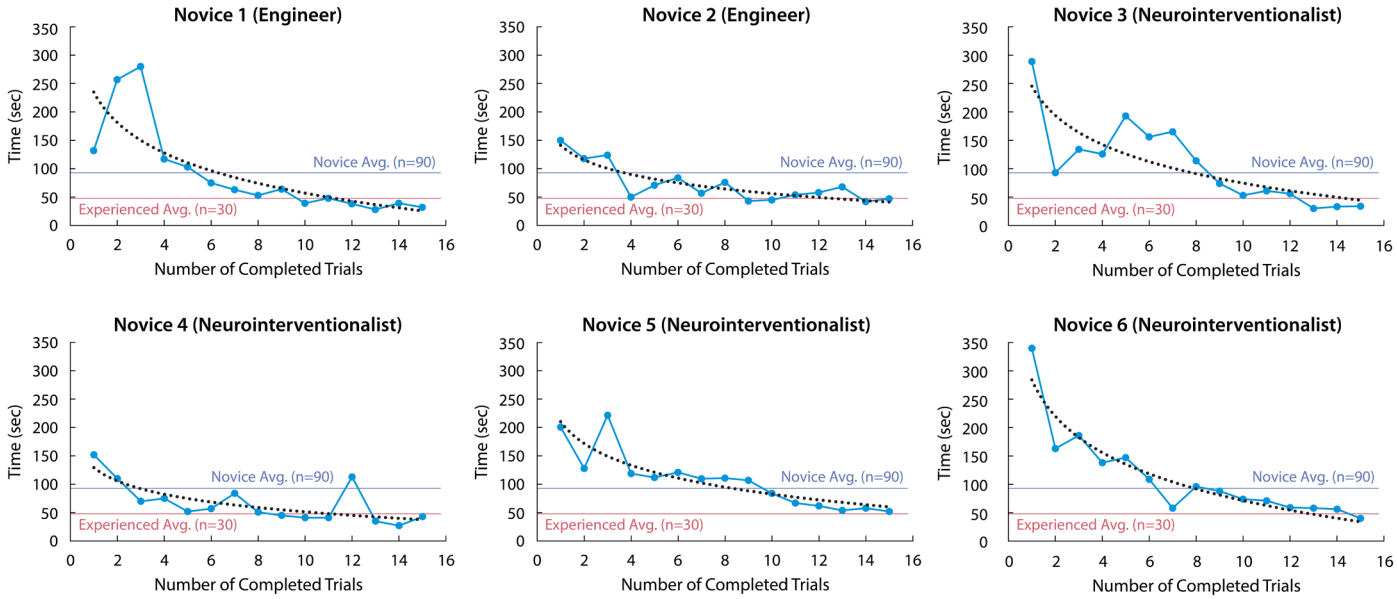


Figure S16. Individual learning curves for novices performing magnetic steering and navigation through real-time teleoperation of the system under fluoroscopic imaging. The average time it took for each participant in the novice group (2 engineers and 4 neurointerventionalists with no prior experience with the developed system) to complete the defined task in **fig. S15C** versus the number of completed trials (fitted with a logarithmic curve), which is compared with the average procedural time for the experienced group ($n = 30$; 15 trials from each of the 2 experienced users) as well as the total average of the novice group ($n = 90$; 15 trials from each of the 6 novices).

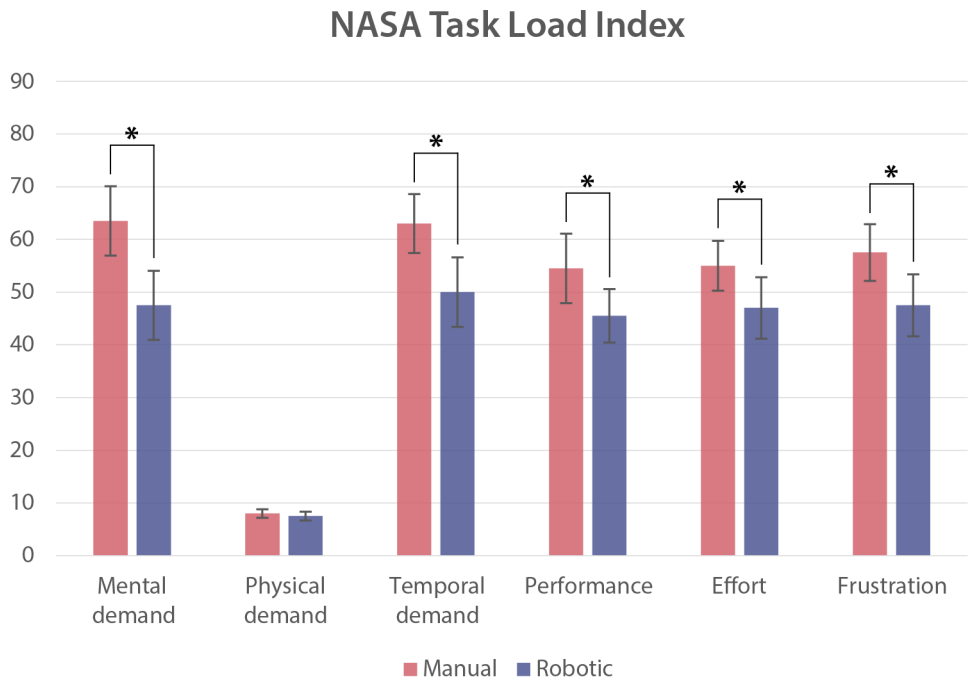


Figure S17. Workload assessment using the NASA Task Load Index during the comparison of the interventionalist's performances with the manually controlled passive guidewire and with the telerobotically controlled magnetic guidewire for 10 consecutive trials in Fig. 8. Mental demand indicates how much mental and perceptual activity was required. Physical demand indicates how much physical activity was required. Temporal demand indicates how much time pressure the operator felt due to the rate or pace at which the tasks or task elements occurred. Performance indicates how successful the operator thinks he/she was in accomplishing the goals of the task. It should be noted that a lower score indicates that the operator was more satisfied with his/her performance during the task. Effort indicates how hard the operator had to work both mentally and physically to accomplish his/her level of performance. Frustration level indicates how discouraged and stressed the operator felt during the task. Error bars with whiskers indicate standard errors of the mean scores from the 10 consecutive trials ($n = 10$). Statistically significant differences are indicated with asterisks ($^*P < 0.05$).

Supporting Movies

Movie S1. Benchtop demonstration of telerobotically controlled magnetic steering and navigation in cerebral arteries of a 3D neurovascular model. This video demonstrates selective navigation in different branches of the left/right middle and anterior cerebral arteries of the 3D neurovascular model under real-time teleoperation of the robot arm for spatial positioning of the actuating magnet. The robot arm's motion and configuration are visualized during the demonstrated steering and navigational task. The C-arm and human patient models implemented in the robot arm's virtual task space simulate the realistic workspace constraints in clinical settings for neurovascular interventions under biplane fluoroscopy.

Movie S2. In vitro demonstration of magnetic steering and navigation in a realistic human head phantom with intracranial arteries under real-time x-ray fluoroscopy. This video demonstrates our system's capability to assist therapeutic procedures for endovascular treatments of cerebral aneurysms with a life-sized anatomical model. The magnetic guidewire was first steered to reach the target lesion in the left middle cerebral artery, and then the microcatheter was advanced and placed in the targeted aneurysm. Then, embolization coils were delivered through the microcatheter into the aneurysm sac to fill up the cavity. The guidewire navigation and microcatheter placement were performed under teleoperation of the system, and the coil delivery and deployment were performed manually following the standard procedure, which involved inserting the coil introducer sheath into the hub of the microcatheter via a rotating hemostatic valve as well as tightening or loosening the hemostatic valve. The average time ($\pm$ standard deviation) it took to complete the demonstrated navigational task was 45.0 ± 4.0 s ($n = 5$).

Movie S3. In vitro demonstration of telerobotically assisted aneurysm coil embolization in the left middle cerebral artery under real-time x-ray fluoroscopy. This video demonstrates telerobotically performed aneurysm coiling in the left middle cerebral artery using our system under real-time x-ray fluoroscopy. The magnetic guidewire was first steered to reach the target lesion in the left middle cerebral artery, and then the microcatheter was advanced and placed in the targeted aneurysm. Then, embolization coils were delivered through the microcatheter into the aneurysm sac to fill up the cavity. The guidewire navigation, microcatheter placement, and the coil delivery and deployment were performed under teleoperation of the system. The average time ($\pm$ standard deviation) it took to complete the demonstrated guidewire navigation and microcatheter placement in the targeted aneurysm was 51.7 ± 3.5 s ($n = 3$), and the average time ($\pm$ standard deviation) it took to complete the coiling of the aneurysm was 32.3 ± 2.5 s ($n = 3$).

Movie S4. In vitro demonstration of telerobotically assisted aneurysm coil embolization in the right middle cerebral artery under real-time x-ray fluoroscopy. This video demonstrates telerobotically performed aneurysm coiling in the right middle cerebral artery using our system under real-time x-ray fluoroscopy. The magnetic guidewire was first steered to reach the most distal aneurysm in the right middle cerebral artery, and then the micro-catheter was advanced over the guidewire and placed in the aneurysm. Then, embolization coils were delivered through the microcatheter and deployed in the aneurysm sac. The guidewire navigation and microcatheter placement and the coil delivery and deployment were performed telerobotically, through remote control of the robot arm and the advancing units under visual feedback. The average time ($\pm$ standard deviation) it took to complete the demonstrated guidewire navigation and microcatheter placement in the targeted aneurysm was 57.6 ± 3.2 s ($n = 3$), and the average time it took to complete the coiling of the aneurysm was 22.3 ± 1.5 s ($n = 3$).

Movie S5. In vitro demonstration of telerobotically assisted clot retrieval thrombectomy and revascularization in the right middle cerebral artery. This video demonstrates our system's capability to assist therapeutic procedures for treating ischemic stroke due to cerebral infarction using a life-sized neurovascular phantom with a simulated clot in the M1 segment of the right middle cerebral artery. The magnetic guidewire was first steered to reach the occluded site and then the guidewire and the microcatheter were advanced under the joystick control to place the microcatheter across the thrombus. Then, a stent retriever device was delivered through the microcatheter and deployed in the thrombus, which was then retrieved upon the withdrawal of the stent and microcatheter to revascularize the occluded site. The average time ($\pm$ standard deviation) it took to complete the demonstrated guidewire navigation and microcatheter placement in the occluded site was 108.0 ± 14.0 s ($n = 3$), and the average time ($\pm$ standard deviation) it took to complete the clot retrieval using the stent retriever was 46.6 ± 5.0 s ($n = 3$).

Movie S6. In vivo demonstration of magnetic steering and navigation in the porcine brachial artery with accentuated tortuosity in the maximally flexed forelimb position. This video demonstrates our system's steering and navigational performance under realistic in vivo conditions. The navigational task was performed in the porcine brachial artery in the fully flexed forelimb position, which was to simulate the tortuosity of the human intracranial arteries. 3D rotational angiography was performed to obtain a reconstructed 3D model of the target vasculature for preprocedural planning of the robot operation and magnet positioning in the robot arms' virtual task space. Out of respect for the animal and to comply with the Institutional Animal Care and Use Committee (IACUC) policy on photography of research animals, the pig was covered during the video recording. The average time ($\pm$ standard deviation) it took to complete the demonstrated navigational task was 124.6 ± 19.7 s ($n = 5$).

Movie S7. Conventional neurovascular guidewire with pre-bent tip manually controlled by a neurointerventionalist for performance comparison. This video demonstrates the steering and navigational performance of a conventional neurovascular guidewire manually manipulated by an experienced neurointerventionalist based on twisting maneuver in a 3D neurovascular phantom under real-time x-ray fluoroscopy over 10 consecutive trials. The interventionalist has +4 years of training and experiences in neuroendovascular intervention and was given several practice trials to become familiar with the given phantom vasculature and to produce steady-state performances. The average time ($\pm$ standard deviation) it took for the interventionalist to complete the demonstrated task with the conventional guidewire was 63.7 ± 22.4 s ($n = 10$).

Movie S8. Magnetic guidewire telerobotically controlled by the same neurointerventionalist for performance comparison with the manually controlled passive guidewire. This video demonstrates our system's steering and navigational performance driven by the same neurointerventionalist in comparison with the manually manipulated passive guidewire in **movie S7** over 10 consecutive trials. The interventionalist was trained to operate the developed system (Novice 3 in **fig. S15**) to produce steady-state performances with the telerobotically controlled magnetic guidewire. The average time ($\pm$ standard deviation) it took for the interventionalist to complete the demonstrated task with the telerobotically controlled magnetic guidewire was 42.9 ± 10.5 s ($n = 10$).